EUREC⁴A

Bjorn Stevens[1], Sandrine Bony[2], David Farrell[3], Felix Ament[4,1], Alan Blyth[5], Christopher Fairall[6],
Johannes Karstensen[7], Patricia K. Quinn[8], Sabrina Speich[9], Claudia Acquistapace[10],
Franziska Aemisegger[11], Anna Lea Albright[2], Hugo Bellenger[2], Eberhard Bodenschatz[12],
Kathy-Ann Caesar[3], Rebecca Chewitt-Lucas[3], Gijs de Boer[13,6], Julien Delanoë[14], Leif Denby[15],
Florian Ewald[16], Benjamin Fildier[9], Marvin Forde[3], Geet George[1], Silke Gross[16], Martin Hagen[16],
Andrea Hausold[16], Karen J. Heywood[17], Lutz Hirsch[1], Marek Jacob[10], Friedhelm Jansen[1],
Stefan Kinne[1], Daniel Klocke[18], Tobias Kölling[19,1], Heike Konow[4], Marie Lothon[20], Wiebke Mohr[21],
Ann Kristin Naumann[1,22], Louise Nuijens[23], Léa Olivier[24], Robert Pincus[13,6], Mira Pöhlker[25],
Gilles Reverdin[24], Gregory Roberts[26,27], Sabrina Schnitt[10], Hauke Schulz[1], A. Pier Siebesma[23],
Claudia Christine Stephan[1], Peter Sullivan[28], Ludovic Touzé-Peiffer[2], Jessica Vial[2], Raphaela Vogel[2],
Paquita Zuidema[29], Nicola Alexander[3], Lyndon Alves[30], Sophian Arixi[26], Hamish Asmath[31],
Gholamhossein Bagheri[12], Katharina Baier[1], Adriana Bailey[28], Dariusz Baranowski[32],
Alexandre Baron[33], Sébastien Barrau[26], Paul A. Barrett[34], Frédéric Batier[35], Andreas Behrendt[36],
Arne Bendinger[7], Florent Beucher[26], Sebastien Bigorre[37], Edmund Blades[38], Peter Blossey[39],
Olivier Bock[40], Steven Böing[15], Pierre Bosser[41], Denis Bourras[42], Pascale Bouruet-Aubertot[24],
Keith Bower[43], Pierre Branellec[44], Hubert Branger[45], Michal Brennek[46], Alan Brewer[47],
Pierre-Etienne Brilouet [20], Björn Brügmann[1], Stefan A. Buehler[4], Elmo Burke[48], Ralph Burton[5],
Radiance Calmer[13], Jean-Christophe Canonici[49], Xavier Carton[50], Gregory Cato Jr.[51],
Jude Andre Charles[52], Patrick Chazette[33], Yanxu Chen[9], Michal T. Chilinski[46], Thomas Choularton[43],
Patrick Chuang[53], Shamal Clarke[54], Hugh Coe[43], Céline Cornet[55], Pierre Coutris[56], Fleur Couvreux[26],
Susanne Crewell[10], Timothy Cronin[57], Zhiqiang Cui[15], Yannis Cuypers[24], Alton Daley[3],
Gillian M. Damerell[17], Thibaut Dauhut[1], Hartwig Deneke[58], Jean-Philippe Desbios[49], Steffen Dörner[25],
Sebastian Donner[25], Vincent Douet[59], Kyla Drushka[60], Marina Dütsch[61,62], André Ehrlich[63],
Kerry Emanuel[57], Alexandros Emmanouilidis[63], Jean-Claude Etienne[26], Sheryl Etienne-Leblanc[64],
Ghislain Faure[26], Graham Feingold[47], Luca Ferrero[65], Andreas Fix[16], Cyrille Flamant[66],
Piotr Jacek Flatau[27], Gregory R. Foltz[67], Linda Forster[19], Iulian Furtuna[68], Alan Gadian[15],
Joseph Galewsky[69], Martin Gallagher[43], Peter Gallimore[43], Cassandra Gaston[29], Chelle Gentemann[70],
Nicolas Geyskens[71], Andreas Giez[16], John Gollop[72], Isabelle Gouirand[73], Christophe Gourbeyre[56],
Dörte de Graaf[1], Geiske E. de Groot[23], Robert Grosz[46], Johannes Güttler[12], Manuel Gutleben[16],
Kashawn Hall[3], George Harris[74], Kevin C. Helfer[23], Dean Henze[75], Calvert Herbert[74],
Bruna Holanda[25], Antonio Ibanez-Landeta[12], Janet Intrieri[76], Suneil Iyer[60], Fabrice Julien[26],
Heike Kalesse[63], Jan Kazil[13,47], Alexander Kellman[72], Abiel T. Kidane[21], Ulrike Kirchner[1],
Marcus Klingebiel[1], Mareike Körner[7], Leslie Ann Kremper[25], Jan Kretzschmar[63], Ovid Krüger[25],
Wojciech Kumala[46], Armin Kurz[16], Pierre L'Hégaret[77], Matthieu Labaste[24], Tom Lachlan-Cope[78],
Arlene Laing[79], Peter Landschützer[1], Theresa Lang[22,1], Diego Lange[36], Ingo Lange[4],
Clément Laplace[80], Gauke Lavik[21], Rémi Laxenaire[81], Caroline Le Bihan[44], Mason Leandro[53],
Nathalie Lefevre[24], Marius Lena[68], Donald Lenschow[28], Qiang Li[16], Gary Lloyd[43], Sebastian Los[69],
Niccolò Losi[82], Oscar Lovell[83], Christopher Luneau[84], Przemyslaw Makuch[85], Szymon Malinowski[46],
Gaston Manta[9], Eleni Marinou[16,86], Nicholas Marsden[43], Sebastien Masson[24], Nicolas Maury[26],
Bernhard Mayer[19], Margarette Mayers-Als[3], Christophe Mazel[87], Wayne McGeary[88,3],
James C. McWilliams[89], Mario Mech[10], Melina Mehlmann[7], Agostino Niyonkuru Meroni[90],
Theresa Mieslinger[4,1], Andreas Minikin[16], Peter Minnett[29], Gregor Möller[19], Yanmichel Morfa Avalos[1],
Caroline Muller[9], Ionela Musat[2], Anna Napoli[90], Almuth Neuberger[1], Christophe Noisel[24],
David Noone[91], Freja Nordsiek[12], Jakub L. Nowak[46], Lothar Oswald[16], Douglas J. Parker[15],

Carolyn Peck[92], Renaud Person[24,93], Miriam Philippi[21], Albert Plueddemann[37], Christopher Pöhlker[25], Veronika Pörtge[19], Ulrich Pöschl[25], Lawrence Pologne[3], Michał Posyniak[32], Marc Prange[4], Estefanía Quiñones Meléndez[75], Jule Radtke[22,1], Karim Ramage[59], Jens Reimann[16], Lionel Renault[94,89], Klaus Reus[7], Ashford Reyes[3], Joachim Ribbe[95], Maximilian Ringel[1], Markus Ritschel[1], Cesar B. Rocha[96], Nicolas Rochetin[9], Johannes Röttenbacher[63], Callum Rollo[17], Haley Royer[29], Pauline Sadoulet[26], Leo Saffin[15], Sanola Sandiford[3], Irina Sandu[97], Michael Schäfer[63], Vera Schemann[10], Imke Schirmacher[4], Oliver Schlenczek[12], Jerome Schmidt[98], Marcel Schröder[12], Alfons Schwarzenboeck[56], Andrea Sealy[3], Christoph J. Senff[13,47], Ilya Serikov[1], Samkeyat Shohan[63], Elizabeth Siddle[17], Alexander Smirnov[99], Florian Späth[36], Branden Spooner[3], M. Katharina Stolla[1], Wojciech Szkółka[32], Simon P. de Szoeke[75], Stéphane Tarot[44], Eleni Tetoni[16], Elizabeth Thompson[6], Jim Thomson[60], Lorenzo Tomassini[34], Julien Totems[33], Alma Anna Ubele[25], Leonie Villiger[11], Jan von Arx[21], Thomas Wagner[25], Andi Walther[100], Ben Webber[17], Manfred Wendisch[63], Shanice Whitehall[3], Anton Wiltshire[83], Allison A. Wing[101], Martin Wirth[16], Jonathan Wiskandt[7], Kevin Wolf[63], Ludwig Worbes[1], Ethan Wright[81], Volker Wulfmeyer[36], Shanea Young[102], Chidong Zhang[8], Dongxiao Zhang[103,8], Florian Ziemen[104], Tobias Zinner[19], and Martin Zöger[16]

[1]Max Planck Institute for Meteorology, Hamburg, Germany
[2]LMD/IPSL, Sorbonne Université, CNRS, Paris, France
[3]Caribbean Institute for Meteorology and Hydrology, Barbados
[4]Universität Hamburg, Hamburg, Germany
[5]National Centre for Atmospheric Science, University of Leeds, Leeds, UK
[6]NOAA Physical Sciences Laboratory, Boulder, CO, USA
[7]GEOMAR Helmholtz Centre for Ocean Research Kiel, Kiel, Germany
[8]NOAA PMEL, Seattle, WA, USA
[9]LMD/IPSL, École Normale Supérieure, CNRS, Paris, France
[10]Institute for Geophysics and Meteorology, University of Cologne, Cologne, Germany
[11]Institute for Atmospheric and Climate Science, ETH Zurich, Zurich, Switzerland
[12]Max Planck Institute for Dynamics and Self-Organization, Göttingen, Germany
[13]Cooperative Institute for Research in Environmental Sciences,
University of Colorado Boulder, Boulder, CO, USA
[14]LATMOS/IPSL, Université Paris-Saclay, Université de Versailles Saint-Quentin-en-Yvelines (UVSQ),
Guyancourt, France
[15]University of Leeds, Leeds, UK
[16]Deutsches Zentrum für Luft- und Raumfahrt, Oberpfaffenhofen, Germany
[17]Centre for Ocean and Atmospheric Sciences, School of Environmental Sciences,
University of East Anglia, Norwich, UK
[18]Hans-Ertel-Zentrum für Wetterforschung, Deutscher Wetterdienst (DWD), Offenbach, Germany
[19]Ludwig-Maximilians-Universität München, Munich, Germany
[20]Laboratoire d'Aérologie, University of Toulouse, CNRS, Toulouse, France
[21]Max Planck Institute for Marine Microbiology, Bremen, Germany
[22]Meteorological Institute, Center for Earth System Research and Sustainability,
Universität Hamburg, Hamburg, Germany
[23]Delft University of Technology, Delft, the Netherlands
[24]Sorbonne Université, CNRS, IRD, MNHN, UMR7159 LOCEAN/IPSL, Paris, France
[25]Max Planck Institute for Chemistry, Mainz, Germany
[26]CNRM, University of Toulouse, Météo-France, CNRS, Toulouse, France
[27]Scripps Institution of Oceanography, University of California San Diego, San Diego, CA, USA
[28]National Center for Atmospheric Research, Boulder, CO, USA
[29]University of Miami, Miami, FL, USA
[30]Hydrometeorological Service, Georgetown, Guyana
[31]Institute of Marine Affairs, Chaguaramas, Trinidad and Tobago
[32]Institute of Geophysics, Polish Academy of Sciences, Warsaw, Poland
[33]LSCE/IPSL, CNRS-CEA-UVSQ, Université Paris-Saclay, Gif-sur-Yvette, France
[34]Met Office, Exeter, UK
[35]Frédéric Batier Photography, Berlin, Germany

[36]Institute of Physics and Meteorology, University of Hohenheim, Stuttgart, Germany
[37]Woods Hole Oceanographic Institution, Woods Hole, MA, USA
[38]Queen Elizabeth Hospital, St. Michael, Barbados
[39]Department of Atmospheric Sciences, University of Washington, Seattle, WA, USA
[40]Institut de Physique du Globe de Paris (IPGP), Paris, France
[41]ENSTA Bretagne, Lab-STICC, CNRS, Brest, France
[42]Aix-Marseille Université, Université de Toulon, CNRS, IRD, MIO UM 110, Marseille, France
[43]University of Manchester, Manchester, UK
[44]French Research Institute for Exploitation of the Sea (IFREMER), Brest, France
[45]Institut de Recherche sur les Phénomènes Hors Equilibre (IRPHE), CNRS/AMU/ECM, Marseille, France
[46]University of Warsaw, Warsaw, Poland
[47]NOAA Chemical Sciences Laboratory, Boulder, CO, USA
[48]St. Christopher Air & Sea Ports Authority, Basseterre, St. Kitts and Nevis
[49]Service des Avions Français Instrumentés pour la Recherche en Environnement (SAFIRE), Météo-France,
CNRS, CNES, Cugnaux, France
[50]LOPS/IUEM, Université de Bretagne Occidentale, CNRS, Brest, France
[51]Saint Vincent and the Grenadines Meteorological Services, Argyle, St. Vincent and the Grenadines
[52]Grenada Meteorological Services, St. George's, Grenada
[53]University of California Santa Cruz, Santa Cruz, CA, USA
[54]Cayman Islands National Weather Service, Grand Cayman, Cayman Islands
[55]LOA, Université de Lille, CNRS, Lille, France
[56]LAMP, Université Clermont Auvergne, CNRS, Clermont-Ferrand, France
[57]Massachusetts Institute of Technology, Cambridge, MA, USA
[58]Leibniz Institute for Tropospheric Research, Leipzig, Germany
[59]IPSL, CNRS, Paris, France
[60]Applied Physics Laboratory, University of Washington, Seattle, WA, USA
[61]Department of Earth and Space Sciences, University of Washington, Seattle, WA, USA
[62]Department of Meteorology and Geophysics, University of Vienna, Vienna, Austria
[63]Leipzig Institute for Meteorology, University of Leipzig, Leipzig, Germany
[64]Meteorological Department St. Maarten, Simpson Bay, Sint Maarten
[65]Gemma Center, University of Milano-Bicocca, Milan, Italy
[66]LATMOS/IPSL, Sorbonne Université, CNRS, Paris, France
[67]NOAA Atlantic Oceanographic and Meteorological Laboratory, Miami, FL, USA
[68]Compania Fortuna, Sucy-en-Brie, France
[69]Department of Earth and Planetary Sciences, University of New Mexico, Albuquerque, NM, USA
[70]Farallon Institute, Petaluma, CA, USA
[71]DT-INSU, CNRS, Plouzane, France
[72]Barbados Coast Guard, St. Michael, Barbados
[73]The University of the West Indies, Cave Hill Campus, Cave Hill, Barbados
[74]Regional Security System, Christ Church, Barbados
[75]College of Earth, Ocean and Atmospheric Sciences, Oregon State University, Corvallis, OR, USA
[76]NOAA Earth System Research Laboratory, Boulder, CO, USA
[77]LOPS, Université de Bretagne Occidentale, Brest, France
[78]British Antarctic Survey, Cambridge, UK
[79]Caribbean Meteorological Organization, Port of Spain, Trinidad and Tobago
[80]Institut Pierre-Simon Laplace (IPSL), Paris, France
[81]Center for Ocean-Atmospheric Prediction Studies, Florida State University, Tallahassee, FL, USA
[82]University of Milano-Bicocca, Milan, Italy
[83]Trinidad and Tobago Meteorological Services, Piarco Trinidad, Trinidad and Tobago
[84]OSU Institut Pythéas, Marseille, France
[85]Institute of Oceanology, Polish Academy of Sciences, Sopot, Poland
[86]National Observatory of Athens, Athens, Greece
[87]Dronexsolution, Toulouse, France
[88]Barbados Meteorological Services, Christ Church, Barbados

[89]Department of Atmospheric and Oceanic Sciences, University of California Los Angeles,
Los Angeles, CA, USA
[90]CIMA Research Foundation, Savona, Italy
[91]University of Auckland, Auckland, New Zealand
[92]Meteorological Service, Kingston, Jamaica
[93]Sorbonne Université, CNRS, IRD, MNHN, INRAE, ENS, UMS 3455, OSU Ecce Terra, Paris, France
[94]LEGOS, University of Toulouse, IRD, CNRS, CNES, UPS, Toulouse, France
[95]University of Southern Queensland, Toowoomba, Australia
[96]University of Connecticut Avery Point, Groton, CT, USA
[97]European Centre for Medium-Range Weather Forecasts, Reading, UK
[98]Naval Research Laboratory, Monterey, CA, USA
[99]Science Systems and Applications, Inc., Lanham, Maryland, USA
[100]University of Wisconsin-Madison, Madison, WI, USA
[101]Department of Earth, Ocean and Atmospheric Science, Florida State University, Tallahassee, FL, USA
[102]National Meteorological Service of Belize, Ladyville, Belize
[103]Cooperative Institute for Climate, Ocean, and Ecosystem Studies,
University of Washington, Seattle, WA, USA
[104]Deutsches Klimarechenzentrum GmbH, Hamburg, Germany

Correspondence: Bjorn Stevens (bjorn.stevens@mpimet.mpg.de)
and Sandrine Bony (sandrine.bony@lmd.ipsl.fr)

Abstract. The science guiding the EUREC[4]A campaign and its measurements is presented. EUREC[4]A comprised roughly 5 weeks of measurements in the downstream winter trades of the North Atlantic – eastward and southeastward of Barbados. Through its ability to characterize processes operating across a wide range of scales, EUREC[4]A marked a turning point in our ability to observationally study factors influencing clouds in the trades, how they will respond to warming, and their link to other components of the earth system, such as upper-ocean processes or the life cycle of particulate matter. This characterization was made possible by thousands (2500) of sondes distributed to measure circulations on meso- (200 km) and larger (500 km) scales, roughly 400 h of flight time by four heavily instrumented research aircraft; four global-class research vessels; an advanced ground-based cloud observatory; scores of autonomous observing platforms operating in the upper ocean (nearly 10 000 profiles), lower atmosphere (continuous profiling), and along the air–sea interface; a network of water stable isotopologue measurements; targeted tasking of satellite remote sensing; and modeling with a new generation of weather and climate models. In addition to providing an outline of the novel measurements and their composition into a unified and coordinated campaign, the six distinct scientific facets that EUREC[4]A explored – from North Brazil Current rings to turbulence-induced clustering of cloud droplets and its influence on warm-rain formation – are presented along with an overview of EUREC[4]A's outreach activities, environmental impact, and guidelines for scientific practice. Track data for all platforms are standardized and accessible at https://doi.org/10.25326/165 (Stevens, 2021), and a film documenting the campaign is provided as a video supplement.

1   Introduction

The clouds of the trades are curious creatures. On the one hand they are fleeting and sensitive to subtle shifts in the wind, to the presence and nature of particulate matter, and to small changes in radiant energy transfer, surface temperatures, or myriad other factors as they scud along the sky (Siebesma et al., 2020). On the other hand, they are immutable and substantial – like Magritte's suspended stone (Stevens and Schwartz, 2012). In terms of climate change,

should even a small part of their sensible side express itself with warming, large effects could result. This realization has motivated a great deal of research in recent years (Bony et al., 2015), culminating in a recent field study named[1] EUREC[4]A. The measurements made as part of EUREC[4]A, which this pa-

---

[1]EUREC[4]A is more of a name than an abbreviation; in terms of the latter it expands to *ElUcidating the RolE of Cloud–Circulation Coupling in ClimAte* and is pronounced *heúrēka*, as Archimedes is reputed to have exclaimed upon discovering buoyancy while bathing.

per describes, express the most ambitious effort ever to quantify how cloud properties covary with their atmospheric and oceanic environment across an enormous (mm to Mm) range of scales.

Initially EUREC[4]A was proposed as a way to test hypothesized cloud-feedback mechanisms thought to explain large differences in model estimates of climate sensitivity, as well as to provide benchmark measurements for a new generation of models and satellite observations (Bony et al., 2017). To meet these objectives required quantifying different measures of clouds in the trade winds as a function of their large-scale environment. In the past, efforts to use measurements for this purpose – from Bannon (1949) to BOMEX[2] (Holland and Rasmusson, 1973) and from ASTEX (Albrecht et al., 1995) to RICO (Rauber et al., 2007) – have been hampered by an inability to constrain the mean vertical motion over larger scales and by difficulties in quantifying something as multifaceted as a field of clouds (Bretherton et al., 1999; Stevens et al., 2001; Siebesma et al., 2003; vanZanten et al., 2011). EUREC[4]A was made possible by new methods to measure these quantities, many developed through experimentation over the past decade in and around the Barbados Cloud Observatory (Stevens et al., 2016, 2019a). To execute these measurements required a high-flying aircraft (HALO, High Altitude and Long Range Research Aircraft) to characterize the clouds and cloud environment from above, both with remote sensing and through the distribution of a large number of dropsondes around the perimeter of a mesoscale (ca. 200 km diameter) circle. A second low-flying aircraft (the ATR), with in situ cloud sensors and sidewards-staring active remote sensing, was necessary to ground truth the remote sensing from above, as well as to determine the distribution of cloudiness and aspects of the environment as seen from below. By making these measurements upwind of the Barbados Cloud Observatory (BCO), and by adding a research vessel (the R/V *Meteor*) for additional surface-based remote sensing and surface flux measurements, the environment and its clouds would be better constrained.

Quantifying day-to-day variations in both cloudiness and its environment opened the door to additional questions, greatly expanding EUREC[4]A's scope. In addition to testing hypothesized cloud-feedback mechanisms, EUREC[4]A's experimental plan was augmented to (i) quantify the relative role of micro- and macrophysical factors in rain formation; (ii) quantify different factors influencing the mass, energy, and momentum balances in the sub-cloud layer; (iii) identify processes influencing the evolution of ocean meso-scale eddies; (iv) measure the influence of ocean heterogeneity, i.e., fronts and eddies, on air–sea interaction and cloud formation; and (v) provide benchmark measurements for a new genera-

tion of both fine-scale coupled models and satellite retrievals. Complementing these scientific pursuits, EUREC[4]A developed outreach and capacity-building activities that allowed scientists coming from outside the Caribbean to benefit from local expertise and vice versa.

Addressing these additional questions required a substantial expansion of the activities initially planned by the Barbadian–French–German partnership that initiated EUREC[4]A. This was accomplished through a union of projects led by additional investigators. For instance, EUREC[4]A-UK (a UK project) brought a Twin Otter (TO for short) and ground-based facilities for aerosol measurements to advance cloud physics studies; EUREC[4]A-OA secured the service of two additional research vessels (the R/V *L'Atalante* and the R/V *Maria Sibylla Merian*) and various ocean-observing platforms to study ocean processes; and the Atlantic Tradewind Ocean–Atmosphere Mesoscale Interaction Campaign (ATOMIC) brought an additional research vessel (the R/V *Ronald H. Brown*), assorted autonomous systems, and the WP-3D Orion, "Miss Piggy", to help augment studies of air–sea and aerosol–cloud interactions. Additionally, nationally funded projects supported a large-scale sounding array, the installation of a scanning precipitation radar, the deployment of shipborne kite-stabilized helium balloons (CloudKites), a network of water stable isotopologue measurements, and a rich assortment of uncrewed aerial and seagoing systems, among them fixed-wing aircraft, quadcopters, drifters, buoys, underwater gliders, and Saildrones. Support within the region helped link activities to operational initiatives, such as a training program for forecasters, and fund scientific participation from around the Caribbean. The additional measurement platforms considerably increased EUREC[4]A's scientific scope and geographic footprint, as summarized in Fig. 1.

This article describes EUREC[4]A in terms of seven different facets as outlined above. To give structure to such a vast undertaking, we focus on EUREC[4]A's novel aspects but strive to describe these in a way that also informs and guides the use of EUREC[4]A data by those who did not have the good fortune to share in their collection. The presentation (Sect. 3) of these seven facets is framed by an overview of the general setting of the campaign in Sect. 2, as well as a discussion of more peripheral, but still important, aspects such as data access, good scientific practice, and the environmental impact of our activities in Sect. 4.

2 General setting and novel measurements

EUREC[4]A deployed a wide diversity of measurement platforms over two theaters of action: the "Tradewind Alley" and the "Boulevard des Tourbillons", as illustrated schematically in Fig. 1. Tradewind Alley comprised an extended corridor with its downwind terminus defined by the BCO and extending upwind to the Northwest Tropical Atlantic Sta-

---

[2]Abbreviations for field experiments, many instruments, instrument platforms, and institutions often take the form of a proper name, which if not expanded in the text is provided in the cited literature or in Appendix B describing the instrumentation.
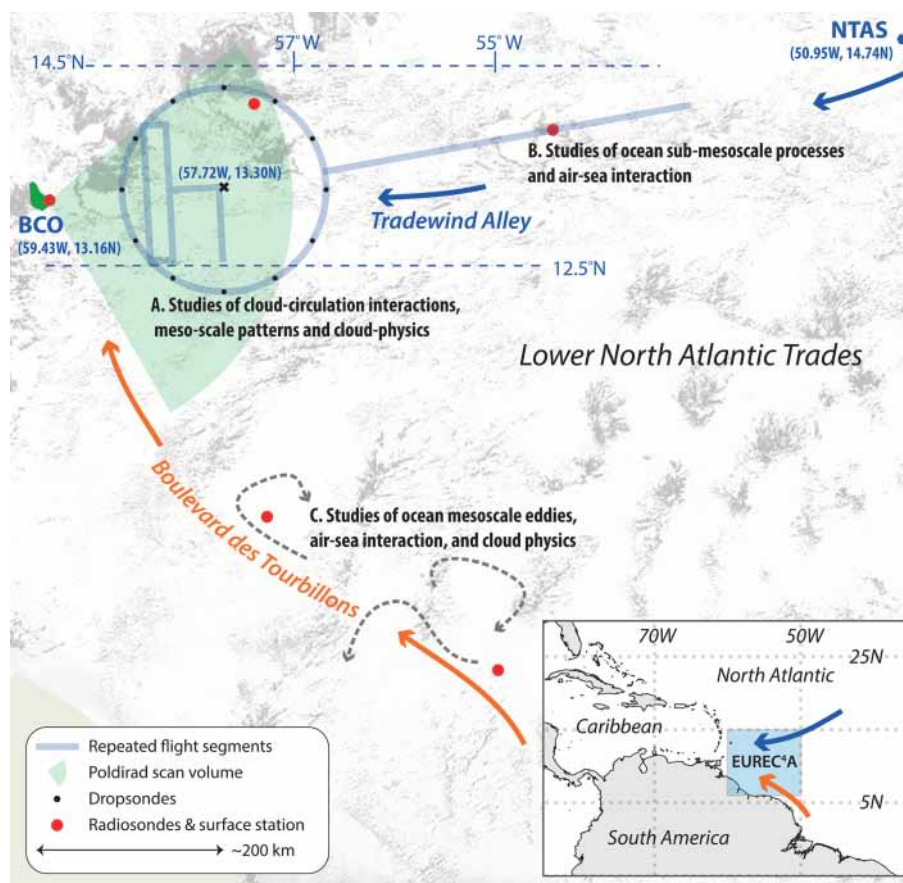
Figure 1. The EUREC^{4}A study area in the lower trades of the North Atlantic. The zonally oriented band following the direction of the trades between the Northwest Tropical Atlantic Station (NTAS) and the Barbados Cloud Observatory (BCO) is called Tradewind Alley. It encompasses study areas A and B. The "EUREC^{4}A-Circle" is defined by the circular airborne sounding array centered at 13.3° N, 57.7° W. A third study area (C) followed the southeast-to-northwest meanders of what we called the Boulevard des Tourbillons. The background shows a negative of the cloud field taken from the 5 February 2020 MODIS-Terra (ca. 14:30 UTC) overpass.

tion (NTAS, 15° N, 51° W), an advanced open-ocean mooring (Weller, 2018; Bigorre and Plueddemann, 2020) that has been operated continuously since 2001. Measurements aimed at addressing the initial objectives of EUREC^{4}A were situated near the western end of the corridor, within the range of low-level scans of a C-band radar installed on Barbados. The area of overlap between the radar and the (∼ 200 km diameter) EUREC^{4}A-Circle (marked A in Fig. 1) defined a region of intensive measurements in support of studies of cloud–circulation interactions, cloud physics, and factors influencing the mesoscale patterning of clouds. Additional measurements between the NTAS and 55° W (Region B in Fig. 1) supported studies of air–sea interaction and provided complementary measurements of the upwind environment, including a characterization of its clouds and aerosols.

The Boulevard des Tourbillons describes the geographic region that hosted intensive measurements to study how air–sea interaction is influenced by mesoscale eddies, sub-mesoscale fronts, and filaments in the ocean (Region C in Fig. 1). Large (ca. 300 km) warm eddies – which migrate

northwestward and often envelope Barbados, advecting large freshwater filaments stripped from the shore of South America – created a laboratory well suited to this purpose. These eddies, known as North Brazil Current (NBC) rings, form when the retroflecting NBC pinches off around 7° N. Characterizing these eddies further offered the possibility to expand the upper-air network of radiosondes and to make contrasting cloud measurements in a potentially different large-scale environment. This situation led EUREC^{4}A to develop its measurements following the path of the NBC rings toward Barbados from their place of formation near the point of the NBC retroflection, with a center of action near Region C in Fig. 1. Measurements in the Boulevard des Tourbillons extended the upper-air measurement network and provided cloud measurements to contrast with similar measurements being made in Tradewind Alley.
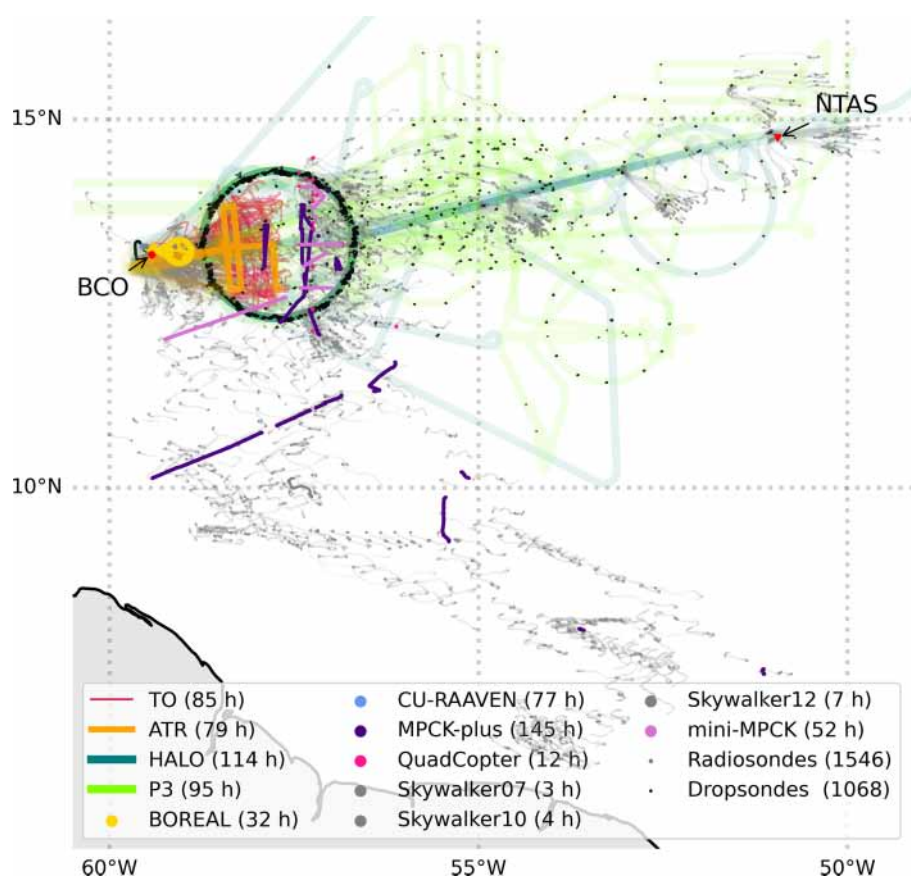
Figure 2. Heat map showing distribution of airborne-platform tracks, colored (with transparency) by platform. Sonde trajectories are shown by trail of dots, with the slower ascent of the radiosondes leading to greater horizontal displacements leading to tracks resembling gray whiskers. The legend includes the flight time (defined as the period spent east of 59° W and west of 45° W to exclude ferries) and number of soundings. Radiosondes ascents and descents with valid data are treated as independent.

2.1 Platforms for measuring the lower atmosphere

Aerial measurements were made by research aircraft, uncrewed (i.e., remotely piloted) aerial systems (UASs), and from balloon- or parachute-borne soundings. These were mostly distributed along Tradewind Alley. Figure 2 shows the realization of the EUREC⁴A strategy: the EUREC⁴A-Circle (teal) and box L (orange) stand out, indicative of the number of times HALO and the ATR flew these patterns. The very large number of dropsondes deployed by HALO (black dots) gives further emphasis to the EUREC⁴A-Circle. Excursions by HALO and flights by the P-3 extended the area of measurements upwind toward the NTAS. The TO intensively sampled clouds in the area of ATR operations in the western half of the EUREC⁴A-Circle. UASs provided extensive measurements of the lower atmosphere, mostly in the area between the EUREC⁴A-Circle and Barbados. Due to their limited range many (Skywalkers, CU-RAAVEN, and quadcopter) only appear as dots on Fig. 2.

Different clusters of radiosonde soundings (evident as short traces, or whiskers, of gray dots) can also be discerned in Fig. 2. Those soundings originating from the BCO (342) and from the R/V *Meteor* (362) were launched from relatively fixed positions, with the R/V *Meteor* operating between 12.5 and 14.5° N along the 57.25° W meridian. East of the EUREC⁴A-Circle, sondes were launched by the R/V *Ronald H. Brown* (Ron Brown), which mostly measured air masses in coordination with the P-3 measurements between the NTAS and the EUREC⁴A-Circle. The R/V *Maria Sibylla Merian (MS-Merian)* and R/V *L'Atalante (Atalante)* combined to launch 424 sondes in total, as they worked water masses up and down the Boulevard. For most sondes, measurements were recorded for both the ascent and descent, with descending sondes falling by parachute for all platforms except the R/V *Ron Brown*. The synoptic environment encountered during EUREC⁴A, the radiosonde measurement strategy, and an analysis of the sonde data are described in more detail by Stephan et al. (2021).

HALO, the ATR, and most of the UASs emphasized statistical sampling. Hence flight plans did not target specific conditions, except to adjust the ATR flight levels relative to the height of the sub-cloud layer – but this varied rela-
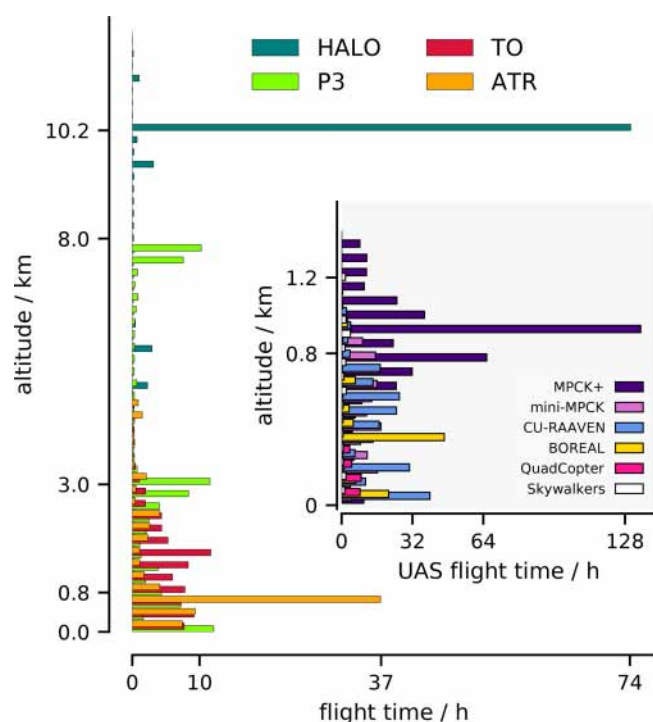
Figure 3. Flight time spent at different altitudes by different airborne platforms. Uncrewed aerial systems (UASs) shown in inset.

2.2 Airborne platforms for measuring the upper ocean and air–sea interface

Four global-class research vessels – all equipped with surface meteorological measurements and underway temperature/salinity sampling devices – and scores of autonomous ocean-observing platforms (AOOPs) were deployed along Tradewind Alley and the Boulevard des Tourbillons. The tracks of the surface vessels are shown in Fig. 4. These tracks, colored by measurements of the near-surface water temperature, show slightly more variability in water temperatures along the Boulevard des Tourbillons, in contrast with more steady westward warming of surface temperatures following the trades along Tradewind Alley. The more dynamic situation along the Boulevard des Tourbillons, as compared to the situation on the Tradewind Alley, required a different measurement strategy. For the former, research vessels actively tracked and surveyed mesoscale features, and for the latter the sampling was more statistical so as to better support the airborne measurements and cloud characterization.

Along Tradewind Alley, the R/V *Meteor* mostly worked along the line of longitude at 57.25° W between 12.4 and 14.2° N. The R/V *Ron Brown*, coordinating its measurements with the P-3, was stationed between the NTAS and the MOVE[3] moorings in January and in the region upwind of the EUREC[4]A-Circle, near 55° W in February. For both positions, SWIFT buoys were deployed and recovered in coordination with P-3 airborne expendable bathythermograph (AXBT) soundings. A Saildrone, two Wave Gliders, an AutoNaut (Caravela), four underwater gliders, and extensive conductivity–temperature–depth (CTD) casts from the two ships profiled the upper ocean Fig. 5.

Along the Boulevard des Tourbillons the R/V *MS-Merian* and the R/V *Atalante* studied the meso- and submesoscale dynamics. Both research vessels extensively profiled the ocean's upper kilometer using a wide assortment of instruments, including underway CTDs, moving vessel profilers, vertical microstructure profilers (VMP and MSS), expendable bathythermographs (XBTs), and expendable CTDs (XCTDs). Three ocean gliders (one SeaExplorer and two Slocum electric gliders) provided dense sampling (more than 1300 profiles, most to at least 700 m, Fig. 5) of subsurface structures associated with mesoscale eddies. Of the roughly 8000 upper-ocean profiles performed during EUREC[4]A, nearly three-fourths were performed in coordination with the eddy sampling along the Boulevard des Tourbillons. Four Saildrones, 22 drifters and four deployments of two air–sea fluxes observing prototypes, OCARINA and PICCOLO, substantially expanded the observations at the ocean–atmosphere interface. Five Argo floats equipped with a dissolved-oxygen sensor were deployed to allow a La-

tively little. During planned excursions from its circling flight pattern, HALO also positioned its track for satellite overpasses – one by MISR (5 February 2021) and another by the core GPM satellite (11 February 2020). Measurements from the MPCK+ (a large CloudKite tethered to the R/V *MS-Merian*) emphasized the lower cloud layer, selecting conditions when clouds seemed favorable. The mini-MPCK was used more for profiling the boundary layer and the cloud-base region and was deployed when conditions allowed. The Twin Otter targeted cloud fields, often flying repeated samples through cloud clusters identified visibly, but also sampled the sub-cloud layer. The P-3 strategy was more mixed; some flights targeted specific conditions, and others were more statistically oriented (for example, to fill gaps in the HALO and ATR sampling strategy). The different sampling strategies are reflected in Fig. 3, where the measurements of HALO are concentrated near 10.2 km and those of the ATR at about 800 m, with relative uniform sampling of the trade wind moist layer by the Twin Otter. Figure 3 also shows the strong emphasis on sampling the lower atmosphere, with relatively uniform coverage of the lower 3 km. Except for the Twin Otter, which was limited to daytime operations, takeoff and landing times of the aircraft were staggered, with three night flights by the P-3, to better sample the diurnal cycle. Data papers for the individual platforms are being prepared and will describe their activities in greater detail.

---

[3]Meridional Overturning Variability Experiment mooring located 50 nmi (nautical miles) northwest of the NTAS and not shown in Fig. 1.
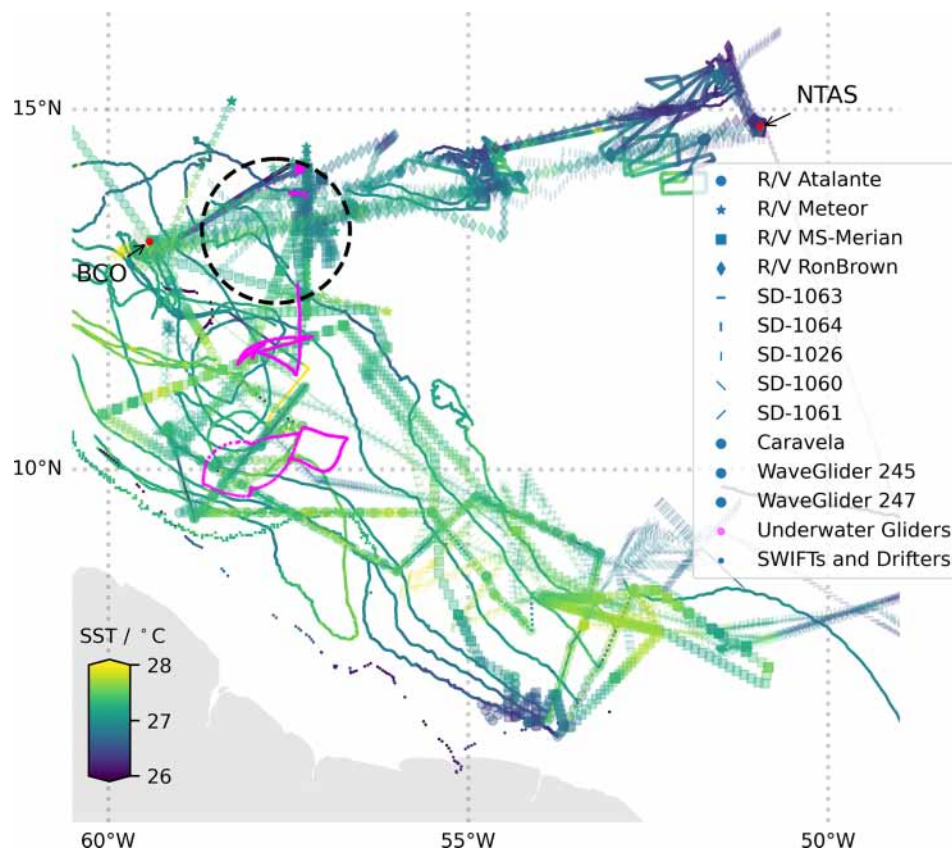
Figure 4. Map showing surface- and subsurface-platform trajectories, colored by (uncalibrated) near-surface water temperature for platforms with near-surface measurements.

grangian monitoring of the ocean surface and subsurface dynamics during and after the campaign.

To effectively survey features in the active waters of the Boulevard des Tourbillons, the sampling strategy and cruise plan were assessed daily, using information from the previous day's measurements, updates from satellite products, weather forecasts, and ocean predictions. Tailored satellite products and model predictions were provided by a variety of groups[4] to help track and follow surface features in near real time.

2.3   Instrument clusters

EUREC^{4}A set itself apart from past field studies both through new types of measurements, as performed by individual platforms, but also through the quantity or clustering of certain instruments. Instrument clustering means using similar instruments across a number of platforms so as to improve the statistical characterization of air masses and their evolution. The ability to make such measurements enables estimates of systematic and random measurement errors, giving rise

[4]Collecte Localisation Satellites, the Centre Aval de Traitement des Données, Mercator Ocean, and the Center for Ocean-Atmospheric Prediction Studies.
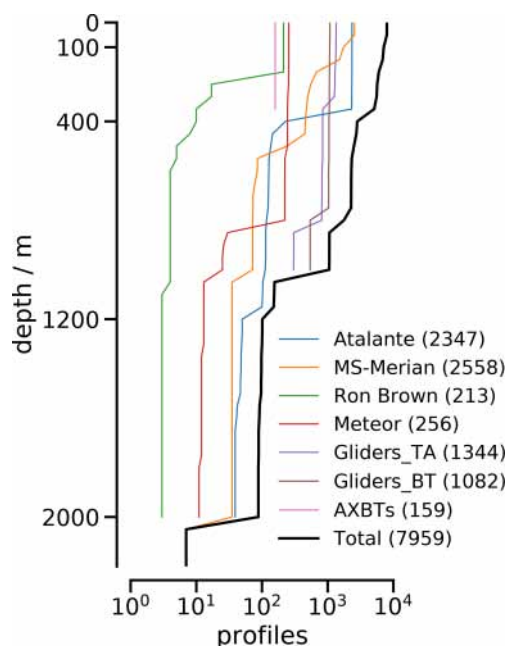
to a different quality of measurement as compared to those made previously, especially in marine environments. Examples are described below and include the use of remote sensing, instruments for measuring stable water isotopologues, and drones. A platform-by-platform listing of the EUREC^{4}A instrumentation is provided in Appendix B.

2.3.1   Remote sensing

EUREC^{4}A included eight cloud-sensitive Doppler (W- and Ka-band) radars. Four zenith-staring instruments were installed at surface sites (BCO, R/V *MS-Merian*, R/V *Meteor*, and R/V *Ron Brown*) and three on aircraft (nadir, zenith on the ATR, HALO, and the P-3). The ATR flew a second, horizontally staring, Doppler system. Two scanning radars (a C-band system installed on Barbados and a P-3 X-band tail radar) and three profiling rain radars (one at the BCO, another at the Caribbean Institute for Meteorology and Hydrology (CIMH), and a third on the R/V *MS-Merian*) measured precipitation. The R/V *MS-Merian* additionally had an X-Band radar installed for wave characteristics and surface currents over a roughly 2 km footprint around the ship. Fourteen lidars were operated, four of which were advanced (high-spectral-resolution, multi-wavelength) Raman or DIAL (dif-

Figure 5. Number of profiles sampling seawater properties at the indicated depth. Ship-based profiling is from CTD casts, underway CTDs, XBTs, and moving vessel profilers. AXBTs were dropped by the P-3.

Figure 6. Vertical latent-heat (vaporization enthalpy) flux as a function of time and height above the platform as measured from the combination of water vapor Raman lidar (ARTHUS) and Doppler wind lidar aboard the R/V *MS-Merian*. The mean value over the 3 d period is $100 \, \mathrm{W \, m^{-2}}$ at 200 m, and the fluxes are positive throughout the sub-cloud layer.

ferential absorption lidar) systems for profiling water vapor and aerosol/cloud properties. The Raman systems (at the BCO, on the R/V *MS-Merian*, and on the R/V *Meteor*) were upward-staring surface-mounted systems, and the DIAL aboard HALO operated in a nadir-staring mode (Wirth et al., 2009). On the ATR a backscatter UV lidar operated alongside the horizontally staring radar, looking horizontally to provide an innovative planform view of cloudiness near cloud base. In total, six wind lidars and three ceilometers were operated from the BCO and all research vessels except for the R/V *Atalante*. As an example of the sensor synergy arising from the multitude of sensors, Fig. 6 shows water vapor flux profiles (Behrendt et al., 2020) estimated from co-located vertically staring Doppler wind lidar and Raman (water vapor) lidar measurements from the ARTHUS system (Lange et al., 2019) aboard the R/V *MS-Merian*. This type of measurement strategy, employing a dense network of remote sensors to both improve sampling and realize synergies, is increasingly emphasized for land–atmosphere interaction studies (e.g., Wulfmeyer et al., 2018), but it is more difficult to realize, and thus uncommon, over the ocean.

More standard, but still unprecedented by virtue of its space–time–frequency coverage, was the contribution of airborne, surface, and space-based passive remote sensing to EUREC[4]A. Three 14-channel microwave radiometers operated from surface platforms, and a 25 channel nadir-staring system operated from HALO (Mech et al., 2014; Schnitt et al., 2017). Handheld sun-photometer measurements were
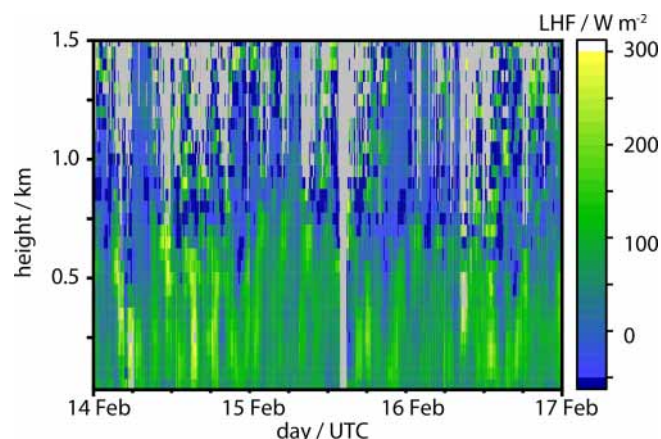
made on all four research vessels, and an automated system operated from Ragged Point, near the BCO, provided additional constraints on estimates of aerosol loading (from lidars) and column water vapor (from radiometers). Infrared radiometers for measuring the surface skin temperature were operated on the ATR, HALO, the R/V *Ron Brown*, the BOREAL, and CU-RAAVEN UASs, as well as on the five Saildrones. For estimating fluxes of radiant energy, broadband longwave and shortwave radiometers were installed on three of the airborne (zenith and nadir) and surface (zenith) platforms. In addition, HALO and the R/V *Meteor* hosted high-spectral-resolution systems measuring shortwave and near-infrared down- and upwelling radiances (Wendisch et al., 2001). Near-real-time geostationary GOES-East satellite imagery and cloud product retrievals between 19° N–5° S and 49–66° W were collected, with finer temporal resolution every minute (between 14 January and 14 February, with a few data gaps from diversions to support hazardous weather forecasting in other domains) archived over most of this domain. ASTER's high-resolution (15 m visible and near-infrared, and 90 m thermal) imager on board TERRA was activated between 7–17° N and 41–61° W. It recorded 412 images of $60 \, \mathrm{km} \times 60 \, \mathrm{km}$ in 25 overpasses between 11 January and 15 February. These images are complemented by Sentinel-2 data with images at 10 m resolution in some visible–near-infrared bands and 20 m resolution in shortwave-infrared bands relevant for cloud microphysical retrievals.

The intensity of remote sensing instrumentation in the vicinity of the EUREC[4]A-Circle will support efforts to, for the first time, observationally close the column energy budget over the ocean, as well as efforts to test hypotheses that link precipitation to processes across very different time and space scales.
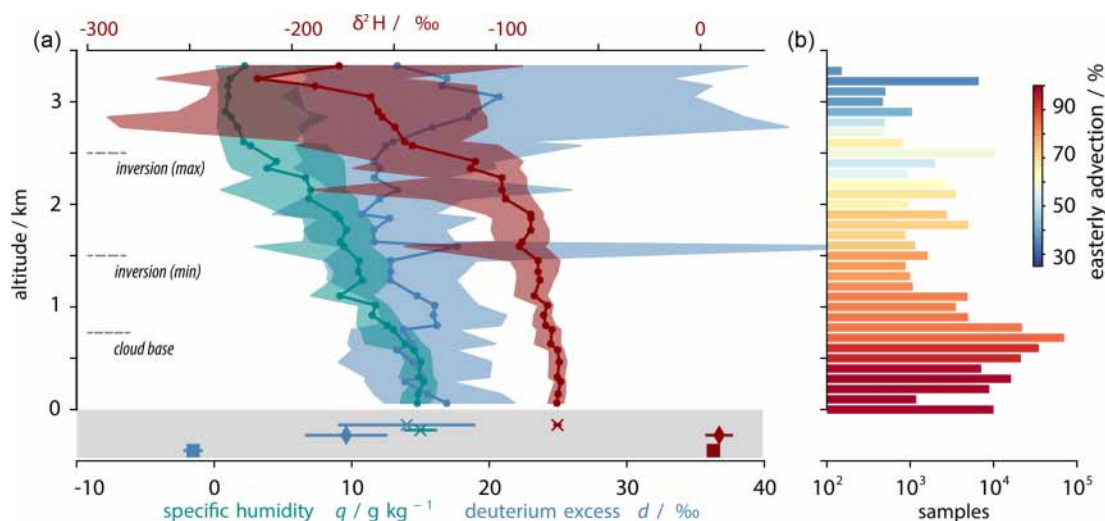
Figure 7. Water stable isotopologues mass fractions **(a)** binned by altitude over all EUREC^{4}A measurements, including samples from near-surface waters. Percent of measurements at each altitude **(b)** associated with winds from the east (45 to 135° from north).

2.3.2   Stable water isotopologues

EUREC^{4}A benefited from an unusually complete and spatially extensive network of stable water isotopologue measurements ($H_2^{18}O$, $H_2^{16}O$, and HDO) distributed across multiple platforms. Seven laser spectrometers and five precipitation sampling systems especially designed to avoid postsampling re-evaporation were deployed. At the BCO, two laser spectrometers provided robust high-frequency measurements of isotopologues in water vapor and 46 event-based precipitation samples were collected. Three ships – the R/V *Atalante*, the R/V *Meteor*, and the R/V *Ron Brown* – were similarly equipped and in addition collected ocean water samples (340 in total) from the underway water line and the CTDs. These samples have been analyzed in the laboratory together with 50 shipboard rainfall samples. Two of the high-frequency laser spectrometers were mounted on the ATR and P-3 to measure the vertical distribution of water isotopologues. The airborne measurements also added continuity, sampling air masses between the BCO and R/V *Meteor* stations and between the R/V *Meteor* and the upwind R/V *Ron Brown*. The measurements provided very good coverage through the lower (3 km) atmosphere. Air-parcel backward trajectories based on three-dimensional wind fields from the operational ECMWF analyses indicate that boundary layer air came almost exclusively from the east, with a more heterogeneous origin of air masses sampled above 2500 m (Fig. 7; see also Aemisegger et al., 2021). Large-scale context for the in situ measurements will be provided by retrievals of atmospheric HDO and $H_2^{16}O$ from spaceborne instruments.

The size of the network of isotopologue measurements and the degree of coordination among the different measurement sites will enable investigations of the variability of the stable water isotopologues – in space and time, in ocean water, atmospheric vapor, and precipitation following the trades – that were previously not possible.

2.3.3   Drones and tethered platforms

A diversity of tethered and remotely piloted platforms provided measurements in the lower atmosphere and upper ocean. Many of these had been used in past field studies, but what set EUREC^{4}A apart was its coordinated use of so many platforms. Five fixed-wing systems and a quadcopter provided approximately 200 h of open-ocean atmospheric profiling, while seven underwater gliders profiled the underlying ocean well over a thousand times, mostly between the surface and 700 m. Figure 8 presents measurements from one of the underwater gliders and the CU-RAAVEN – which along with the other fixed-wing systems (BOREAL and Skywalkers) was flown from Morgan Lewis Beach, a windward beach about 20 km north of the BCO. The measurements highlight the boundary layers on either side of the air–sea interface – one (in the atmosphere) extending to about 700 m and capped by a layer that is stably stratified with respect to unsaturated, but unstable with respect to saturated, convection. The typical ocean mixed layer was as impressively well mixed, but over a layer about 10 times shallower. Here the measurements document the peculiar situation of salinity maintaining the stratification that caps the downward growth of the ocean mixed layer. Ship-based measurements of the air–sea interface were greatly extended by 5 Saildrones, 3 wave gliders, 6 SWIFT drifters, 2 autonomous prototype drifters (OCARINA and PICCOLO), and 22 drifters. In Fig. 8 the air–sea temperature difference of about 0.8 K is based on Saildrone data, which also quantifies the role of moisture in driving density differences. During EUREC^{4}A more than half of the
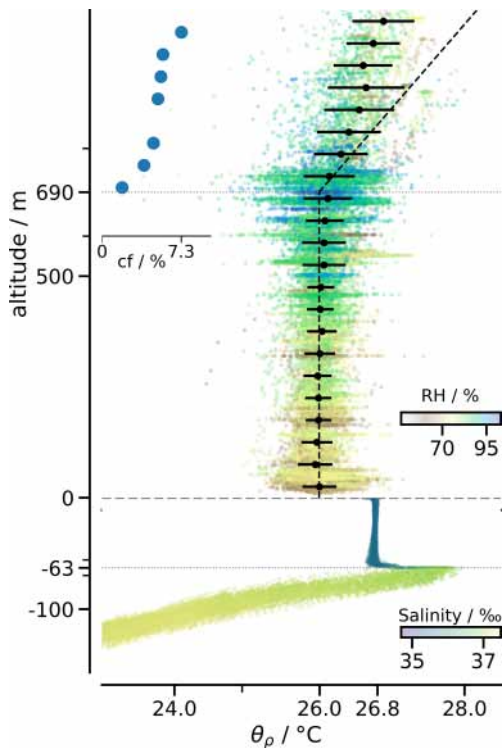
Figure 8. Ocean and atmospheric boundary layer upwind of the BCO. Dots show CU-RAAVEN measurements of the density potential temperature vs. altitude, as well as underwater glider measurements of the temperature below the surface. Values are normalized to compensate for differences associated with either synoptic variations or from variations in the depth of the sampled planetary boundary layers. Blue dots show profile of cloud fraction from all MPCK profiles. The dashed (black) line marks the potential temperature of near-surface air isentropically lifted from the surface; the slope discontinuity at the lifting condensation level (690 m) marks the shift from an unsaturated to a saturated isentrope. The temperature difference between the sea surface and the lower atmosphere is taken from Saildrone data.

density difference between the near-surface air and air saturated at the skin temperature of the underlying ocean can be attributed to variations in the specific humidity.

Kite-stabilized helium balloons, known as Max Planck CloudKites (MPCKs), made their campaign debut during EUREC[4]A. Three instrument systems were flown. One large MPCK+ instrument was flown on the R/V *MS-Merian*, suspended from the larger aerostat (115 kg lift, 1.5 km ceiling) to sample clouds. Two smaller mini-MPCK instruments were flown both on the same aerostat and the smaller aerostat on the R/V *Meteor* (30 kg lift, 1 km ceiling), which focused on boundary layer and cloud-base profiling. Measurements from the CloudKites are used to quantify the cloud coverage in Fig. 8.

3 EUREC[4]A's seven science facets

In this section we elaborate on topics that motivated EUREC[4]A and how this influenced the measurement strategy. The presentation aims to emphasize novel contributions without loosing sight of the need to also provide a clear sketch of the campaign as a whole. Additional details describing the activities of specific platforms, or groups of platforms, are being described in complementary data papers, and a full listing of the deployed instrumentation is presented in Appendix B.

3.1 Testing hypothesized cloud-feedback mechanisms

As described by Bony et al. (2017), EUREC[4]A was conceived as a way to test the hypothesis that enhanced mixing of the lower troposphere desiccates clouds at their base, in ways that warming would enhance (Rieck et al., 2012; Sherwood et al., 2014; Brient et al., 2016; Vial et al., 2016) but the signal of which has not been possible to identify in past measurements (Nuijens et al., 2014). In addition, recent research suggests that clouds in the trades tend to organize in mesoscale patterns (Stevens et al., 2019b) selected by environmental conditions (Bony et al., 2020). These findings raise the additional question as to whether changes in the mesoscale cloud organization with evolving environmental conditions might play a role in low-cloud feedbacks. To address these questions, EUREC[4]A developed techniques to measure the strength of convective-scale and large-scale vertical motions in the lower troposphere, together with the co-incident cloud-base cloud fractions, in addition to other possible drivers of changes in mesoscale cloud patterns, such as coherent structures within the sub-cloud layer, radiative cooling, and air mass trajectories.

To make the desired measurements required HALO and the ATR to fly closely coordinated flight patterns, ideally sampling different phases of the diurnal cycle (Vial et al., 2019). This was realized by HALO circling (at an altitude of 10.2 km) 3.5 times over 210 min. Within this period three full sounding circles were defined by a set of 12 dropsonde launches, one for each 30° change in heading. The start time of successive sounding circles was offset by 15 min so as to distribute the sondes through the period of circling. During this time HALO also provided continuous active and passive remote sensing of the cloud field below. Flying 50 min "box" patterns just above the estimated cloud base (usually near a height of about 800 m, Fig. 3), the ATR provided additional remote sensing, as well as in situ turbulence and cloud microphysical measurements. After two to three box patterns, the ATR flew two to four L-shaped wind-aligned and wind-perpendicular patterns (the "L" in Fig. 1) – at the top, middle, and bottom of the sub-cloud layer – before returning to Barbados to refuel for a second mission. While the ATR was refueling, HALO made an excursion, usually in the direction of the R/V *Ron Brown* and the NTAS buoy. On all but
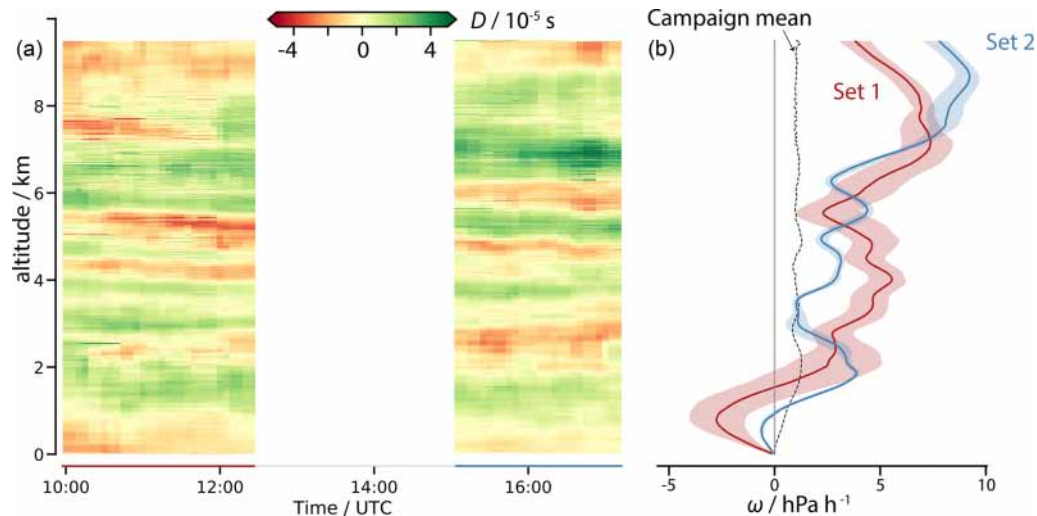
Earth Syst. Sci. Data, 13, 4067–4119, 2021

https://doi.org/10.5194/essd-13-4067-2021

Figure 9. Divergence of the horizontal wind versus height **(a)**, and vertical pressure velocity versus height **(b)**. Divergence estimated from dropsonde measurements and vertical pressure velocity derived from these for the two sets of circles flown on 5 February. The black dashed line on the rightmost panel denotes vertical pressure velocity averaged over all EUREC^{4}A-Circle dropsonde measurements.

two occasions the ATR returned to the measurement zone after refueling (about 90 min later) to execute a second round of sampling, accompanied by HALO returning for another 210 min tour of the EUREC^{4}A-Circle. All told this resulted in 18 coordinated (4 h) flight segments, one of which involved the P-3 substituting for HALO on one of its nighttime flights.

A first target of the flight strategy was the measurement, for each sounding circle, of the vertical profile of mass divergence using dropsondes (following Bony and Stevens, 2019). In Fig. 9 the vertical pressure velocity, ω, estimated from this divergence is averaged over a set of three circles for the two 5 February circling periods. Also shown is the average over all circles over all days. The continuity of the divergence within a circle and across two circling periods – although on some flights vertical motion can change more markedly across sets of circles – gives confidence that the measurements are capturing a physical signal. It also shows, for the first time from measurements on this scale, how the mean ω reduces to the expected climatological profile, with a magnitude (of about $1\,h\,Pa\,h^{-1}$) similar to what is expected if subsidence warming is to balance radiative cooling.

The second target of the flight strategy was the measurement of the cloud fraction at cloud base through horizontal lidar–radar measurements by the ATR. In fields of optically thin shallow cumuli (such as those associated with the cloud patterns observed on 28 January), cloud droplets were too small to be detected by the radar, but the lidar could detect the presence of many successive clouds along a roughly 10 km line of sight, i.e., half of its box-pattern width (Fig. 10; Chazette et al., 2021). In the presence of larger cloud droplets, normally associated with larger or more-water-laden clouds, such as on 11 February, the radar detected larger droplets and rain drops over a range of 10 km

(Fig. 10). The lidar–radar synergy will provide, for each ATR box, the cloud fraction and the distribution of cloud geometric and optical properties at cloud base. The second, vertically pointing ATR cloud radar allows a characterization of the aspect ratio of clouds, which may help infer the mesoscale circulations within the cloud field. These measurements, associated with new methods developed to estimate the cloud-base mass flux (Vogel et al., 2020), and to characterize the mesoscale cloud patterns from GOES-16, MODIS, or ASTER satellite observations (Stevens et al., 2019b; Mieslinger et al., 2019; Bony et al., 2020; Denby, 2020; Rasp et al., 2021), will make it possible to test cloud-feedback mechanisms and advance understanding of the processes underlying the formation of the mesoscale cloud patterns, as well as whether they influence the hypothesized feedback mechanisms.

3.2 Quantifying processes influencing warm-rain formation

As highlighted by Bodenschatz et al. (2010), the range of scales, from micro- to megameters, that clouds encompass has long been one of their fascinating aspects. Measurements made during EUREC^{4}A quantified, for the first time, the main processes that influence trade wind clouds across this full range of scales. By doing so, long-standing questions in cloud physics were addressed, including (i) whether microphysical processes substantially influence the net amount of rain that forms in warm clouds and (ii) how important is the interplay between warm-rain development and the mesoscale organization of cloud fields. These questions identify precipitation development as the link among processes acting on
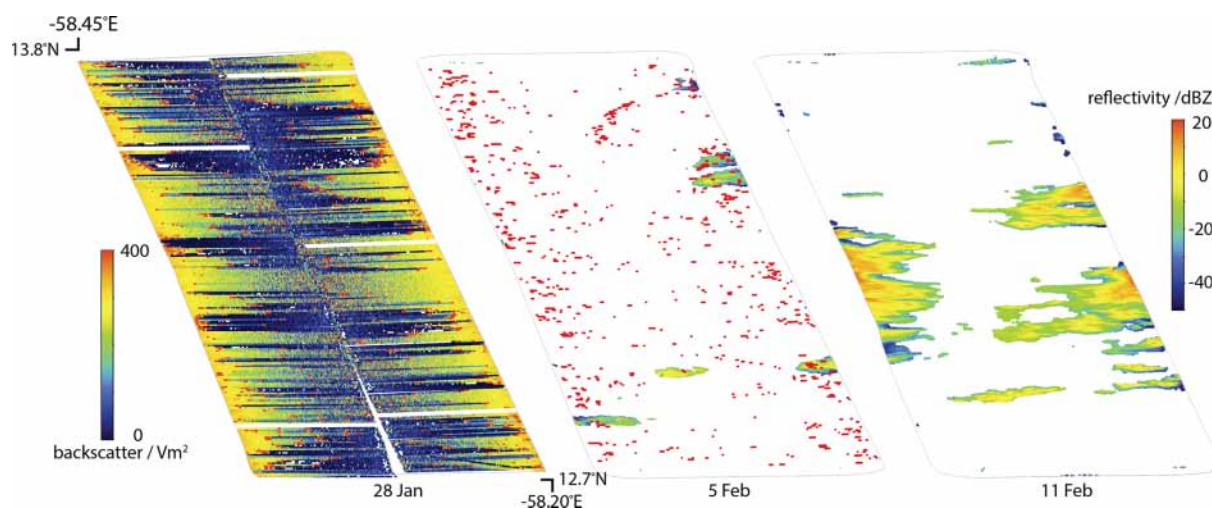
https://doi.org/10.5194/essd-13-4067-2021

Earth Syst. Sci. Data, 13, 4067–4119, 2021

Figure 10. Illustration for January 28 lidar, February 5 lidar and radar, and February 11 radar cloud field observed at cloud base by the ATR with horizontal lidar (detected cloud boundaries denoted by red dots) and radar measurements.

different scales and hence guided EUREC[4]A's measurement strategy.

On the particle scale, measurements were performed to characterize aerosols and to quantify how small-scale turbulence mixing processes influence droplet kinematic interactions and activation. Aerosol properties and turbulence both imprint themselves on the cloud microstructure and thereby affect the formation of precipitation (Broadwell and Breidenthal, 1982; Cooper et al., 2013; Li et al., 2018; Pöhlker et al., 2018; Wyszogrodzki et al., 2013). In most cases, not only the magnitude, but also the sign of the hypothesized effects can be ambiguous, if not controversial. For example, by acting as an additional source of cloud condensation nuclei (CCN), Saharan dust may retard the formation of precipitation (Levin et al., 1996; Gibson et al., 2007; Bailey et al., 2013), but if present as giant CCN, it may have the opposite effect (Jensen and Nugent, 2017).

On the cloud scale, the intensity of rain and the evaporation of raindrops can lead to downdrafts, cold pools, and mesoscale circulations which can lift air parcels, producing secondary and more sustained convection (e.g., Snodgrass et al., 2009). These cloud-scale circulations, which the EUREC[4]A-Circle measurements quantified, may also change the vigor and mixing characteristics of cloud. This could in turn influence precipitation formation, a process that Seifert and Heus (2013) suggest may be self-reinforcing, consistent with an apparent link between precipitation and mesoscale cloud patterns such as "fish" or "flowers" (Stevens et al., 2019b).

On larger (20 to 200 km) scales, horizontal transport, which determines whether or not Saharan dust reaches the clouds, as well as factors such as the tropospheric stability, or patterns of mesoscale convergence and divergence, which influence cloud vertical development, may affect the efficiency

of warm-rain production. In addition to the characterization of the environment from the dropsondes, the positioning of surface measurements (R/V *Meteor*, R/V *Ron Brown*, and BCO) helped characterize the Lagrangian evolution of the flow, also in terms of aerosol and cloud properties.

Figure 11 shows an example of the cascade of measurements, spanning scales covering 10 orders of magnitude. On the smallest $O(10^{-5}\,\mathrm{m})$ scale, a sample holographic image from an instrument mounted on the MPCK+ shows the spatial and size distribution of individual cloud drops. In situ measurements and airborne remote sensing document the cloud microphysical structure and its relationship to the properties of the turbulent wind field. On scales of hundreds of meters to a few kilometers, vertically and horizontally pointing cloud radars and lidars characterize the geometry and the macrophysical properties of clouds. On yet larger $O(10^5\,\mathrm{m})$ scales, the spatial organization and clustering of clouds and precipitation features are captured by satellite, by high-resolution radiometry from high-altitude aircraft, and by the C-band scanning radar, POLDIRAD (Schroth et al., 1988).

An example of how the measurements upwind and downwind of the EUREC[4]A-Circle helped constrain its aerosol environment is shown in Fig. 12. Two periods with larger CCN number concentration (near $450\,\mathrm{cm}^{-3}$), both associated with periods of elevated mineral dust, can be identified in measurements made aboard the R/V *Ron Brown* (east of 55° W) and from the ground station at Ragged Point (Pöhlker et al., 2018). The slight lag of the Ragged Point measurements relative to those on the R/V *Ron Brown* is consistent with the positioning of the two stations and the westward dust transport by the mean flow. The episodes of elevated dust are believed to be from Saharan dust outbreaks, which are unusual in the (boreal or northern) winter months (Prospero et al.,
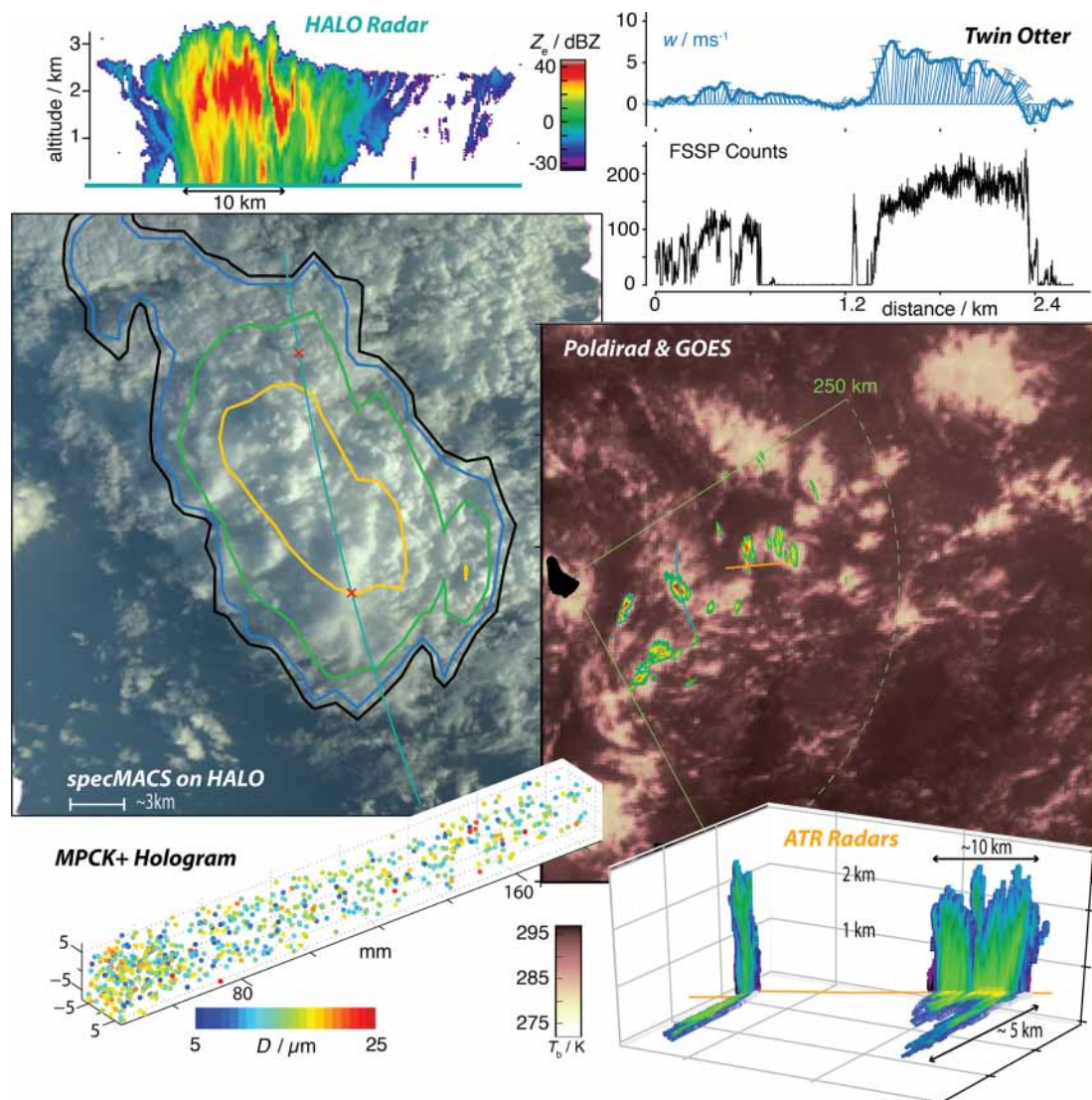
Figure 11. Measurements within the Tradewind Alley test section (5 February) define a multi-scale cloud chamber. The figure highlights clustering on different scales. Scanning C-band radar (POLDIRAD) 0.6° scan (11:25:25 UTC) is overlain on the 11:33:41 UTC brightness temperature (at 10.6 μm) measured by GOES-16, with coincident segments of the HALO and ATR flight tracks. Radar images from the ATR (horizontal and zenith) and HALO (nadir) are shown (all radar imagery shares the same color scale), as well as cloud water and updraft velocity from a penetration of cloud by the Twin Otter (later in the day, at 18:32 UTC, near 13.55° N, 58.26° W at 1910 m). Visual image from the specMACS instrument, with POLDIRAD reflectivity contours superimposed, shows the cloud visualization along a segment of the HALO flight track. MPCK+ hologram measurements (made in the southern portion of the circle – 12.25° N, 57.70° W at 1084 m – on 17 February) demonstrate the capability to measure the three-dimensional distribution of individual cloud droplets colored by size.

2020) and can greatly increase CCN number concentrations (Wex et al., 2016). In between these events, CCN number concentration are 3-fold smaller ($150\,cm^{-3}$), which we take as representative of the clean maritime environment.

The degree of aerosol variability should aid efforts to untangle the relative role of different factors influencing warm-rain formation. Helping in this regard is that variations in CCN concentrations are not too rapid to call into question the idea of associating a 3 h period of measurements on the EUREC4A-Circle with a particular concentration of CCN:

50 % of the Ragged Point measurements change by less than 10 % over a 3 h period, and only 20 % of the time are changes larger than 30 % measured.

3.3 Sub-cloud mass, matter, energy, and momentum budgets

Early field studies extensively and compellingly documented the basic structure of the lower atmosphere in the trades (Riehl et al., 1951; Malkus, 1958; Augstein et al., 1974;
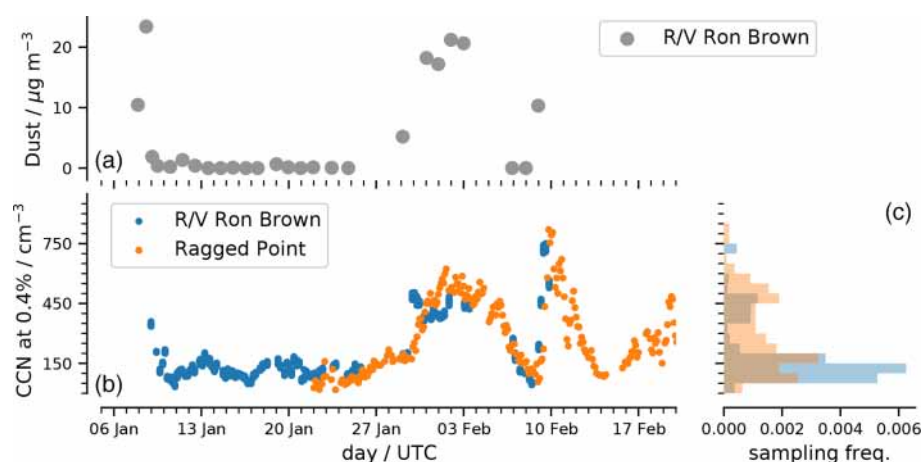
Figure 12. Aerosol characteristics measured in the Tradewind Alley highlight two periods (31 January to 6 February and 9–12 February) of CCN-laden air. Dust mass density from the R/V *Ron Brown* **(a)**, which was mostly east of 55° W. Normalized histogram showing the relative frequency of occurrence of different CCN concentration levels **(c)**. Note that the periods of observation at the two locations are only partly overlapping.

Brummer et al., 1974; Garstang and Betts, 1974). What remains poorly understood is the relative role of specific processes, particularly those acting at the mesoscale, in influencing this structure. A specific question that EUREC⁴A aims to answer is the importance of downdrafts, and associated cold pools (Rauber et al., 2007; Zuidema et al., 2012), in influencing boundary layer thermodynamic structure and momentum transport to the surface. A related question is whether the links between the cloud and sub-cloud layer depend on the patterns of convective organization, for instance as a result of differences in the circulation systems that may accompany such patterns.

For quantifying the sub-cloud layer budgets, as for many other questions, a limiting factor has been an inability to measure mesoscale variability in the vertical motion field. EUREC⁴A's measurements not only address this past short coming, but the ship-based sounding network additionally quantifies the mean vertical motion at different scales. The arrangement of measurements, particularly flight segments, was designed to quantify the Lagrangian evolution of air masses, with legs repeated on every mission at levels attuned to the known structure of the lower troposphere, i.e., near the surface, in the middle, near the top, and just above the sub-cloud layer, as well as in and just above the cloud layer. Past studies using a single aircraft, albeit in a more homogeneous environment, demonstrate that such a strategy can close boundary layer moisture and energy budgets (Stevens et al., 2003). Doing so also aids quantification of the vertical profile of turbulent transport and contributions associated with horizontal heterogeneity and sets the stage for estimating mass and energy budgets through the entire atmospheric column.

To address the measurement challenge posed by an environment rich in mesoscale variability, EUREC⁴A made use of additional aircraft and a larger array of surface measurements (also from uncrewed platforms) as well as extensive ship and airborne active remote sensing, and a network of water stable isotopologues (as presented in Sect. 2.3.2). At the BCO, aboard the R/V *Meteor* and on the R/V *MS-Merian*, advanced Raman lidars provided continuous profiling of water vapor, clouds, temperature, and aerosols. The nadir-staring WALES lidar on HALO likewise profiled water vapor, clouds, and aerosols. As an example of this capability, Fig. 13 presents relative humidity data (deduced from temperature and absolute humidity retrievals) from the BCO lidar. These measurements document the time–height evolution of water vapor in the boundary layer, something impossible to assess from in situ measurements, which measure at only a few levels, or soundings, which are sparse in time.

The BCO lidar measurements quantify the structure of moist or dry layers in the free atmosphere, as well as variations in the cloud and sub-cloud layers, illustrating days of more nocturnal activity (centered on 1 February), and also features presumed to be the signature of mesoscale circulations. Analyses of *Meteor* data show a signature of the diel cycle (0.54 K), but it is more pronounced (1.27 K) over the BCO – both at the surface and as sensed by the BCO lidar at 400 m. Both a slight slackening of the winds and an upwind adjustment in response to diurnal heating of the island could be responsible for the amplification of the diel cycle over the BCO.

Possible mesoscale circulations are the focus of the magnification in the lower panels (of Fig. 13). Shown are measurements in the lower 3 km for a 5 h period late on 2 February 2020. During this period aerosol-poor air appears to descend adiabatically into the cloud layer (near 2 km), coincident with a large-scale fold of cloud layer air into the sub-cloud layer. This results in a sharp contact discontinuity
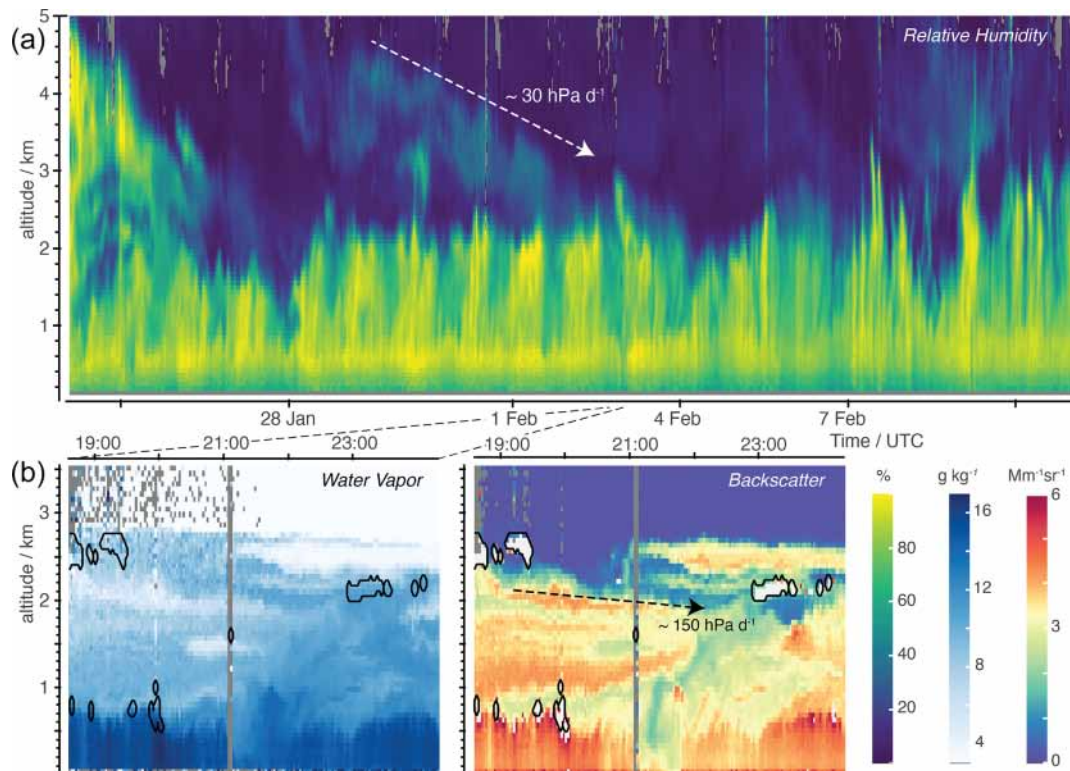
Figure 13. Lidar profiling of the lower atmosphere using the CORAL lidar at the Barbados Cloud Observatory. The upper panel **(a)** shows the relative humidity in the lower 5 km over the entirety of the campaign. The lower panel **(b)** shows (from left to right) show the specific humidity over a 4 h period marked by a large intrusion of cloud layer air on 2 February and the associated aerosol/cloud backscatter. Also shown is the Lagrangian evolution of humidity, or backscatter features, with dashed arrows following the descent with time of features (white arrow in the upper panel: following RH feature; black arrow in the lower panel: following backscatter feature) being indicative of the magnitude of vertical velocity variations on different temporal scales. Gray bars on lower plots (at 21 h) are missing data.

(aerosol front) near 21:00 UTC, which extends to the surface and is also evident in the water vapor field. Typically the marine boundary (sub-cloud) layer is viewed as a turbulent layer that primarily interacts with the much-larger-scale evolution of the free atmosphere through small-scale entrainment at its top. Events such as the one shown in Fig. 13 suggest that in addition to downdrafts and the cold pools they feed, circulations on scales commensurate with and larger than the depth of the sub-cloud layer may be important for boundary layer budgets.

Similar considerations also apply to the momentum budget of the trades. In Dixit et al. (2020) idealized large-eddy simulations are shown to underestimate the flux of momentum in the sub-cloud layer, something they hypothesize to arise from an absence of mesoscale circulations in the simulations. As an example of efforts to quantify such processes Fig. 14 shows the total wind speed measured in the sub-cloud layer by the long-range wind lidar aboard the R/V *Meteor*. The lower panel documents kilometer-scale wind speed variations on the order of $2\,\mathrm{m\,s^{-1}}$ that extend into the surface layer (derived from the short-range wind lidar, defined with respect to 3-hourly running means). One question asked

is whether, for a given surface friction, convectively driven flows can sustain a relatively large near-surface wind, and weaker surface layer wind shear, than expected from shear-driven turbulence alone. The third panel shows that the ratio of wind speeds at 40 m to wind speeds at 200 m, as a measure of surface layer wind shear, is close (ca. 0.95) to unity. Combined with surface heat and momentum fluxes measured by other platforms, the lidars provide a unique opportunity to identify the influence of (moist) convection on wind stress at the surface.

3.4 Ocean mesoscale eddies and sub-mesoscale fronts and filaments

Mesoscale eddies, fronts, and filaments – not unlike the mesoscale circulations that are the subject of increasing attention in the atmosphere – are coherent structures that may be important for linking surface mixed layer to the interior ocean dynamics (Carton, 2010; Mahadevan, 2016; McWilliams, 2016). By virtue of a sharp contrast with their surroundings, these structures can efficiently transport enthalpy, salt, and carbon through the ocean. Though satellite
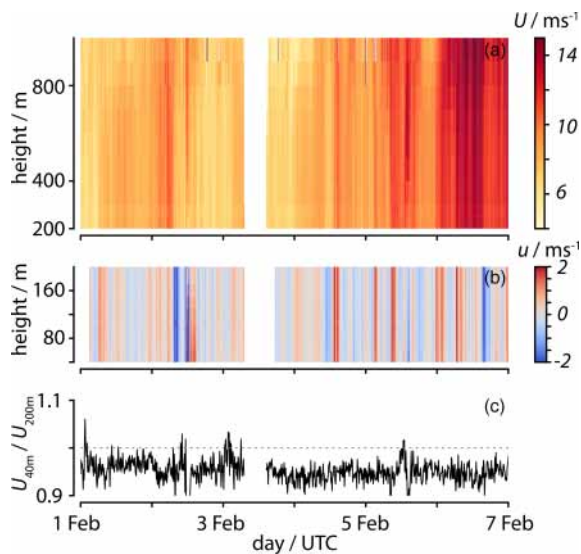
Figure 14. Sub-cloud layer lidar wind versus height above the R/V *Meteor*. Panel **(a)** shows the value of the wind speed in the sub-cloud layer, above 200 m. Fluctuations of the near-surface wind speed from a 3-hourly running mean value **(b)** are shown with an expanded vertical scale. The lower time series **(c)** shows the ratio of the wind speed at 40 m (the lowest remotely sensed level) to its value at 200 m.

Figure 15. Surface density gradients at different horizontal length scales. Bivariant histogram shows counts versus (1 to 200 km) and strength of gradient as measured by Saildrones (note the log-scale color bar). Inset is power spectral density of the surface density gradients, calculated by averaging periodograms constructed for each vehicle after de-trending the data and smoothing the data with a 2 km Gaussian filter. The red line shows the linear regression best fit slope of −2.3.

observations have enhanced knowledge of their occurrence and surface imprint (Chelton et al., 2001), the sparsity of direct observations limits our ability to test understanding of such structures, in particular subsurface eddies. Understanding of the role of these types of structures is further limited by their short lifespans (hours to days) and small spatial scales (0.1 to 10 km), which make them difficult to observe. These facts motivated ocean observations during EUREC^{4}A, as did recent work suggesting that such coherent structures, in particular localized upwelling, downwelling, straining, stratification variability, wave breaking, and vertical mixing, may couple with and influence atmospheric processes, including cloud formation (Lambaerts et al., 2013; Renault et al., 2016; Foussard et al., 2019).

To address these questions, measurements during EUREC^{4}A attempted to quantify how near-surface currents, density, and waves varied across and within different dynamical regimes, e.g., for mesoscale eddies, fronts, and filaments. Such measurements aimed to answer specific questions not unlike those posed for the atmospheric boundary layer, namely to quantify the contribution of such structures to the spatial and temporal variability of the upper ocean. EUREC^{4}A distinguished itself from past campaigns that have attempted similar measurements – LatMix (Shcherbina et al., 2013), OSMOSIS (Buckingham et al., 2016), and CARTHE (D'Asaro et al., 2018) – by virtue of the number and diversity of observing platforms deployed (Saildrones, underwater gliders, instrumentally enhanced
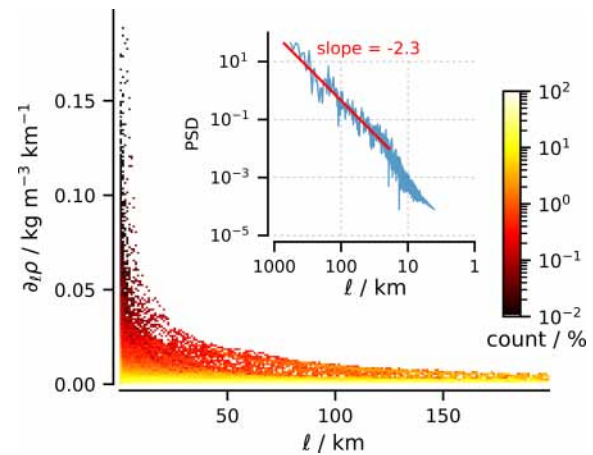
surface and subsurface drifters, Wave Gliders, an AutoNaut, and biogeochemical Argo floats). These mapped the ocean down to 1000 m or more, simultaneously across both the Tradewind Alley and the Boulevard des Tourbillons (Fig. 2). These measurements have resulted in an unprecedented view of a large spectrum of ocean temporal and spatial scales across different oceanic environments.

The richness of structure observed in the upper ocean during EUREC^{4}A can be quantified by the distribution of surface temperature fronts. All seagoing platforms contributed to observing the upper-ocean temperature structure, surveying a wide region and a large spectrum of ocean scales, and thus can contribute to this measure of upper-ocean variability. An example from one such platform, a Saildrone, is shown in Fig. 15. The sensitivity of frontal density gradients to spatial resolution was explored by subsampling data from 0.08 to 100 km (Fig. 15). For each length scale, the percentage frequency of each density gradient was calculated. This analysis demonstrates that smaller length scales yield larger density gradients. The largest gradients were found at spatial scales of only 1 km and were associated with strong, local freshening. These are believed to be associated with small-scale, but intense, rain showers, a potentially far-reaching idea given the importance of rain for linking processes at different scales in the atmosphere (e.g., Sect. 3.2). The analysis further documents self-similar (power law) scaling between 19 and 1900 km with a slope of −2.3. There is evidence of a scale break at around 25 km. Surface quasi-geostrophic turbulence generally predicts a slope of −5/3 or steeper (Callies and Ferrari, 2013; Rocha et al., 2016; Lapeyre, 2017).
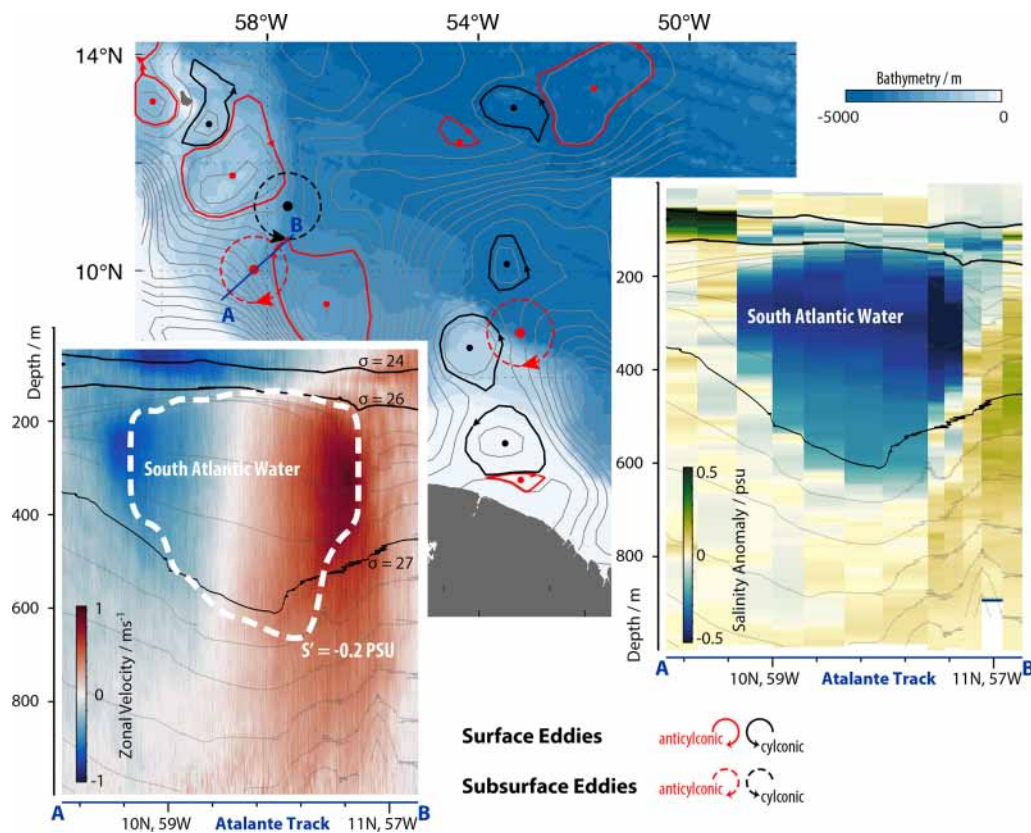
Figure 16. Eddies in the Boulevard des Tourbillons (map) with vertical cross section (A–B transect near 10° N, 58° W on the map) showing ship acoustic Doppler current profiler (SADCP) currents from the R/V *Atalante* (bottom left) and salinity from CTD casts (right). Surface-eddy field derived from satellite altimetry (Pujol et al., 2016). Eddy contours are detected automatically by the TOEddies algorithm (Laxenaire et al., 2018). The position of subsurface eddies (200 to 600 m deep) as identified from the eddy detection method (Nencioli et al., 2010) applied to vector currents measured by SADCPs are shown by red circles. A subsurface eddy freshwater anomaly is indicative of South Atlantic origins.

A wide array of instruments deployed from all four ships (CTDs, underway CTDs, mounted vessel profilers, microstructure profilers, XBTs, XCTDs, Doppler current meter profilers, five BGC Argo floats) and the seven underwater gliders (e.g., Fig. 5) profiled water properties and ocean currents. This array of measurements, guided by near-real-time satellite data and real-time ship profiling, revealed a surprisingly dense and diverse distribution of mesoscale eddies. All of the measured eddies captured by satellite data (Fig. 16) were shallow, extending to a depth of about 150 m (Fig. 16) and transporting warm and salty North Atlantic tropical water swiftly northward. Below but not aligned with the surface structures and separated by strong stratification, large subsurface anticyclonic eddies (and on some occasions cyclonic eddies) extended from 150 to 800 m and carried large quantities of water from the South Atlantic northward. An example sampled by the R/V *Atalante* along a southwest-to northeast-aligned transect near 50° N and 58° W is illustrated in Fig. 16. Here a ca. 200 km eddy characterized by a 0.2 PSU freshwater anomaly was measured carrying water, which was likely subducted in the south Atlantic, northward.

The anomaly was associated with a circulation of $\sim 1\,\mathrm{ms}^{-1}$ with maximum velocities near 300 m extending downward to a depth of about 800 m. EUREC[4]A observations such as these will be essential for understanding the complex dynamics of the upper ocean and the extent to which they can be captured by a new generation of kilometer-scale coupled climate models.

3.5 Air–sea interaction

What distinguished EUREC[4]A from the many previous campaigns focused on air–sea interaction was its interest in assessing how circulation systems, in both the ocean and the atmosphere, influence surface exchange processes. These interests extended to interactions with ocean biology and their impact on both CO_2 exchange and profligate amounts of seaweed (*Sargassum*) that have, in past years, developed into a regional hazard. To study these processes EUREC[4]A made use of a flotilla of uncrewed devices and a wealth of nadir-staring airborne remote sensing, specifically designed to characterize the air–sea interface on a range of scales.
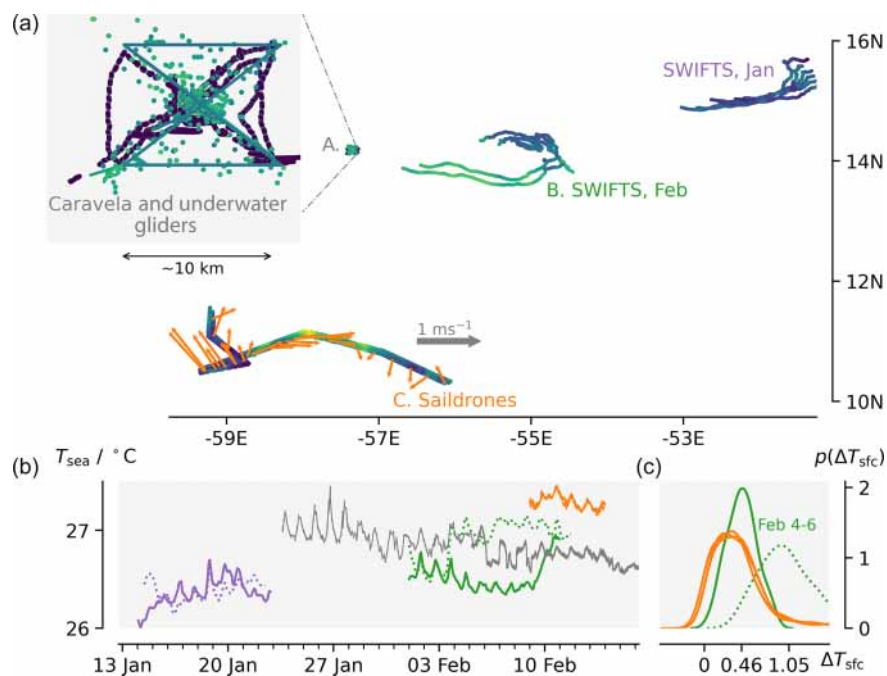
Figure 17. Near-surface temperature (T_{sea}) from drifters and gliders in the three EUREC⁴A study regions. Panel (**a**) shows the tracks of the instruments colored by T_{sea}. The magnification (upper left) expands the domain of the Caravela (and underwater glider) measurements in Region A (near $57°$ W). January and February SWIFT buoy (T_{sea} at -0.3 m) deployments in Region B. Saildrone (T_{sea} at -0.5 m) measurements across an eddy near $11°$ N, with anti-cyclonic currents (at -5 m) shown by vectors, in Region C. Panel (**b**) shows time series of T_{sea} measurements by the different instruments. Probability density, p, of air–sea temperature differences measured by two SWIFT buoys between 04:00 UTC 4 February and 14:00 UTC 6 February (**c**).

Ocean eddies, fronts, and filaments influence the atmosphere by perturbing air–sea surface fluxes (Chelton and Xie, 2010; O'Neill et al., 2012) – a process that may also feed back on the ocean by causing a damping of the (sub)mesoscale activity (Renault et al., 2018). As an example, Sullivan et al. (2020) use large-eddy simulation to show how small-scale ocean fronts perturb the boundary layer through its depth, giving rise to circulations on scales much larger than that of the boundary layer, or of the front itself (their Fig. 12). These lead to large perturbations in vertical mixing and, one can speculate, on patterns of cloudiness. Similarly, clouds influence the downward longwave and shortwave irradiance, which influences both the sea surface temperature and atmospheric temperatures directly, something that Naumann et al. (2019) have shown to commensurately power (2 to 200 km) circulations.

In the area near and within the EUREC⁴A-Circle (Region A), measurements sought to quantify how surface exchange processes vary with circulation (cloud pattern) regime. Measurements by Caravela (an AutoNaut) and three underwater gliders characterized the air–sea interface in a small, and spatially fixed, (ca. 10 km) region in this domain (Fig. 17). These measurements help untangle spatial from temporal variability, with both a secular (seasonal) cooling of surface waters over the course of the campaign and a variable, but at times

pronounced, diel cycle (Fig. 17). In addition, CTD casts, lower atmospheric profiling (with a mini-MPCK and a quadcopter), and eddy-covariance measurements from an outrigger mast were performed by the R/V *Meteor* as it steamed up and down the $57.25°$ W meridian bisecting the EUREC⁴A-Circle just upwind of Caravela's box. Rounding out the measurements in this region were low-level Twin Otter, ATR (as part of its "L" pattern) legs, and BOREAL UAS measurements, as well as airborne remote sensing of sea surface temperatures along the EUREC⁴A-Circle by HALO. Based on preliminary analyses, these measurements are proving useful in quantifying the diel cycle in both the upper ocean and in the lower atmosphere.

Effects of ocean sub-mesoscale processes on air–sea interactions were the focus of measurements in Region B (Fig. 1). On two occasions the R/V *Ron Brown* deployed six SWIFT drifters (spar buoys) in regions of surface heterogeneity: once in January near the NTAS buoy and again in early February near $55°$ W. The deployments were performed and coordinated with further measurements by the R/V *Ron Brown*, as well as by the P-3, two Wave Gliders, and a Saildrone. The P-3 (see also Figs. 4 and 2) dropped AXBTs around the SWIFTS, quantified air–sea exchange with near-surface flight legs, and surveyed the near-surface wind and wave fields using remote sensing. Figure 17 documents how, dur-
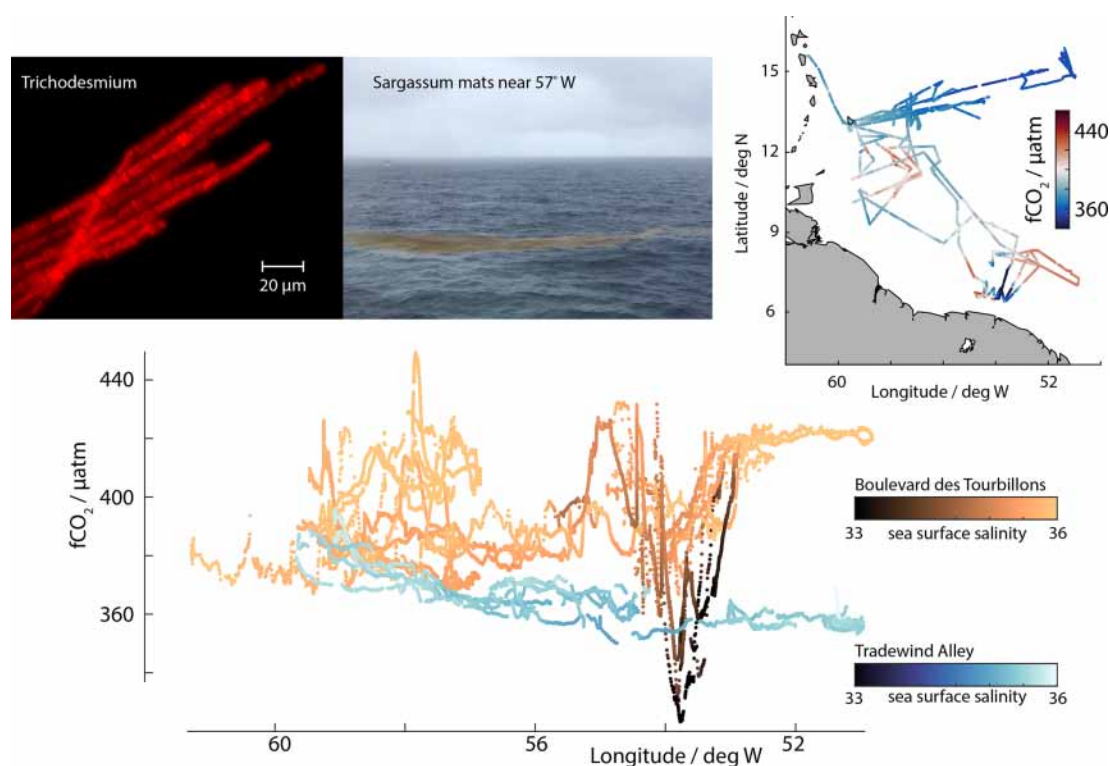
Figure 18. CO$_2$ fugacity (fCO$_2$) measurements from different surface vessels (upper right) and versus longitude (lower). The presentation contrasts strong variability in fCO$_2$ in association with eddies and salinity variations along Boulevard des Tourbillons (orange in lower panel, track in upper right) versus in the Tradewind Alley (blues). Microscopic/epifluorescence image of several filaments of *Trichodesmium*, an N$_2$-fixing cyanobacterium that is found in the region (upper left), and mats of seaweed (*Sargassum*, photo by Wiebke Mohr, upper center) which were frequently observed and difficult to navigate from some of the uncrewed surface vehicles.

ing the February deployment, the SWIFTS sampled large 0.5 K mesoscale (ca. 30 km) variability in sea surface temperature (SST) features. This variability gives rise to air–sea temperature differences twice as large as the baseline, as inferred from the average of measurements over longer periods (i.e., as shown by the Saildrone data, orange lines) and is characteristic of the SWIFT data away from the local feature in surface temperatures (e.g., green solid line in Fig. 17).

In the Boulevard des Tourbillons (Region C), coordinated sampling between Saildrones and two research vessels aimed to quantify mesoscale and submesoscale air–sea interaction. Submesoscale variability and strong near-surface currents, with a circulation indicative of an NBC ring, were measured by the Saildrones (Fig. 17). These measurements were coordinated with the activities of the R/V *Atalante* and R/V *MS-Merian*, as well as three underwater gliders (e.g., Fig. 4). Extensive vertical profiling, also by high-speed underway CTDs, aimed to quantify the impacts of submesoscale fronts and filaments and mesoscale eddies on surface exchange processes, and vice versa. Being able to resolve the thermal structure of the upper ocean should also help quantify the importance of the $O(0.3 \, \text{K})$ cool-skin effect and diurnal warm-

ing just below the skin layer (Fairall et al., 1996) on ocean mixing and air–sea exchange.

Factors, including the role of meso- and sub-mesoscale variability, influencing air–sea gas exchange were also studied. pCO$_2$ measurements were made on the R/V *Atalante*, R/V *MS-Merian*, and the R/V *Ron Brown* (Fig. 18). In addition, both the R/V *MS-Merian* and R/V *Meteor* regularly sampled water at four different depths (selected based on chlorophyll concentrations) for N$_2$ fixation and primary production rates as well as potential aerobic methane production. DNA- and RNA-based sequencing will additionally be performed on these water samples to identify diazotrophic community members, potentially including so far unrecognized members. Furthermore, large floating mats of seaweed (genus *Sargassum*) were observed from all crewed platforms. On the R/V *MS-Merian*, to investigate if, and to what degree, this biomass and primary production can be supported by local N$_2$ fixation, incubation experiments including stable isotopes were conducted on seaweed samples that were collected underway. In addition to extending studies of air–sea interaction to incorporate chemical and biological processes, EUREC⁴A may also shed light on the role of meso- and sub-

mesoscale ocean circulations on these chemical and biological processes.

3.6 Benchmarks for modeling and satellite retrievals

The range of scales and types of processes that can presently be captured by both satellites and models, and the extent to which they were integrated into EUREC[4]A's experimental design (see Bony et al., 2017), allows EUREC[4]A to address questions that could not be addressed with data from earlier field studies. For instance, what resolution is required for atmospheric models with an explicit (fluid-dynamical) representation of clouds and convection to represent the vertical structure of the lower troposphere, and its interaction with mesoscale vertical motion and upper-ocean variability, within the observational uncertainty? The fine scale of the EUREC[4]A measurements also makes it possible to quantify satellite retrieval uncertainty, for instance for measurements of small-scale precipitation features, cloud microphysical properties, or column energy budgets (Illingworth et al., 2015).

For these purposes EUREC[4]A was closely coordinated with efforts to develop and test a new generation of Earth-system models. Recently, following the pioneering efforts of Japanese colleagues (Tomita et al., 2005), a number of groups in other countries have demonstrated – within the DYAMOND[5] project (Stevens et al., 2019c) – the capability of performing kilometer-scale simulations on global (atmospheric) grids (Satoh et al., 2019). A follow-up, called DYAMOND-Winter, is extending this capability to also include coupled global models and has been coordinated to simulate the EUREC[4]A period. DYAMOND-Winter simulations are being initialized from observational analyses on 20 January and run for at least 40 d. With grid scales of a few kilometers in the atmosphere (and ocean for coupled runs) the simulations explicitly represent scales of motion similar to those observed, all as part of a consistently represented global circulation. This enables investigations of processes influencing the mesoscale organization of fields of shallow convection, including the possible role of surface ocean features, as well as a critical evaluation of the simulations.

An example of an uncoupled DYAMOND-Winter simulation using ICON is given in Fig. 19. The simulated cloud fields exhibit rich mesoscale variability whose structure, while plausible, begs a more quantitative evaluation. The combination of the field measurements and simulations with realistic variability on the mesoscale will aid efforts to test retrievals of physical quantities from satellite radiances. This should make it possible to establish a self-consistent and quantitative understanding of controls on cloudiness.

In addition to the global coupled modeling activities, coordinating modeling activities using much-higher-resolution

---

[5]the DYnamics of the Atmospheric general circulation Modeled On Non-hydrostatic Domains

(meters to tens of meters) simulations of the ocean, atmosphere, and the coupled system over a limited area are ongoing. These include idealized simulations with doubly periodic boundary conditions, atmospheric simulations designed to track the Lagrangian evolution of the flow, and simulations with open boundaries matched either to meteorological/oceanographic analyses or the free-running global simulations. Few if any field studies have benefited from such a rich complement of modeling activities.

Some of the challenges to evaluating these simulations are illustrated with the help of preliminary, but idealized, large-eddy simulations with the forcing specified based on preliminary data in a manner similar to what has been adopted in past studies (e.g., Stevens et al., 2005; vanZanten et al., 2011), albeit (in the present case) over considerably larger domains. Figure 20 shows, with the help of a satellite image, the degree of mesoscale cloud variability. This apparent whimsicality suggests that, given the imprecision in the forcing and the cloud retrievals, assessing the magnitude of systematic biases in the simulations will be a challenge. In this case, the simulations performed for the mean conditions in the vicinity of "D" seem implausible. The challenge will be to assess to what extent this reflects imprecision in the forcing, of the sort that differentiates the different marked regions in the figure.

Given a demonstration that fine-scale models can quantitatively represent the macro-structure of the observed clouds, EUREC[4]A measurements are expected to provide benchmarks for the simulation of cloud microphysical process. This would allow the first ever evaluation of the ability of microphysical models, which depend on a variety of parameterized processes, to quantitatively represent precipitation formation processes in realistically simulated cloud fields. Previous attempts (Ackerman et al., 2009; vanZanten et al., 2011) at making such an evaluation have highlighted large differences in models, but it remains unclear to what extent these differences are due to the representation of cloud macrophysics versus microphysics. Greater confidence in the fidelity of these simulation approaches will also greatly benefit their application to questions in remote sensing.

3.7 Scientific outreach and capacity building

A core, and hopefully sustainable, feature of the EUREC[4]A field campaign was the rich human and scientific interactions with the Barbadian public, the regional research community, and the larger community of scientists from outside of the region. Activities that permitted these exchanges included operational support for flight planning, inclusion in flight teams and on-ship data collection teams, weekly seminars, a larger symposium, and scientific outreach to schools and to the general public. A total of more than 25 researchers from the region as well as representatives of regional governments contributed to the data collection. This participation was essential not just for meeting EUREC[4]A's original objectives, but
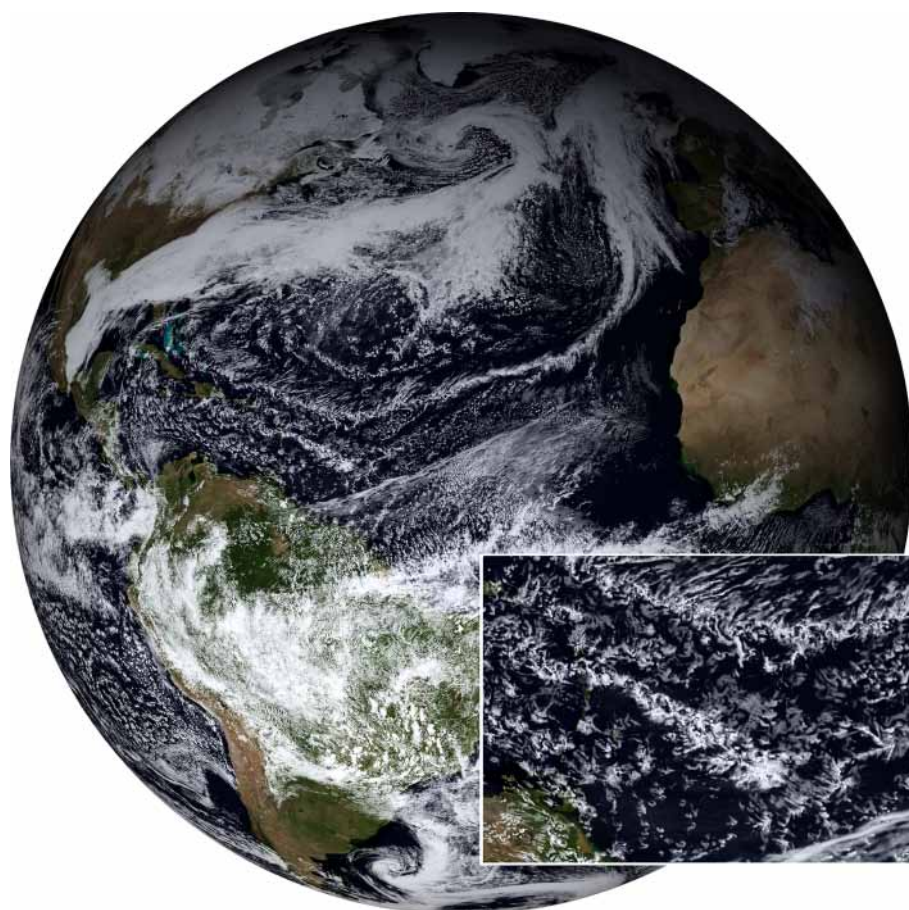
Figure 19. Global 2.5 km mesh simulations performed by ICON as part of DYAMOND-Winter for the EUREC[4]A period. The snapshot, with a magnification over the study region to show the degree of detail in the simulations, was taken from 2 February of a simulation initialized on 20 January and allowed to freely evolve thereafter.

it also expanded the scope of activities to include the development of regional climate resilience and capacity building in the use of advanced weather and climate early warning systems.

3.7.1 Operational support

Daily operational meetings were hosted at a facility shared by the Barbados Meteorological Service and the Department of Civil Aviation. Scientists from national meteorological services across the region supported the effort by providing daily weather forecasts, which helped to coordinate the measurements for the following days. The European Centre for Medium-Range Weather Forecasts and national weather services in France, Germany, the Netherlands, the UK, and the USA supported these activities by providing access to output from global models at 10 km resolution and regional forecasts made specially for the region on kilometer-scale grids. The daily weather discussions provided an opportunity for scientists from different teams to discuss and analyze the early results of the campaign and the perspectives ahead. For

example, during one of these meetings it was learned that the mesoscale cloud patterns identified as "fish" in the recent literature have long been termed "rope" clouds by the regional forecast community.

3.7.2 Symposium and scientific seminars

Knowledge transfers of immense value were facilitated by the organization of regular scientific presentations that provided an opportunity for exchange among EUREC[4]A participants and researchers at the Caribbean Institute for Meteorology and Hydrology (CIMH). It is expected that such exchanges will sustain collaborations well beyond the campaign. Keynote presentations at the Barbados Museum and Historical Society brought to a general audience the goals of the EUREC[4]A campaign, the very early history of meteorology on Barbados, and issues or relevance to climate change and related adaptation.

Campaign participants also celebrated the 50th anniversary of the Barbados Oceanographic and Meteorological EXperiment (BOMEX) field campaign with a 2 d public sympo-
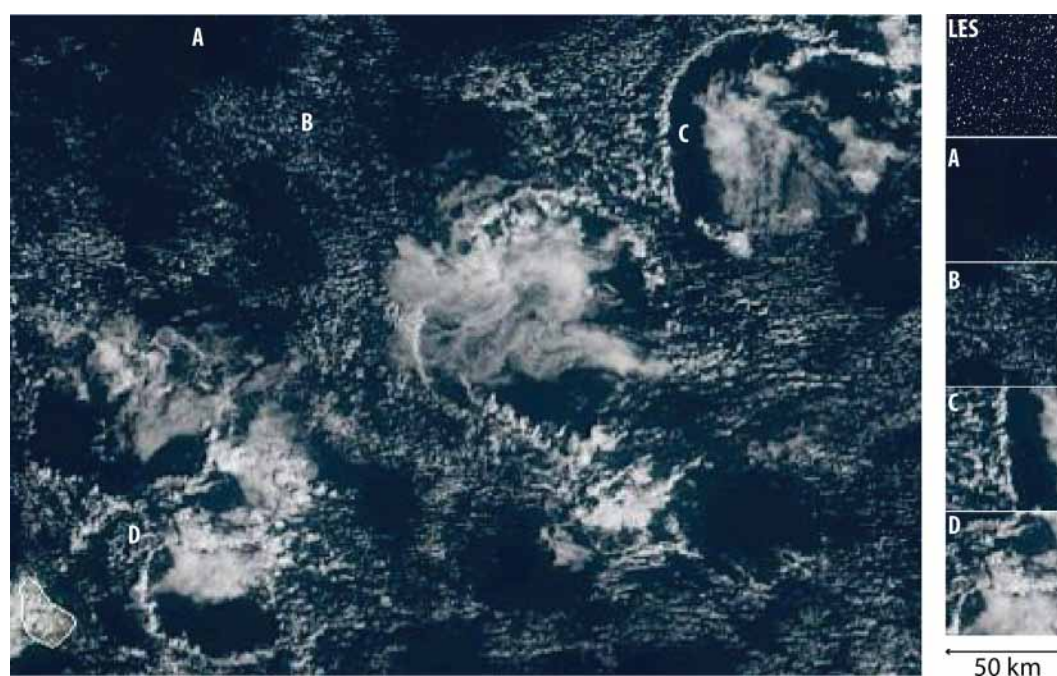
Figure 20. Geostationary satellite image showing the cloud field in the measurement area on 5 February 2020. Snapshots of cloud fields over 50 km × 50 km subdomains labeled "A" to "D" are compared to large-eddy simulation. The large-eddy simulation employed a 100 m mesh, doubly periodic horizontal boundary conditions, and horizontally homogeneous mean forcing is estimated from measurements in the vicinity of subdomain "D".

sium entitled "From BOMEX to EUREC[4]A". The symposium brought together a varied audience, including regional and international scientists, EUREC[4]A participants, and students from the University of the West Indies Cave Hill Campus (Fig. 21). The symposium provided an opportunity to reflect upon the evolution of climate research during the past 50 years. From fascinating speeches by BOMEX veterans, to presentations describing the state of present-day understanding as expressed in EUREC[4]A's objectives, the symposium helped contextualize the efforts being made as part of EUREC[4]A.

In December 2019, prior to the start of the EUREC[4]A campaign, the Caribbean Meteorological Organization (CMO) Headquarters Unit and the University of Leeds, with the assistance of CIMH, organized a Caribbean Weather Forecasting Initiative workshop at CIMH to promote knowledge exchange between researchers and forecasters from CMO members and other Caribbean states. This activity supported the EUREC[4]A forecast testbed, in which many of the regional forecasters who participated in the workshop provided some of the daily forecasts previously discussed.

3.7.3 Scientific outreach in schools and facility visits

Scientific outreach activities, such as school visits and scientific open houses, sought to sensitize the public, in particular school children, to the EUREC[4]A program and its impor-

tant role in addressing issues of severe weather and climate change. Together with the CIMH, and the Barbados Ministry of Education, 10 visits to primary and secondary schools in Barbados were arranged. Simple experiments were designed and performed with the children to help build intuition as to the underlying atmospheric and ocean processes relevant to EUREC[4]A's scientific objectives, not to mention the weather phenomena that surrounds them on a daily basis. These outreach efforts aimed to raise awareness in ways that would increase the resilience of the region to weather and climate extremes, to support citizen science, and to expose young people to scientific career paths.

The open houses consisted of guided tours of many of the measurement platforms. This included tours of the research ships; visits to the BCO at Deebles Point, St. Philip (where visitors could help launch radiosondes); the aerosol measurement facility on nearby Ragged Point; BOREAL, Skywalker, and CU-RAAVEN drone launches at Morgan Lewis Beach, St. Andrew; and tours of the POLDIRAD radar at Colleton, St. John. As an informal complement to the symposium, the outreach activities provided a window into the daily life of the campaign and gathered a diverse audience, from local Barbadians to the scientists involved in EUREC[4]A. The success of EUREC[4]A's outreach efforts is perhaps best exemplified by the ad hoc team of young engineers (Fig. 22) that helped flight proof the drones before their launch from Morgan Lewis Beach.

Earth Syst. Sci. Data, 13, 4067–4119, 2021

https://doi.org/10.5194/essd-13-4067-2021

Figure 21. "From BOMEX to EUREC^{4}A" symposium participants (photo by Frédéric Batier). Pat S. R. Callender (front, third from right) and Clyde Outram (front center, with cane) participated in BOMEX.

Further activities included members of the scientific team planting trees as part of Barbados' "We Planting" initiative. In parallel to the scientific campaign, two French filmmakers also visited Barbados for the duration of the EUREC^{4}A field campaign to shoot a documentary combining scientific, cultural, and historical elements of the island of Barbados. From their material an additional short scientific documentary of the campaign was created and is provided as a Supplement (video asset) with this paper.

4 Scientific practice

EUREC^{4}A advanced a culture of open and collaborative use of data. It did so by initiating a series of discussions, starting well before the field campaign and culminating in a document outlining principles of good scientific practice. In arriving at these principles emphasis was placed on understanding the differing cultural contexts in which data are collected. For instance, the degree to which measurements are made by individual investigators, or made for investigators by institutions, were often colored by different national practice. Differences in how measurements are made lead to differences in expectations as to how the resultant data should be made available and used and thus reflect this national color-

Figure 22. Local children helping to evaluate air worthiness of CU-RAAVEN UAS prior to launch from Morgan Lewis Beach (photo by Sandrine Bony).

https://doi.org/10.5194/essd-13-4067-2021

Earth Syst. Sci. Data, 13, 4067–4119, 2021

ing. EUREC^{4}A defined "good scientific practice" in terms of four principles, summarized below:

1. To actively support the initial dispersal of data by making (even preliminary) data available to *everyone* as quickly as possible through the AERIS archive.

2. To publish finalized data in ways that ensure open and long-term availability and bestow appropriate credit on those who collected it.

3. To actively attempt to meaningfully involve those who collected data in their analysis at the early stages of their use.

4. To provide clear, timely, and unprompted feedback on the use of the data, both by the analysis community for the instrument groups and vice versa.

Most of the data collected during EUREC^{4}A are already available on the AERIS archive, much of them are described by data papers published, or being published, as part of this ESSD special issue.

Examples of "bad practice" were also outlined – for example (i) in the first years after the campaign using data for specific analysis without asking the data provider whether/how this analysis overlaps with his/her current analysis efforts, (ii) using someone's data to write a paper and then sending the paper to the data providers only as it is about to be submitted and offering authorship, or (iii) by assigning co-authorship on the basis of someone's status rather than through substantive contributions. "Good practice" would have been to intellectually involve the data provider at an early stage of the study. "Good practice" also recognized the importance of providing intellectual space for young scientists to independently develop their ideas – giving them a bit more time to recognize and reach what a more experienced colleague might more immediately recognize as low-hanging fruit.

Authorship of the present paper recognizes all technical/scientific contributions to the data collection. The ways in which each author contributed to EUREC^{4}A are summarized in the Supplement on author contributions.

4.1 Data

The data collected during EUREC^{4}A will, in different stages of development, be uploaded and archived on the AERIS data center. The AERIS data center is part of the French Data Terra research infrastructure, which has the objective to facilitate and enhance the use of atmospheric data, whether from satellite, aircraft, balloon, or ground observations, or from laboratory experiments. It generates advanced products and provides services to facilitate data use, to prepare campaigns, and to interface with modeling activities.

In addition, emphasis is being placed on the publishing of datasets through a special collection of articles in *Earth System Science Data*. Many of these data papers will involve the construction of cross-platform datasets, for instance for the upper-air network, or dropsondes, isotope measurements, or classes of remote sensors. At the end of the data collection phase, all data on AERIS will be mirrored by the Caribbean Institute for Meteorology and Hydrology in Barbados.

4.2 Environmental impact

EUREC^{4}A was motivated by an interest to better anticipate how Earth's climate will change with warming. This makes it all the more relevant to ask how EUREC^{4}A exacerbates the problems it attempts to understand, or more pertinently, whether it made appropriate use of scarce resources. The first step in answering this question is to estimate the magnitude of its environmental impact. We do so here mostly in terms of EUREC^{4}A's carbon footprint, which we estimate (see Appendix A for details) to be 5000 t of CO_2. The marginal increase – EUREC^{4}A took place at the expense of other campaigns – is of course much less. The main contribution to the carbon footprint was from fossil fuels (kerosene and diesel) used to power the research platforms. The travel of the participating scientists contributed non-negligibly (5 %) to EUREC^{4}A's carbon footprint and provides context for the total emissions.

When learning about EUREC^{4}A many people become concerned about the environmental impact of the dropsondes – a concern shared by some of the present authors. The sondes have been designed to sink to the ocean floor after descending to the sea surface. As elaborated upon in Appendix A, this along with the choice of materials (including batteries), and their small size (which with planned modifications may be reduced by a further factor of 2), results in the environmental impact of the use of even a very large number of sondes themselves being minimal. One hesitates to call any environmental impact negligible, but compared to many of the other activities – let alone the initial emotional response to the idea of throwing objects out of an aircraft – this is probably an apt description.

The potential of using yet smaller sondes, or smaller platforms in general, to further reduce environmental impacts was vividly illustrated by EUREC^{4}A's extensive use of robotic sensors (uncrewed aerial systems, UASs; autonomous ocean-observing platforms, AOOPs). In many cases these provided more agile and less energy intensive ways of sampling the environment. For instance, the Saildrones, Wave Gliders, and AutoNaut (Caravela) make use of renewable energy sources for their propulsion (e.g., wind for Saildrones, waves for the Wave Gliders and AutoNaut), and for their scientific sensors (solar panels).

Validation for EUREC^{4}A's use of the resources was experienced not just through the data collected, but also through the social interactions that the campaign enabled. These, as discussed in Sect. 3.7, were expressed in bonds of friendship that were established and through the many opportunities that

were presented through the outreach and capacity building activities (Fig. 22). Further validation of EUREC[4]A's use of resources depends on how the gained data advances scientific understanding to help humanity. This ultimately depends on what is done with the data – something over which we, the authors, have considerable influence and responsibility. We very much hope this realization will motivate a determination to learn as much as possible from the EUREC[4]A measurements and that the importance of supporting such efforts is recognized by funding agencies. We also acknowledge the imperative this creates to make the hard-won data easy to access and use, e.g., through data papers, and to also communicate what we learned from our efforts, as widely and freely as possible.

5 Data availability

A standardized (CF-1.8 compliant) track data set provides the trajectory data for the 59 mobile platforms deployed during EUREC[4]A. Trajectories are described by the latitude and longitude (and altitude or depth as applicable) of each platform as a function of time. Airborne platforms are segmented by flight. The data are freely available on the AERIS archive (https://doi.org/10.25326/165, Stevens, 2021). The EUREC[4]A film is freely available on the AERIS archive (https://doi.org/10.25326/224, Lena et al., 2021).

6 Conclusions

Field studies are commonplace, and each – by virtue of taking a snapshot of nature at a given point in time and space – is unique and unprecedented. This is in itself not particularly remarkable. Field studies involving such a large number of investigators and such a large degree of coordination, as was the case in EUREC[4]A, are uncommon, but also this represents little more than an organizational achievement. Moreover, many of the questions EUREC[4]A attempted to address have been the focus of past field studies. For instance, air–sea interaction was at the heart of the original Barbados field study, BOMEX (Holland and Rasmusson, 1973). Likewise a great number of studies, most recently the Convective Precipitation Experiment (Leon et al., 2016) and Rain in Cumulus over the Ocean (RICO Rauber et al., 2007), had warm-rain formation processes as a central focus. The influence of boundary layer processes on cloud formation was already extensively studied by Malkus (1958) and again more recently by Albrecht et al. (2019). Field studies to measure aerosol–cloud interactions are myriad and include very large international efforts such as the Indian Ocean Experiment (Ramanathan et al., 2001). And with new insights from modeling, an increasing number of studies have begun to focus on ocean meso- and submesoscale dynamics (Shcherbina et al., 2013; Buckingham et al., 2016; D'Asaro et al., 2018). What made EUREC[4]A an improvement was neither its size nor

many of its specific questions – rather it was EUREC[4]A's ability to quantify a specific process: the link between circulation and cloudiness. Doing so opened the door to characterizing the totality of processes believed to influence the structure of the lower atmosphere and upper ocean in the region of the trades. This is what made EUREC[4]A special.

The execution of EUREC[4]A was successful. All of the measurements we set out to make have been made. For some key quantities, such as the mean mesoscale vertical motion field, preliminary analyses (e.g., Fig. 9) suggest that the measurements sampled substantial variability, which bodes well for testing the hypothesized link between cloudiness and cloud-based mass fluxes. The analysis of other measurements, such as those that aim to quantify clouds, is more delicate and ongoing. We anticipate that each step of the subsequent analysis of the EUREC[4]A data will teach us a great deal more about the ways of clouds, how they couple to circulation systems on different scales, how they influence and are influenced by the upper ocean, the extent to which they are susceptible to perturbations in the aerosol environment, and how precipitation links processes across scales. At the very least a better quantification of these sensitivities should help us understand to what extent a warmer world will express the majesty of the clouds in the trades less markedly.

Appendix A: Estimates of environmental impact

With a specific density of $0.82\,\mathrm{kg\,L^{-1}}$ we can compute the total CO_2 emissions from aircraft operations as $629\,497\,\mathrm{L} \times 3\,\mathrm{kg\,CO_2\,kg}$-fuel $\times 0.82\,\mathrm{kg}$-fuel $\mathrm{L^{-1}} = 1\,548\,562\,\mathrm{kg}$ of CO_2 emissions, or roughly 1500 t.

Estimates of the fuel consumption for the research vessels are larger as they operate around the clock and support the life of a community of scientists and their laboratories at sea. They are also more roughly estimated. We begin with numbers from the R/V *Meteor*, which burns sulfate-reduced diesel. Its burn rate is estimated as $5000\,\mathrm{L\,d^{-1}}$ when stationary and as much as twice that much when under way. Given that the ships were generally steaming but with station work mixed in, we adopt a burn rate of $8000\,\mathrm{L\,d^{-1}}$. Diesel is denser than kerosene and produces more CO_2 per kilogram. We adopt a conversion of $3.15\,\mathrm{kg}$ of CO_2 for every kilogram of diesel and a density of $0.85\,\mathrm{kg\,L^{-1}}$. Based on this we estimated that the R/V *Meteor* burned $21\,420\,\mathrm{kg\,d^{-1}}$. The reported fuel use for the R/V *Ron Brown* was $79\,922$ gallons or $363\,333\,\mathrm{L}$, which included the ferry to and from a home port. This fuel burn corresponds to $972\,823\,\mathrm{kg}$ of CO_2. Assuming 35 d of operations, this corresponds to a burn rate of $10\,380\,\mathrm{L\,d^{-1}}$. For our estimates we adopt the $8000\,\mathrm{L\,d^{-1}}$ burn rate for all the ships and estimate 5 d of ship ferry time, so for four ships each with $30\,\mathrm{d^{-1}}$ of ship time we end up with a total emission of 3000 t of CO_2, which is about twice the direct emissions from the research aircraft. The ship numbers are not offset by the reduced personal emissions of those on the ship, i.e., who do not need hotels, or rental cars, or the operation of their home labs, and often have reduced travel, but this is likely minor.

We estimated that 200 people traveled to EUREC^{4}A. If each is further assumed to have flown $15\,000\,\mathrm{km}$ (about the round-trip distance from Frankfurt to Grantley Adams International Airport in Barbados) in economy class, then we can adopt an emission estimate of $75\,\mathrm{gCO_2\,km^{-1}}$ per passenger (from Atmosfair for a non-stop flight with an Airbus 340–500). This $200 \times 15\,000\,\mathrm{km} \times 75\,\mathrm{gCO_2\,km^{-1}} = 225\,000\,\mathrm{kg}$ of CO_2 emissions. More modern aircraft have substantially reduced emissions ($60\,\mathrm{g\,km^{-1}}$), then again carbon-offsetting schemes often estimate a 3-fold larger equivalent emission due to the inclusion of other factors.

The environmental impact of the sondes is informed by life cycle analyses that Vaisala has commissioned for their radiosondes, as well as our own analysis. The life cycle analysis identified "the production of the printed circuit board and the electricity used during the assembly [as having] the most significant effect on the environmental impacts". But this analysis did not consider the impact of the waste, beyond issues of things like battery toxicity. In this regard the lithium batteries used by the sondes had the least environmental impact of all available choices, i.e., alkaline or water-activated batteries. We estimated that $1.2\,\mathrm{kg}$ of lithium was deposited with the sondes in the ocean – which is roughly equivalent to what would be found naturally in the seawater displaced by one of the EUREC^{4}A research vessels. Plastic sensor casings, parachutes, and/or remainders of the latex balloon add an additional impact. This is minimized by designing the sondes to sink to the ocean floor. Efforts are ongoing to identify different materials to further reduce the environmental impact of the sondes. One also questions whether the potential energy loss by the sonde could be used to power the instrumentation and whether a different and smaller sonde could forgo the use of a parachute.

Appendix B: Platforms

B1 BCO

The Barbados Cloud Observatory (BCO) is located at the far east of Barbados ($13°\,09'\,45.8''$ N, $59°\,25'\,43.8''$ W) and started operation in April 2010 with a growing set of different instruments for cloud observing and recording. During the whole EUREC^{4}A campaign the BCO was staffed for radiosonde launching and maintenance. Measurements at Ragged Point listed below were made by the University of Miami, the University of Manchester, and the Max Planck Institute for Chemistry. DLR and CIMH staff operated POLDIRAD at St. John ($13°\,10'\,49''$ N, $59°29'\,47''$ W; altitude 240 m).

B2 NTAS

The Woods Hole Northwest Tropical Atlantic Station (NTAS) is a surface mooring maintained at approximately $15°$ N, $51°$ W since 2001 by means of annual mooring "turnaround", i.e., deployment of a refurbished mooring and recovery of the old mooring. The refurbished mooring has freshly calibrated sensors and is deployed first. A 1 to 2 d period of overlap before recovering the old mooring provides intercomparison data and allows consecutive data records to be merged. Meteorological variables suitable for estimation of air–sea fluxes from bulk formulas, as well as upper-ocean variables and deep ocean temperature and salinity, are measured. Data are available from the Upper Ocean Processes Group at the Woods Hole Oceanographic Institution.

B3 ATR

The French ATR-42 aircraft, operated by SAFIRE (Service des Avions Français Instrumentés pour la Recherche en Environnement, a national research infrastructure of Météo-France/CNRS/CNES), is a turboprop aircraft that has the capability of flying in the lower troposphere (ceiling at about 8 km). During EUREC^{4}A it flew 19 missions on 11 d, from 25 January to 13 February 2020, totaling 91 flight hours. It generally flew two missions per day. Each mission was about 5 h long, including a transit time from the airport to the EUREC^{4}A-Circle of 20 min in each direction. Most mis-

Table A1. Fuel consumption from EUREC^{4}A crewed aircraft. Some fuel burn rates were reported in pounds (lb) and were converted to liters using a conversion of 1.76 lb L^{-1}.

Aircraft	Total fuel/liters	Notes
ATR	92 348	Includes cross-Atlantic transit from Toulouse, France.
HALO	235 493	Includes ferry from Oberpfaffenhofen, Germany.
TO	33 850	Not including ferry from Panama.
P-3	267 806	Assuming 20 h of ferry and 95 flight hours.
Sum	629 497	

sions were composed of a transit leg to the circle flown at an altitude of about 2.5 km, two or three box patterns (rectangles of 15 km by 120 km) near cloud base, two L patterns within the sub-cloud layer (near the top and the middle of the layer, cross-wind and along-wind), and a surface leg (altitude of 60 m) before a transit back to the airport at an altitude of about 4.5 km.

B4 HALO

The German research aircraft HALO (High Altitude and Long Range Research Aircraft) is operated by DLR in the configuration described by Stevens et al. (2019a), with instruments developed, certified, and operated by groups from around Germany. During EUREC^{4}A it was stationed at the Grantley Adams International Airport (GAIA, TBPB) on Barbados. It flew 13 missions out of GAIA plus two transfer flights from and to Germany, totaling in 130 flight hours. Its first local flight was on 22 January and its last on 15 February 2020. HALO is a modified twin-engine business jet (Gulfstream 550) with an endurance of over 8000 km and a ceiling of 15.5 km. Most flights were spent around 10 km altitude with a flight speed of about 190 ms^{-1}, with a typical flight pattern of two sets of 3.5 circles (each lasting about an hour) on the EUREC^{4}A-Circle separated by a 1 h excursion toward the NTAS buoy.

B5 P-3

The NOAA WP-3D Orion (P-3) "Miss Piggy" was operated by NOAA's Aircraft Operations Center. During EUREC^{4}A it flew 11 missions on 11 d totaling 95 flight hours. Its first flight was on 17 January and its last on 11 February 2020. There were three night flights on 9, 10, and 11 February, taking off between 22:00 and 23:30 local time on 8, 9, and 10 February respectively. The P-3, one of two "Hurricane Hunters", is a four-engine turboprop and operates with a maximum endurance of 10 flight hours and a maximum ceiling of 8.75 km. Flight strategies varied over the course of the experiment but included circles at or above 7 km to deploy dropsondes, slow profiles from 7 km to 500 ft/150 m for water vapor sampling, stacked straight and level legs to vertically sample horizontal variability at different heights within the cloud and sub-cloud layers, and "lawnmower" patterns at 2.75 to 3.00 km for deployment of airborne expendable bathythermographs and remote sensing of ocean surface state. Flight-level data include aircraft navigation and orientation and standard meteorological variables.

B6 TO

The Twin Otter (TO) was operated by the British Antarctic Survey (BAS). It flew 25 missions on 15 d totaling 90 flight hours. The first flight was on 24 January and the last on 15 February 2020. All flights were during daylight hours. The main objective of the TO flights was to observe the sub-cloud and cloud layers at a number of altitudes from close to the sea surface to the level of the detrainment region and above. As many clouds as possible were sampled by zigzagging to catch the clouds.

B7 Atalante

The R/V *L'Atalante (Atalante)* belongs to the French oceanographic research fleet national infrastructure and is operated by IFREMER. This 85 m long vessel is the first modern vessel of the French open-ocean fleet. The R/V *Atalante* ship time has been provided by the French operator to the EUREC^{4}A_OA project within the EUREC^{4}A umbrella. It sailed from Pointe-à-Pitre, Guadeloupe, on 20 January and started its operations in Barbados water on 21 January 2020. It navigated for more than 3000 nmi collecting ocean and atmosphere data from 6 to 15° N and 60 to 52° W and surveying the Tradewind Alley and the North Brazil Current eddy corridor (Boulevard des Tourbillons) in international waters and in the EEZ (or Exclusive Economic Zone) of Barbados, Trinidad and Tobago, Guyana, Suriname, and French Guyana. During the cruise, an underwater electric glider (Kraken) and surface drifters (including the OCARINA and PICCOLO platforms) were deployed (see respective sub-subsections).

B8 MS-Merian

The R/V *Maria Sibylla Merian* is a (95 m) long German research vessel, owned and funded jointly by the Ger-

Table B1. BCO.

Instrument	Brief description
Cloud radar (CORAL)	Metek MIRA-35 vertically staring pulsed 35 GHz Doppler cloud radar measuring radar reflectivity, linear depolarization ratio, Doppler velocity, and spectral width
Rain radar (POLDIRAD)	A scanning polarized Doppler C-band radar measuring radar reflectivity, linear depolarization ratio, Doppler velocity, spectral width, differential reflectivity, copolar correlation coefficient, and differential propagation phase
Rain radar	Metek Micro Rain Radar operating at 24 GHz to measure rain rate, liquid water content, and drop velocity
Raman lidar (CORAL)	A vertically staring backscatter lidar with attenuated backscatter at 355, 387, 407, 532, and 1064 nm measuring particle backscatter at 355 nm, water vapor mixing ratio, temperature, and humidity
Wind lidar	HALO Phononics scanning Doppler lidar measuring Doppler velocity and vertical and horizontal winds
Ceilometer	OTT CHM 15k pulsed laser cloud height detector at 1064 nm used to detect cloud-base height and lifting condensation level
Isotopic analyzer	Picarro (L2130-i) cavity ring-down laser spectrometer to measure water stable isotopologues
Radiometer (BCOHAT)	RPG HATPRO-G5 scanning radiometer at K and V band used for retrievals of columnar water vapor content, liquid water path, and rain rate
Pyrgeometer	Kipp and Zonen CGR4 sensor measuring hemispheric broadband downwelling longwave (4.5 to 42 μm) radiative fluxes
Pyranometer	Kipp and Zonen CMP21 sensor measuring hemispheric broadband downwelling and diffuse shortwave (0.285 to 2.8 μm) radiative fluxes
Pyrheliometer	Kipp and Zonen CHP1 sensor measuring direct normal shortwave (0.2 to 4 μm) radiative irradiance
All-sky camera	Vertically operating visible (hemispheric) and infrared camera to infer cloud coverage
Disdrometer	Eigenbrodt ODM470 optical sensor measuring droplet size distributions
Particle counter	Size-resolved CCN measurements (CCN-100, DMT vs. CPC 5.412 – GRIMM)
Particle counter	CPC (TSI 3750) measuring total aerosol/condensation nuclei (CN) concentration ($d > 10$ nm)
Particle sizer	SMPS (GRIMM 5.420) measuring aerosol/CN size distribution (10 to 1000 nm)
Particle sizer	WRAS (GRIMM, EDM 180) measuring aerosol/CN size distribution (0.25 to 32 μm)
Particle sizer	SMPS (TSI 3080) measuring aerosol/CN size distribution (15 to 650 nm)
Particle sizer	APS (TSI 3321) measuring aerosol/CN size distribution (0.5 to 20 μm)
Particle sizer	PAS (GRIMM 1.109) measuring aerosol/CN size distribution (0.25 to 32 μm)
Aerosol mass spectrometer	AeroMegt LAAP-ToF mass spectrometer measuring single particle aerosol composition and mixing state
Aerosol mass spectrometer	Aerodyne AMS, bulk chemical composition of non-refractory aerosol ($d < 1$ μm)
Bioaerosol sensor	Wideband Integrated Bioaerosol Sensor (WIBS-4M) measuring aerosol size distribution, three-channel fluorescence, and particle asymmetry
Aerosol filter measurements	Mass concentrations of dust and soluble ions collected daily using high volume sampling
Aerosol composition	Aerosol collection for offline analysis of mixing state and size-resolved composition
Anemometer	Gill R350 sonic anemometer to measure wind speed and wind direction

Table B1. Continued.

Instrument	Brief description
Weather sensors	Metpack (Vaisala WXT-510) to measure temperature, relative humidity, pressure, and precipitation
Weather sensors	Vaisala WXT-530 weather sensors measuring temperature, humidity, pressure, wind speed, wind direction, and rain
GNSS	Dual Trimble NetR9 GNSS receivers with Zephyr Geodetic 2 antennas for columnar water vapor content
Radiosondes	Vaisala RS41-SGP radiosondes measuring atmospheric profiles (during ascent and descent) of temperature, relative humidity, pressure, wind direction, and wind speed

Table B2. NTAS.

Instrument	Brief description
ASIMET	Air-Sea Interaction METeorology system measuring air temperature, relative humidity, barometric pressure, precipitation, wind speed, wind direction, longwave broadband irradiance, shortwave broadband irradiance, sea surface temperature, and sea surface salinity every 1 min (on surface buoy, sensors at 3 m height)
Weather sensors	Vaisala WXT-520 measuring air temperature, relative humidity, barometric pressure, precipitation, wind speed, and wind direction (sensor at 3 m height)
Thermometer	Sea-Bird SBE-39 adapted to measure air temperature every 5 min (sensor at 3 m height)
Thermometer	Sea-Bird SBE-56 fast-sampling temperature recorder measuring sea surface temperature every 1 min (in buoy hull)
Thermometer	Sea-Bird SBE-39 recording seawater temperature every 5 min (on mooring line at 5, 15, 20, 30, 35, 45, 50, 60, 65, 75, 80, 90, 100, and 110 m)
Thermometer	Star-Oddi Starmon measuring seawater temperature every 10 min (on mooring line at 110–160 m, 10 m intervals)
Wave height sensor	Xeos Brizo measuring surface wave height and period (every 60 min, with a 20 min sample interval each hour)
Acoustic Doppler current meter	Nortek Aquadopp ADCM recording horizontal velocity every 20 min (on mooring line at 5.7 and 13 m)
Current profiler	Nortek Aquapro profiler measuring horizontal velocity profile every 60 min (on mooring line at 24 m, uplooking)
Acoustic Doppler current profiler	Teledyne RDI ADCP measuring horizontal velocity profile every 60 min (on mooring line at 85 m, uplooking)
CT sensor	Sea-Bird SBE-37 measuring seawater temperature and conductivity/salinity every 10 min (on mooring line at 10, 25, 40, 55, and 70 m)
CT sensor	Sea-Bird SBE-37 measuring deep ocean temperature and salinity every 5 min (38 m above bottom).

man Research Foundation (DFG) and the German Ministry for Education and Science (BMBF). The MSM89 cruise started (17 January 2020) and ended (20 February 2020) in Bridgetown, Barbados (Karstensen et al., 2020). During the cruise various ocean and atmosphere profile measurements were carried out from the ship. In addition, underwater electric gliders and the CloudKite were deployed but are described separately (see respective sub-subsections).

B9 Meteor

The R/V *Meteor* is a 98 m long German research vessel, which is funded jointly by the German Research Foundation (DFG) and the German Ministry for Education and Research (BMBF). The M161 cruise started in Bridgetown (Barbados) on 17 January 2020, and R/V *Meteor* spent the following month in the trade wind alley east of Barbados (between 12 to 15° N and 54 to 60° W). During this time, the atmosphere

Table B3. ATR.

Instrument	Brief description
Backscatter lidar (ALIAS)	A horizontally staring backscatter lidar operating at 355 nm and detecting polarization (Chazette et al., 2021)
Cloud radar (BASTA)	A horizontally staring bistatic FMCW 95 GHz Doppler cloud radar characterizing clouds, rain, and horizontal Doppler velocity (Delanoë et al., 2016)
Cloud radar (RASTA)	An upward-looking 95 GHz Doppler pulsed cloud radar characterizing clouds, rain, vertical Doppler velocity, and Doppler spectrum
Isotopic analyzer	Picarro (L2130-i) cavity ring-down laser spectrometer measuring stable isotopologues in water vapor (including water vapor mixing ratio)
Humidity sensor	WVSS2 absolute humidity sensor (tunable diode laser absorption)
Humidity sensor	LICOR 7500 hygrometer
Humidity sensor	Campbell krypton hygrometer KH20 measuring humidity fluctuations
Humidity sensor	1011 C Buck dew point hygrometer
Humidity sensor	Enviscope capacitive sensor measuring relative humidity
Visible cameras	High-resolution visible cameras (AV GT1920C) looking sideways and downward
Particle sizer	UHSAS, measuring aerosol particle sizes from 0.06 to 1 µm
Scattering spectrometer	FSSP 300, measuring particle sizes from 0.3 to 20 µm
Cloud droplet probe	CDP/FCDP, measuring particle sizes from 2 to 50 µm
Particle imager	2D-S Stereo probe measuring particle sizes from 10 µm to 2000 µm
Liquid water sensor	LWC-300 hot-wire liquid water sensor to measure liquid water content
Pyrgeometer	Kipp and Zonen sensor measuring hemispheric broadband upwelling and downwelling longwave (4.5 to 42 µm) radiation
Pyranometer	Kipp and Zonen sensor measuring hemispheric broadband upwelling and downwelling shortwave (0.2 to 3.6 µm) radiation
Infrared radiometer	CLIMAT CE332, a downward-staring infrared radiometer measuring irradiance at 8.7, 10.8, and 12.0 µm and used to infer SST
Core instrument	The aircraft and in situ data system (aircraft state, temperature, humidity, and pressure)

above and the ocean underneath was repeatedly probed using a wealth of instruments that either were running continuously or sampled discrete stations. At the end of the campaign, R/V *Meteor* headed for its next working area. Additional measurements were carried during this transit, and the vessel arrived in Ponta Delgada (Azores, Portugal) on 3 March 2020 after a total of 6250 nmi of sailing (Rollo et al., 2020). The autonomous platforms (such as CloudKite or ocean glider) deployed from the R/V *Meteor* are described in their respective sub-subsections.

B10 Ron Brown

Sampling on board the NOAA Ship *Ronald H. Brown* took place from 7 January to 13 February 2020 and focused on the region between 57 and 51° W east of Barbados and north of 12.5° N in the trade wind alley. The overarching strategic goal of ATOMIC was to provide a view of the atmospheric and oceanic conditions upwind of the EUREC^{4}A study region. Operations of the R/V *Ron Brown* were coordinated with two Wave Gliders (245 and 247) and SWIFTS deployed from the ship, the P-3 aircraft, Saildrone 1064, and BCO (these platforms are described in their respective sub-subsections). An additional logistical objective included recovering the NTAS-17 mooring and replacing it with the NTAS-18 mooring. A third objective was to triangulate and download data from a Meridional Overturning Variability Experiment (MOVE) subsurface mooring and related Pressure Inverted Echo Sounders (PIESs). MOVE is designed to monitor the integrated deep meridional flow in the tropical North Atlantic. Additional information on shipboard sam-

Table B4. HALO.

Instrument	Brief description
Cloud radar (HAMP)	A Downward-looking high-powered Ka-band polarized Doppler cloud radar
Microwave radiometers (HAMP)	An ensemble of microwave radiometers in K, V, W, F, and G bands to estimate cloud properties, precipitation, and integrated water vapor amount
DIAL lidar (WALES)	A differential absorption lidar near 935 nm, with additional channels at 532 and 1064 nm, to characterize aerosols, clouds, and water vapor profiles
Hypersp. imager (specMACS)	A VNIR and a SWIR hyperspectral camera (0.4 to 2.5 μm) and two polarization cameras to characterize clouds, droplets, and optical thickness (Ewald et al., 2016)
Solar radiometer (SMART)	A spectral solar radiometer measuring visible and near-infrared radiation to infer cloud presence and microphysics
Infrared imager (VELOX)	A spectral IR imager to characterize clouds and measure liquid water path and SST
Infrared thermometer (V-KT 19)	An infrared thermometer channel for the VELOX to measure SST
Broadband radiom. (BAC-ARDI)	A broadband radiometer for downwelling and upwelling irradiances in the LW and the SW
Dropsondes	AVAPS dropsonde (Vaisala RD-41) system to measure temperature, humidity, and wind
Core instrument (BAHAMAS)	The aircraft and in situ data system (aircraft state, temperature, humidity, and pressure)

Table B5. P-3.

Instrument	Brief description
Cloud radar	Downward-looking PSL W-band (94 GHz) Doppler pulsed cloud radar to characterize clouds, precipitation, and the ocean surface wave state
Isotope analyzer	Picarro (L2130-i) cavity ring-down laser spectrometer measuring stable isotopologues in water vapor (including water vapor mixing ratio)
Microwave radiometer	Stepped frequency microwave radiometer ProSensing Inc., measuring in six C-band frequencies to characterize surface wind speed and rain rate
Wave radar	Wide Swath Radar Altimeter, ProSensing Inc., 80 beams to 30°, 16 GHz (Ku band) to characterize the ocean surface wave state
Infrared radiometer	Heitronics KT19.85, measuring infrared brightness temperature in the atmospheric window (9.6 to 11.5 μm)
Particle sizer	Measuring particle sizes from 0.5 to 50 μm
Cloud droplet probe	Measuring cloud droplets size from 2 to 50 μm
Particle imager	Measuring cloud and rain drops from 12.5 to 1550 μm
Rain imager	Measuring precipitation particles sizes from 0.1 to 6.2 mm
Core instrument	The aircraft and in situ data system (aircraft state, temperature, humidity, and pressure)

pling strategies, measurements, and data availability can be found in Quinn et al. (2020).

B11 BOREAL

The BOREAL UAS was operated by BOREAL SAS (Toulouse, France) and the National Center for Meteorological Research (CNRM; Toulouse, France). During EUREC^{4}A it flew nine missions totaling 32 research flight hours. Its first flight was on 26 January and its last on 9 February 2020. The BOREAL has a 4.2 m wingspan and a maximum takeoff weight of 25 kg. The BOREAL can fly up to 6 h, covering more than 600 km, with a 5 kg payload. During EUREC^{4}A, the BOREAL flew roughly 20 km radius circles between

Table B6. TO.

Instrument	Brief description
Hygrometer	Buck 1011c cooled-mirror hygrometer measuring humidity at 1 Hz
Thermometer	Non-de-iced and de-iced Rosemount probes measuring temperature at 0.7 Hz
Pyrgeometer	Eppley pyrgeometer measuring longwave irradiance 4–50 µm
Pyranometer	Eppley pyranometer measuring shortwave irradiance 0.295–2.8 µm
Infrared thermometer	Heimann IR thermometer measuring temperature at 10 Hz
Camera	Forward camera mounted in the cockpit
Turbulence probe	Best Aircraft Turbulence (BAT) probe measuring air motions and high-frequency wind (50 Hz)
Ultra-fast thermometer	Ultra-fast thermometer 2 (UFT2, developed from UFT-M) measuring temperature fluctuations with a sampling frequency of 20 kHz
Particle counter	TSI 3772 CPC measuring total ultrafine particle concentration ($D > 10$ nm)
Particle sizer	GRIMM Sky-OPC aerosol spectrometer measuring particle sizes from 0.3 to 10 µm
Particle sizer	TSI SMPS 3938 and 3775 measuring aerosol particle sizes from 25 to 1 µm
Particle counter	DMT PCASP measuring aerosol particle sizes from 0.1 to 3 µm
Particle counter	CCN-100 measuring cloud condensation nuclei as a function of supersaturation
Cloud droplet probe	DMT CDP-100 measuring cloud droplet sizes from 2 to 50 µm
Scattering spectrometer	SPEC FFSSP measuring cloud droplet sizes from 1.5 to 50 µm
Particle imager	SPEC 2D-S measuring cloud particle sizes from 10 to 1280 µm
Rain spectrometer	SPEC HVPS-3 measuring precipitation particles sizes from 150 µm to 19.2 mm
Core instrument	The aircraft and in situ data system (aircraft state, temperature, humidity, and pressure)

80 and 1000 m above sea level centered at a distance of roughly 50 km upwind of the Barbados Cloud Observatory (see Fig. 2).

B12 CU-RAAVEN

The RAAVEN was operated from Morgan Lewis Beach, Barbados, by the University of Colorado Boulder, under support from the National Oceanic and Atmospheric Administration (NOAA). During EUREC^{4}A it flew 38 missions spanning 20 d and totaling 77 flight hours. Its first flight was on 24 January and its final flight was on 15 February 2020. It typically flew two flights per day, with one occurring in the mid-morning and one in the mid-afternoon. It is an electric, fixed-wing remotely piloted aircraft system and operates with an endurance of approximately 2.5 h. Flights were primarily focused on the boundary layer, with all measurements collected below 1000 m altitude and the majority of observations occurring in the lowest 750 m of the atmosphere. Additional information on the RAAVEN, its capabilities, and the data collected during EUREC^{4}A can be found in de Boer et al. (2021).

B13 MPCKs

The Max Planck CloudKites were operated on R/V *MS-Merian* and R/V *Meteor*. Two different instrument boxes were flown with the CloudKites, namely the MPCK+ (only on R/V *MS-Merian*) and mini-MPCK (on both R/V *MS-Merian* and R/V *Meteor*). The CloudKites (except for the aerostats and winches that are produced by the Allsopp Helikites Ltd) are designed and produced by the Mobile Cloud Observatory at the Max Planck Institute for Dynamics and Self-Organization. The MPCK+ and mini-MPCK aboard R/V *MS-Merian* together flew 18 missions on 17 d (between 26 January and 18 February 2020) totaling 135 measurement flight hours. Most of the flight time was spent at 1000 m with the maximum altitude being at 1500 m. The mini-MPCK aboard the R/V *Meteor* flew nine successful missions on 9 d (between 24 January and 6 February 2020) totaling 51 measurement flight hours. Most of the flight time was spent between 200 and 1000 m.

B14 Skywalker

The Skywalker X6 UASs were operated by the National Center for Meteorological Research (CNRM; Toulouse, France),

Table B7. *Atalante.*

Instrument	Brief description
Underway data	DSHIP navigational data, base meteorology data, bathymetry: UTC time, latitude, longitude, heading, heave, pitch, roll, pressure, air temperature, water temperature dew point, relative humidity, solar broadband radiation, infrared broadband radiation, UV radiation, visibility, wind direction, wind speed, relative wind direction, and relative wind speed
Radiosondes	Vaisala RS41-SGP radiosondes measuring atmospheric profiles (during ascent and descent) of temperature, relative humidity, pressure, wind direction, and wind speed
Radiosondes	Meteomodem M10 radiosondes measuring atmospheric profiles (during ascent only) of temperature, relative humidity, wind direction and wind speed
Ceilometer	Lufft CHM 8K ceilometer measuring profiles of attenuated backscatter at 905 nm
Cloud cameras	Upward all-sky visible images and upward 30° field-of-view thermal images, both at 0.1 Hz
Sun photometer	MICROTOPS sun photometer capturing at sun views the solar attenuation at 380, 440, 670, 870, and 940 nm to derive column properties of aerosol optical depth (AOD) at these wavelengths and the atmospheric water vapor content
Atmospheric mast	A meteorological station WXT-500, a 3D wind anemometer Gill HS-50, a CNR4 radiometer for direct and indirect radiation, an inertial station to filter the ship motion, a refractometer for humidity, a LICOR LI-7500DS for fast CO_2 and humidity measurements, fast measurements of wind, temperature, humidity, and pressure, two GPS antennas, and a motion pack
Isotope analyzer	Picarro (L2140-i7) cavity ring-down laser spectrometer measuring stable isotopologues in water vapor (including water vapor mixing ratio)
Isotope sampler	Sampling system for measuring stable isotopologues in rain and seawater
Pyranometer	SPN1 Delta-T SNC radiometer measuring global and diffuse radiation
Hypersp. radiometer	ROX JBC hyperspectral radiometer measuring global, reflected, and diffuse spectral radiation from 350 to 950 nm
GNSS	Global Navigational Satellite System (GNSS) antennas and receivers for measuring underway columnar water vapor content
Aethalometer	Aethalometer AE33 Magee Scientific measuring aerosol attenuation at seven wavelengths (370, 470, 520, 590, 660, 880, and 950 nm) and used to infer black carbon concentrations
Particle sizer	NanoScan TSI Inc. measuring particle number concentrations from 10 to 400 nm
Particle counter	GRIMM 1.107 optical particle counter measuring number concentrations from 0.25 to 32 μm
Volume sampler	Echo PUF TCR Tecora measuring particle mass concentrations and chemical composition
Thermosalinograph	SBE-21 and SBE38 thermosalinographs measuring near-surface seawater temperature, conductivity, and fluorescence (to infer salinity and chlorophyll)
pCO_2	LICOR LI-7000 measuring system for pCO_2 and fCO_2
CTD casts	SBE-911 Plus CTD for conductivity, temperature, and pressure measurements, a SBE-43 dissolved-oxygen sensor, a Chelsea AquaTracka III fluorimeter for in situ detection of chlorophyll a, a WET Labs CSTAR transmissometer for underwater measurements of beam transmittance, a Tritech PA500 altimeter, and a Biospherical Instruments QCP2350 cosine-corrected irradiance collector for measuring photosynthetically active radiation (PAR).
Moving vessel profiler	A MVP30-300 AML Oceanographic measuring water column temperature, salinity, pressure, and high-frequency vertical profiles of seawater temperature and salinity within the upper ocean (0 to 200 m)

https://doi.org/10.5194/essd-13-4067-2021

Earth Syst. Sci. Data, 13, 4067–4119, 2021

Table B7. Continued.

Instrument	Brief description
uCTD	Teledyne underway CTD is a profiler device measuring vertical profiles within the upper ocean (0–400 m) of salinity (through conductivity), temperature (through a thermistor), and depth (through pressure), deployed over a moving vessel; it has the convenience of an expendable device like the XBT, but it is recoverable and reusable
Microstructure sonde	Rockland Scientific VMP-500 measuring vertical profiles of microstructure and dissipation-scale turbulence in the upper 300 m of the ocean
Acoustic Doppler current profiler	Teledyne RDI 38 and 150 kHz acoustic Doppler current profilers measuring subsurface (30 to 1000 m and 30 to 150 m, respectively) water velocity
Acoustic Doppler current profiler	Teledyne RDI 300 kHz duo acoustic Doppler current profiler measuring full water column water velocity
XBTs	Lockheed Martin Sippican XBT-T7 measuring vertical profiles of seawater temperature within the upper ocean (0 to 800 m).
XCTDs	Lockheed Martin Sippican XCTD-2 measuring vertical profiles of seawater temperature and conductivity (salinity) within 0 to 1000 m
Argo floats	ARVOR-type Argo floats constructed through a cooperation between the Centro di Taratura Oceanografico and NKE Instrumentation measuring vertical profiles of seawater temperature, salinity, and dissolved oxygen within the upper ocean (initially 0 to 1000 m, parking depth 200 dbar, daily; after 0 to 2000 m, parking depth 1000 dbar, every 10 d)

the French Civil Aviation University (ENAC; Toulouse, France), and the Laboratory for Analysis and Architecture of Systems (LAAS; Toulouse, France) as part of the NEPHAE-LAE project (ANR-17-CE01-0003). During EUREC^{4}A, the team flew more than 50 flights over the ocean up to 15 km off the eastern coast of Barbados. The first flight was on 25 January and the last was on 9 February 2020. The Skywalker has a 1.5 m wingspan and a maximum takeoff weight of 2.5 kg. The Skywalker flew up to 1 h and utilized sensor feedback to map an individual cloud autonomously and adaptively.

B15   Caravela

The AutoNaut (Caravela) was operated by the University of East Anglia (UEA). Caravela is an unmanned surface vehicle with continuously sampling meteorological and oceanographic sensors and can also be used to tow and deploy an underwater glider. During EUREC^{4}A it was deployed on 22 January from the coastguard station on Barbados towing underwater glider SG579, which was released on 28 January. Caravela continued to its study location centered at 14.2° N, 57.3° W and spent 11 d repeating a butterfly pattern around a square with 10 km sides, before returning to Barbados for recovery on 24 February.

B16   Underwater electric gliders

Three underwater gliders were operated by UEA. SG579 was deployed from Caravela on 28 January and completed 76 dives to 1000 m along the transect to the gliders' study lo-

cation, followed by 219 dives to 250 m while traversing the same butterfly pattern as Caravela. It was recovered onto R/V *Meteor* on 16 February. SG637 was deployed from R/V *Meteor* on 23 January, completed 155 dives to 750 m around the same "butterfly", all with ADCP data, and was also recovered onto R/V *Meteor* on 16 February. SG620 was deployed from the *Meteor* on 23 January and completed 131 dives to 750 min virtual mooring mode at the center of the butterfly, before being recovered on 5 February onto R/V *Meteor*.

Three Teledyne Slocum G2 underwater electric gliders were operated by GEOMAR. All three surveyed down to 1000 m depth. IFM03 and IFM12 were deployed from the R/V *MS-Merian* on 24 January to survey the edge of a mesoscale eddy. IFM03 was recovered by the R/V *Meteor* on 3 February, and IFM12 was recovered with R/V *MS-Merian* on 17 February 2020 after a complete survey. IFM09 was operated within the EUREC^{4}A-Circle as a virtual mooring mission from 20 January and recovered by R/V *MS-Merian* on 9 February 2020.

One SeaExplorer X2 underwater glider (Kraken) was deployed and recovered from the R/V *Atalante* and operated by DT INSU CNRS in connection with the ship chief scientist. Kraken was deployed on 25 January at 10° 08′ 45″ N, 57° 29′ 37″ W and was recovered on 13 February 2020 at 10° 19′ 24″ N, 57° 53′ 30″ W. It accomplished 472 profiles down to 700 m across two different mesoscale eddies, both anticyclonic: a North Brazil Current ring limited to the upper 150 m of depth and a thicker subsurface (200–600 m) eddy.

Table B8. *MS-Merian.*

Instrument	Brief description
CTD casts	Sea-Bird SBE-911 CTD mounted on a rosette system, operated up to full water depth, measuring vertical profiles of seawater temperature, salinity, fluorescence, oxygen, and PAR
Rosette bottle sampler	Samples used for ocean-microbiology observations, including biogeochemical parameters (e.g., nutrients, chlorophyll *a*, particulate organic carbon and nitrogen, trace greenhouse gases), biogeochemical process rates (e.g., primary production), and molecular analyses (e.g., microbial community structure)
Cloud cameras	Upward all-sky visible images and upward 30° field-of-view thermal images, both at 0.1 Hz
Underwater Vision Profiler	The Underwater Vision Profiler UVP5 is an underwater camera system mounted on the CTD rosette that can take images of particles and plankton down to 6000 m water depth
UV spectral sensor	The TriOS OPUS spectral sensor was mounted on the CTD rosette to acquire full-depth profiles of nitrate and nitrite
Acoustic Doppler current profiler	Teledyne RDI 300 kHz lowered ADCP mounted on the CTD rosette to survey full-depth ocean currents and acoustic backscatter
Acoustic Doppler current profiler	Teledyne RDI ADCP 38 kHz and 75 kHz were mounted in the hull of the ship (75 kHz) and in the ship moon pool (38 kHz) to provide water currents and backscatter information from close to the surface to more than 1 000 m depth; surveyed in an underway mode
Thermosalinograph	Sea-Bird SBE-45/SBE-38 measuring temperature and salinity underway from about 6.5 m water depth
Microstructure sonde	Sea & Sun Technology microstructure probe MSS 90 measuring the micro-scale temperature, pressure, conductivity, and shear to determine the micro-scale water stratification and the strength of small-scale turbulence in the water column
FerryBox system	OceanPack FerryBox underway system that acquires $p\mathrm{CO}_2$ data from 6.5 m water depth
Radiosondes	Vaisala RS41-SGP radiosondes measuring atmospheric profiles (during ascent and descent) of temperature, relative humidity, pressure, wind direction, and wind speed
Moving vessel profiler	An AML Oceanographic MVP30-350 measuring vertical profiles of temperature, salinity, pressure, and fluorescence in the upper ocean, operated as underway system at selected segments
uCTD	Teledyne Oceanscience underway CTD measuring vertical profiles of temperature, pressure, and salinity in the upper ocean, operated as underway system at selected cruise segments
Wave radar	A 9.4 GHz X-band wave radar measuring both phase and intensity of the radar backscatter and Doppler speed (sampled up to a maximum range of about 3 km around the ship), to determine surface currents, wind field, and surface signatures of internal waves
Sun photometer	MICROTOPS sun photometer capturing at sun views the solar attenuation at 380, 440, 670, 870, and 940 nm to derive column properties of aerosol optical depth (AOD) at these wavelengths and the atmospheric water vapor content
Weather sensors	German Weather Service (DWD) automatic weather station measuring underway wind speed, wind direction, temperature (air, ocean), humidity, and barometric pressure
GNSS	Global Navigational Satellite System (GNSS) antennas and receivers for measuring underway columnar water vapor content
Particle sizer	SMPS (TSI 3080) measuring aerosol/CN size distribution (10 to 420 nm)
Micro Rain Radar	A 24 GHz meteorological radar profiler for Doppler spectra of hydrometeors and multiple parameters related to rain
Cloud radar	RPG FMCW94 cloud radar to characterize the atmospheric state and clouds (including precipitation and turbulent structure of the atmospheric boundary layer) through reflectivity, Doppler velocity, spectral width, and skewness

Table B8. Continued.

Instrument	Brief description
Raman lidar (ARTHUS)	University of Hohenheim Raman lidar at 355 nm providing underway vertical profiles of temperature, water vapor mixing ratio, aerosol particle backscatter, and extinction coefficients at up to 10 Hz and 7.5 m as well as range resolution
Wind lidar	Doppler lidar (1 Hz temporal and 30 m range resolution) for the profiling of vertical wind and particle backscatter coefficient as well as boundary layer depth and cloud-base height
Wind lidar	Scanning Doppler lidar operated in the six-beam staring mode for the profiling of horizontal wind, TKE, and momentum flux; horizontal wind profiles are delivered with 1 min as well as the TKE and momentum flux profiles with 30 to 60 min resolution
Ocean microbiology	Measurements in the upper water column of biogeochemical parameters (e.g., nutrients, chlorophyll a, particulate organic carbon and nitrogen, trace greenhouse gases), biogeochemical process rates (e.g., primary production), and molecular analyses (e.g., microbial community structure)
Underway data	Data acquired at high temporal resolution along the ship track: latitude, longitude, motion, course/heading (multiple), water depth, solar global radiation, infrared radiation, PAR radiation, and rain (vertical/lateral)

B17 Saildrones

Continuous measurements of air–sea interaction by five uncrewed surface vehicle (USV) Saildrones were led by Farallon Institute, NOAA/PMEL, and CICOES/University of Washington during EUREC^{4}A and ATOMIC from 12 January to 3 March 2020. Three NASA funded Saildrones (SD1026, SD1060, SD1061) and one NOAA-funded Saildrone (SD1063) were dedicated to the ocean eddy corridor southeast of Barbados, where large North Brazil Current rings migrate northwestward. The NOAA-funded Saildrone SD1064 was dedicated to the trade wind alley between NTAS buoy and the HALO flight circle. The two NOAA-funded Saildrones continued their observation after the EUREC^{4}A/ATOMIC intensive observation period until 15 July 2020.

B18 SWIFTs and Wave Gliders

A total of six SWIFT (Surface Wave Instrument Floats with Tracking) drifting platforms were deployed from the R/V *Ron Brown* during EUREC^{4}A. There was an initial deployment for 2 weeks in January 2020 and a second deployment for another 2 weeks in February 2020. SWIFTs are produced and operated by the Applied Physics Laboratory at the University of Washington. Two of the SWIFTs were version 3 models, as described in Thomson (2012), and four of the SWIFTs were version 4 models, as described in Thomson et al. (2019). SWIFTs collect data in a wave following reference frame, with burst sampling and statistical products available hourly.

Two Wave Glider ASVs (autonomous surface vehicles), designated WG245 and WG247, operated from the R/V *Ron Brown* during EUREC^{4}A. The missions each spanned 4 weeks from January to February 2020. The Wave Gliders are built by Liquid Robotics, Inc, with additional sensors integrated by the Applied Physics Laboratory at the University of Washington for air–sea flux calculations (Thomson and Girton, 2017).

B19 Surface drifters, OCARINA and PICCOLO

Ten SVP-BSW (barometer–salinity–wind) drifters from Pacific Gyre were deployed from R/V *Atalante* from 23 January to 4 February 2020. Each drifter had temperature and salinity measurements at three levels (0.50, 5, and 10 m) as well as barometric sea level pressure and wind. Five SC40 SVP-BRST drifters (from EUMETSAT grant TRUSTED to Météo-France/CLS) manufactured by NKE were deployed for three short periods of time from the R/V *Atalante* before being finally released at sea between 10 and 14 February 2020. Each drifter provided high-precision measurements of temperature at 20 cm depth and of barometric sea level pressure. Two SC40 SVP-BSC drifters (from Météo-France/LOCEAN with CNES/SMOS support) manufactured by NKE were deployed for three short periods of time from the R/V *Atalante* before being released at sea between 10 and 14 February 2020. Each drifter measured temperature and salinity at 20 cm depth and barometric sea level pressure. Two Surpact wave riders manufactured by SMRU (University of St Andrews) and LOCEAN (with CNES/SMOS support) were deployed for short times from the R/V *Atalante* before being released at sea between 10 and 14 February 2020. These drifters do not have a drogue to follow the currents at 15 m and thus are deployed tethered to another drifter. Each float measured temperature and salinity at 5 cm depth, as well as vertical acceleration and thus wave spectra. Moreover, the noise recorded by a microphone under a cupola was spectrally analyzed to estimate the noise

Table B9. *Meteor.*

Instrument	Brief description
Underway data	Data acquired along the ship track: time, position (latitude, longitude), motion (heave, pitch, roll), atmospheric state (pressure, air temperature, water temperature, dew point, relative humidity), wind (wind direction, wind speed, relative wind direction, relative wind speed), downward broadband solar radiation (200–3600 nm), downward broadband infrared radiation (4.5–42 µm), ocean currents at different depth (ADCP), and surface water sea salt content and water temperature (thermosalinograph)
Raman lidar	Lidar providing vertical profiles of attenuated backscatter at 355, 532, and 1064 nm, volume depolarization ratio at 532 nm, particle linear depolarization ratio, and vertical profiles of water vapor mixing ratio
Cloud radar	94 GHz cloud radar operating on a balanced platform measuring radar reflectivity , linear depolarization ratio, Doppler velocity, and spectral width
Microwave radiometer	HATPRO microwave radiometer measuring brightness temperatures in K and V Bands
Solar spectrometer	Measuring downward spectral solar irradiance between 300 and 2200 nm for droplet effective radius and liquid water path retrievals
Ceilometer	Jenoptik system measuring vertical profiles of attenuated backscatter at 1064 nm to infer cloud base as a function of altitude and aerosol
Cloud cameras	Upward all-sky visible images and upward 30° field-of-view thermal images, both at 0.1 Hz
Sun photometer	MICROTOPS sun photometer capturing at sun views the solar attenuation at 380, 440, 670, 870, and 940 nm to derive column properties of aerosol optical depth (AOD) at these wavelengths and the atmospheric water vapor content
Solar spectrometer	MAX-DOAS (Multi-AXis Differential Optical Absorption Spectroscopy) measuring scattered sky solar radiances at different elevation angles to infer NO_2, SO_2, SO_2, H_2O, and oxygen dimer (near the surface, vertical profiles, and column data)
GNSS	Global Navigational Satellite System (GNSS) antennas and receivers for measuring underway columnar water vapor content
Particle sizer	WRAS (GRIMM, EDM 180) measuring aerosol/CN size distribution (0.25 to 32 µm)
Photoacoustic extinctiometer	PAX photoacoustic nephelometer measuring the scattering of aerosol (size information) and the photoacoustic absorption (black carbon concentration)
Air sampler	Locomotive air sampler measuring concentrations of larger (PM10) aerosol particles
Wind lidar	WINDCUBE WLS70 wind lidar measuring vertical wind profiles for the 100–2000 m range
Wind lidar	WINDCUBE V2 wind lidar measuring vertical wind profiles for the 40–250 m range
Eddy covariance	A 4 m outrigger in front of the *Meteor* and one high up in the main mast close to the operational wind measurements providing high-resolution (20 Hz) measurements of vertical wind speed and gas concentrations to derive surface momentum, enthalpy, and CO_2 fluxes
Isotope analyzer	Picarro (L2140-i7) cavity ring-down laser spectrometer measuring stable isotopologues in water vapor (including water vapor mixing ratio)
Isotope sampler	Sampling system for measuring stable isotopologues in rain and seawater
Rain collector	Palmex rain collector avoiding re-evaporation used to sample precipitation
Radiosondes	Vaisala RS41-SGP radiosondes measuring atmospheric profiles (during ascent and descent) of temperature, relative humidity, pressure, wind direction, and wind speed
UASs	Light ship-based (quadcopter) UASs were operated (during stations only) for measuring temperature and wind speed profiles in the lower atmosphere (up to 300 m) and temperature profiles within the upper 20 m of the ocean

Table B9. Continued.

Instrument	Brief description
CTD casts	Vertical profiles, within the upper 800 m of the ocean, of temperature, salinity, dissolved oxygen, and fluorescence
Ocean microbiology	Measurements in the upper water column of biogeochemical parameters (e.g., nutrients, chlorophyll a, particulate organic carbon and nitrogen, trace greenhouse gases), biogeochemical process rates (e.g., primary production), and molecular analyses (e.g., microbial community structure)

of the wind/waves and rainfall. Five barometer–temperature drifters from Pacific Gyre were deployed from R/V *MS-Merian* from 21 January to 4 February 2020. Each drifter measured temperature at 20 cm depth and barometric sea level pressure. Each drifter had a 6 m long drogue centered at a depth of 15 m. The drifters used Iridium SBD telemetry and a 50-channel GPS system (including WAAS correction), and data were transmitted every 30 min.

The R/V *Atalante* also deployed two drifting platform prototypes, OCARINA (Ocean Coupled to Atmosphere, Research at the Interface with a Novel Autonomous platform) and PICCOLO (Profiling Instrument to Check if the wind Curvature is Only Logarithmic on the Ocean), to measure air–sea fluxes (momentum, sensible heat, latent heat, radiative shortwave and longwave up and down) very close to the sea surface. The platforms were deployed on 25 January 2020 from 15:00 to 21:00 UTC (start position 10.11° N, 57.50° W; end position 10.15° N, 57.45° W), on 3 February from 10:00 to 21:00 UTC (start position 6.83° N, 54.14° W; end position 6.83° N, 54.34° W), on 10 February from 10:00 to 19:00 UTC (start position 10.38° N, 59.13° W; end position 10.53° N, 59.23° W), and on 17 February from 09:00 to 18:00 UTC (start position 13.13° N, 59.75° W; end position 13.10° N, 59.82° W).

Table B10. *Ron Brown.*

Instrument	Brief description
Anemometer	Metek uSonic-3 anemometer measuring wind vector, stress, and heat flux (bow mast)
Rain gauge	Optical precipitation sensor ORG-815 DA measuring the rain rate at 1 Hz (bow mast)
Humidity sensor	LICOR 7500 gas analyzer measuring water vapor density (bow mast)
Weather sensors	Vaisala HMT335 transmitter measuring air temperature and humidity, and Vaisala PTB220 barometer to measure atmospheric pressure (bow mast)
Pyranometer	Eppley PSP measuring shortwave 295–2800 nm irradiance (bow mast)
Pyrgeometer	Eppley PIR measuring downward longwave irradiance 4–50 µm (bow mast)
Inertial system	Mast and ship motions (bow mast)
Ceilometer	Vaisala CL31 ceilometer measuring vertical profiles of backscatter from refractive index gradients, cloud-base height, and cloud fraction (O3 deck)
Disdrometer	Two Parsivel optical rain gauges (650 and 780 nm) measuring the size, fall speed and precipitation intensity, radar reflectivity, particle number, and cumulated precipitation for rain droplets with sizes between 0.2 and 8 mm (O3 deck)
Camera	StarDot NetCam XL camera pointed to starboard (field of view of 15 m, image captured every 4 s, O3 deck)
Doppler lidar	For measuring atmospheric velocities and backscatter to infer cloud-base height and boundary layer turbulence (O2 deck)
Cloud radar	Vertically pointing W-band (95 GHz) Doppler cloud radar measuring vertical profiles of non-precipitating and lightly precipitating clouds up to 4.2 km with 30 m resolution (O2 deck)
Radon detector	Dual-flow loop two-filter radon (^{222}Rn) detector (O3 deck)
Weather sensors	Vaisala WXT-536 weather sensors measuring air temperature, humidity, pressure, rainfall, and wind (O2 deck)
Isotope analyzer	Picarro (L2130-i) cavity ring-down laser spectrometer measuring stable isotopologues in water vapor (including water vapor mixing ratio)
Isotope sampler	Sampling system for measuring stable isotopologues in rain and seawater
Radiosondes	Vaisala RS41-SGP radiosondes measuring atmospheric profiles (during ascent and descent) of temperature, relative humidity, pressure, wind direction, and wind speed (every 4 h, main deck)
Ozone analyzer	Thermo Environmental Model 49C measuring ozone concentration (aerosol inlet)
In situ aerosol instrumentation	Collection with multi-jet cascade impactors and analysis by ion chromatography, thermal-optical, gravimetric, and XRF analysis to measure size-segregated concentrations of Cl^-, NO_3^-, SO_4^-, methanesulfonate (MSA), Na^+, NH_4^+, K^+, Mg_2^+, Ca_2^+, organic carbon, elemental carbon, and trace elements (aerosol inlet)
Particle sizer	DMPS and TSI 3321APS measuring number and size distributions 0.02 to 10 µm (aerosol inlet)
Particle sizer	TSI 3025A, 3760A, and 3010 measuring number concentrations > 3, 13, and 13 nm (aerosol inlet)
Nephelometer	TSI 3563 nephelometer measuring aerosol light scattering and backscattering at 60 % relative humidity by splitting light into 450, 550, and 700 nm wavelengths (aerosol inlet)
Nephelometer	TSI 3563 nephelometer measuring aerosol light scattering and backscattering as a function of relative humidity by splitting light into 450, 550, and 700 nm wavelengths at dry and 80 % relative humidities (aerosol inlet)
Photometer	Radiance Research particle soot absorption photometer (PSAP) measuring light absorption at 467, 530, and 660 nm (aerosol inlet)

Table B10. Continued.

Instrument	Brief description
Particle counter	DMT cloud condensation nuclei counter (CCNC) measuring the number of particles which can activate cloud droplets at a specific supersaturation (0.1 % to 0.6 % supersaturation)
Sun photometer	MICROTOPS sun photometer capturing at sun views the solar attenuation at 380, 440, 670, 870, and 940 nm to derive column properties of aerosol optical depth (AOD) at these wavelengths and the atmospheric water vapor content
Spectrometer	Marine Atmospheric Emitted Radiance Interferometer (M-AERI) spectrometer to infer skin sea surface temperature (O2 deck)
Radiometer	Remote Ocean Surface Radiometer (ROSR) measuring sea surface skin temperature (O2 deck)
Thermistor (sea snake)	Floating YSI 46040 Thermistor (deployed off port side with outrigger) measuring near-skin sea surface temperature
Altimeter	Riegl 1D laser altimeter measuring wave height (bow mast)
CTD casts	Sea-Bird 9+ CTD at station measuring conductivity (salinity), temperature, depth (pressure), PAR, fluorescence, and dissolved oxygen (deployed off starboard side, main deck)
Thermosalinograph	Sea-Bird SBE-45 and SBE-38 thermosalinographs measuring seawater temperature and conductivity near the surface and 5 m below the surface
CTD/uCTD	ADCP measuring ocean currents to 600–750 nm using an RBRconcerto underway CTD and a Tuna Brute winch (uCTD) to measure conductivity (salinity) and temperature and depth (pressure) in the upper 60 to 130 m (deployed off starboard aft quarter)

Table B11. BOREAL.

Instrument	Brief description
Particle counter	CPC measuring aerosol concentrations ($D > 11$ nm) at 1 Hz
Particle counter	Optical particle counter measuring aerosol size distribution ($0.3\,\mu m < D < 3$ nm) at 1 Hz
Infrared thermometer	Measuring infrared brightness temperatures to infer SST
Turbulence probe	Multihole probe measuring vertical and horizontal winds at 30 Hz to characterize turbulence and fluxes
Radar altimeter	To characterize the sea state, including wave height, speed, and direction; 1 Hz
Weather sensors	Measuring temperature, pressure, and relative humidity
Solar radiometer	Solar irradiance and broadband solar flux (400 to 1100 nm); 1 Hz
Camera	High-resolution visible camera looking forward and down to characterize clouds and the sea state

Earth Syst. Sci. Data, 13, 4067–4119, 2021

https://doi.org/10.5194/essd-13-4067-2021

Table B12. CU-RAAVEN.

Instrument	Brief description
Weather sensors	Vaisala RSS-421 PTH sensors (two body-mounted RSS-421s, similar to sensors in RS41 radiosondes and RD41 dropsondes) measuring pressure, temperature, and relative humidity
Multihole probe	Black Swift Technologies multihole pressure probe measuring static and dynamic pressure, airspeed, angle of attack, sideslip, attitude and acceleration, temperature, and humidity, primarily for wind estimation
Inertial system	VectorNav VN-300 INS to measure aircraft position, attitude, acceleration, inertial velocities, static pressure, and inertial motion unit, with integrated GPS
Infrared thermometer	Melexis IR thermometers measuring surface and sky brightness temperatures in a narrow field of view for sensing surface temperature and cloud presence
Turbulence probe	Custom fine-wire array (three-wire array with two cold wires and one hot wire) for fast temperature, humidity, and velocity sensing

Table B13. MPCK+.

Instrument	Brief description
Weather sensors	Aosong relative humidity (2 % RH accuracy) and temperature (0.1–1 K accuracy) sensor (0.2 Hz)
Anemometer	1D static tube with PT100 measuring wind speed and temperature at 100 Hz, wind speed range 3 to 20 ms^{-1} with < 5 % accuracy, temperature −35…55 °C with accuracy of ±0.3 K
Anemometer	Five-hole static tube; 100 Hz, 4…15 ms−1, < 5 % wind speed accuracy, 1° wind direction accuracy to measure 3D wind velocity
Particle image velocimetry	PIV at 15 Hz with a pulsed 532 nm laser and a high-speed camera, max. probing. vol. 150 mm × 100 mm × 5 mm, to characterize droplet 2D velocity and spatial distribution
Holography	In-line holography at 75 Hz with a pulsed 355 nm laser and 25 Mpx camera, max. probing. vol. 15 mm × 15 mm × 250 mm, to characterize 3D droplet size and spatial distribution
Cloud droplet probe	SPEC Fast CDP using forward scattering to measure droplet size and number concentration of 2 to 50 μm particles up to 2000 cm^{-3}

Table B14. Mini-MPCK.

Instrument	Brief description
Weather sensors	Aosong relative humidity (2 % RH accuracy) and temperature (0.1–1 K accuracy) sensor (0.2 Hz).
Anemometer	1D static tube with PT100 measuring wind speed and temperature at 100 Hz, wind speed range 3–20 m s^{-1} with < 5 % accuracy, and temperature −35…55 °C with accuracy of ±0.3 K
Anemometer	Metek uSonic-3 Class A ultrasonic anemometers operating at 30 Hz, 0–40 m s^{-1} with minimal flow shadowing from of the arms, and 1° wind direction accuracy
Cloud droplet probe	DMT CDP-2, a forward-scattering optical spectrometer to determine size and number concentration of 2 to 50 μm particles
Weather sensors	Vaisala HMP7 heated humidity and temperature probe; response time ∼ 15 s, ±0.8 % RH accuracy, ±0.1 K temperature accuracy
Weather sensors	Bosch BMP388 sensor measuring pressure and temperature (±50 Pa absolute pressure accuracy, ±0.3 K temperature accuracy)
Hot wire	Dantec mini-hot wire measuring air velocity fluctuations at 8 kHz
Ultra-fast thermometer	Ultra-fast thermometer M (UFT-M, provided by University of Warsaw) measuring temperature fluctuations with a sampling frequency of 8 kHz

Table B15. Skywalker.

Instrument	Brief description
Cloud sensor	Cloud extinction measured at three wavelengths (1 Hz)
Cloud active mapping system	Adaptive sampling and real-time mapping of clouds
Weather sensors	Measurements of temperature and relative humidity
Camera	High-resolution visible camera looking forward and down to characterize clouds and the sea state
Inertial system	Paparazzi Apogee autopilot providing UAS flight parameters (latitude, longitude, altitude, pitch, roll, yaw, horizontal wind speed)

Table B16. Caravela.

Instrument	Brief description
Pyranometer	CS301 Apogee SP-110-SS pyranometer measuring downwelling shortwave radiation (360–1120 nm)
Pyrgeometer	Apogee SL-510 pyrgeometer measuring downwelling longwave radiation (5–30 μm)
Weather sensors	Airmar 120WX weather station measuring wind velocity, air temperature (measurement height 1.5 m)
Weather sensors	Rotronic HC2A-S3, Rotronic MP402H 082000, and Rotronic AC1003 measuring air temperature and humidity (measurement height 1 m)
Ocean state	Valeport miniCTD measuring sea surface temperature and conductivity (mounted through Caravela's hull, measurement depth 0.2 m)
Acoustic Doppler current profiler	Nortek Signature1000 1 MHz acoustic Doppler current profiler (ADCP) with a five-beam setup for estimating velocity shear and biomass in the water column, range 30 m

Table B17. Humpback (SG579).

Instrument	Brief description
CT sail	Sea-Bird unpumped CT sail measuring temperature and conductivity
PAR sensor	Biospherical Instruments QSP2150 measuring photosynthetically active radiation
Fluorometer	WET Labs ECO Triplet measuring chlorophyll fluorescence, chromophoric dissolved organic matter (CDOM) fluorescence, and optical backscatter at 650 nm

Table B18. Omura (SG637).

Instrument	Brief description
CT sail	Sea-Bird unpumped CT sail measuring temperature and conductivity
Acoustic Doppler current profiler	Nortek Signature1000 1 MHz acoustic Doppler current profiler (ADCP) measuring vertical shear of horizontal current velocity

Table B19. Melonhead (SG620).

Instrument	Brief description
CT sail	Sea-Bird unpumped CT sail measuring temperature and conductivity
Microstructure sonde	Rockland Scientific MicroPods microstructure system measuring shear and temperature and thus ocean turbulence

Table B20. IFM03.

Instrument	Brief description
CTD sensor	Measuring temperature and salinity
Oxygen sensor	Optode measuring dissolved oxygen
Fluorometer	WET Labs ECO puck measuring chlorophyll fluorescence and turbidity
Microstructure sonde	Rockland Scientific MicroRider turbulence sensor

Table B21. IFM09.

Instrument	Brief description
CTD sensor	Measuring temperature and salinity
Oxygen sensor	Optode measuring dissolved oxygen
Fluorometer	WET Labs ECO puck measuring chlorophyll fluorescence and turbidity
Microstructure sonde	Rockland Scientific MicroRider turbulence sensor

Table B22. IFM12.

Instrument	Brief description
CTD sensor	Measuring temperature and salinity
Oxygen sensor	Optode measuring dissolved oxygen
Fluorometer	WET Labs ECO puck measuring chlorophyll fluorescence and turbidity
Nutrient analyzer	Sea-Bird Submersible UV Nitrate Analyzer (SUNA)
Optical sensor	Measuring dissolved organic matter (CDOM)

Table B23. Kraken.

Instrument	Brief description
CTD sensor	Sea-Bird CTD (GPCTD) measuring temperature, salinity, and pressure
Oxygen sensor	Optode measuring dissolved oxygen
Fluorometer and backscatter sensor	WET Labs ECO puck BB2FLVMT measuring chlorophyll a fluorescence and turbidity
Optical sensor	WET Labs ECO puck measuring dissolved organic matter (CDOM)

Table B24. Saildrones.

Instrument	Brief description
Anemometer	WindMaster Gill 1590-PK-020 sonic anemometer 10 Hz at 5.2 m above water line, measuring wind speed and direction
Weather sensors	Rotronic HygroClip 2 measuring air temperature and relative humidity at 1 Hz, 1 min measurements every 5 min at 2.3 m above water line
Pyrometer	Heitronics CT 15.10 infrared pyrometer to measure skin SST (experimental)
Cameras	Four visible cameras looking sideways, upward, and downward
PAR sensor	LICOR LI-192SA sensor measuring photosynthetically active radiation at 2.6 m above water line
CT sensor	SBE-37-SMP-ODO MicroCAT measuring seawater temperature, salinity, conductivity, and dissolved oxygen (pumped CTD at 0.5 m depth)
CT sensor	RBR Ltd C.T.ODO.chl-a logger measuring seawater temperature, salinity, conductivity, dissolved oxygen, and chlorophyll *a* (experimental); inductive CTD at 0.53 m depth
Fluorometer	WET Labs ECO-FL-S G4 and Turner Cyclops measuring chlorophyll *a* (experimental) at 0.5 m depth
Barometer	Vaisala PTB210 measuring barometric pressure at 0.2 m above water line
Inertial system	VectorNav VN300 Dual GPS-aided inertial measurement unit deriving estimates of significant wave height and dominant period from wave spectrum
Thermistors	Sea-Bird SBE-57s thermistors of seawater temperature (on keel at 0.3, 0.6, 0.9, 1.2, 1.4, and 1.7 m depths)
Acoustic Doppler current profiler	Teledyne Workhorse 300 kHz ADCP measuring ocean current profiles between 6 and 100 m depths
Pyranometer	SPN1 Delta-T Sunshine Pyranometer measuring total and diffuse solar radiation (equipped on NOAA-funded Saildrones, 2.8 m above water line, sampling at 5 Hz for tilt correction, Zhang et al., 2019)
Pyrgeometer	Eppley Precision Infrared Radiometer (PIR) measuring downward longwave radiation (equipped on NOAA-funded Saildrones, 0.8 m above water line)

Table B25. SWIFTs.

Instrument	Brief description
Inertial system	SBG Ellipse GPS measuring drift speed from 5 Hz positions and velocities
Inertial system	SBG Ellipse IMU measuring surface waves from 5 Hz displacements (processed for hourly wave spectral parameters)
Weather sensors	Vaisala WXT-536 measuring air temperature, humidity, pressure, rainfall, and wind at 1 m
Weather sensors	Airmar PB200 measuring wind speed and direction, air temperature, and air pressure at 1 m above surface
CT sensors	Aanderaa CT sensor measuring surface conductivity and temperature to infer ocean salinity and temperature at 0.5 m below surface
Acoustic Doppler current profiler	Nortek Aquadopp 2 MHz ADCP used in pulse-coherent (HR) mode to measure ocean turbulence and current profiles with high resolution
Acoustic Doppler current profiler	Nortek Signature 1 MHz ADCP used in pulse-coherent (HR) mode to measure ocean turbulence and current profiles with high resolution
Camera	Low-resolution sky cameras providing pictures every 4 s

Earth Syst. Sci. Data, 13, 4067–4119, 2021

https://doi.org/10.5194/essd-13-4067-2021

Table B26. Wave Gliders.

Instrument	Brief description
Inertial system	MicroStrain GPS measuring vehicle speed from 5 Hz positions and velocities
Inertial system	MicroStrain IMU measuring surface waves from 5 Hz displacements (processed for hourly wave spectral parameters, Thomson et al., 2018)
Weather sensors	Vaisala WXT-536 measuring air temperature, humidity, pressure, rainfall, and wind at 1 m
Weather sensors	Airmar PB200 measuring wind speed and direction, air temperature, and air pressure at 1 m above surface
CT sensors	Aanderaa CT sensor measuring surface conductivity and temperature to infer ocean salinity and temperature at 0.3 m below surface
Glider payload	Sea-Bird GPCTD measuring conductivity, temperature, and depth to infer ocean salinity and temperature at 8 m below surface
Acoustic Doppler current profiler	300 kHz ADCP measuring ocean current profiles from 0 to 120 m depth

Table B27. SVP-BSW drifters.

Instrument	Brief description
Thermistor	30 K thermistor measuring seawater temperature at a depth of 20 cm
CT sensors	Sea-Bird SBE-37-SI measuring seawater temperature and conductivity (salinity) at a depth of 20 cm
CT sensors	Sea-Bird SBE-37-IM measuring seawater conductivity and temperature to infer ocean temperature and salinity at depths of 5 and 10 m
Pressure sensor	Honeywell integrated pressure transducer (IPT) measuring atmospheric pressure at a height of 50 cm
Tilt compensated compass	PNI TCM-2.5 measuring wind direction at a height of 50 cm
Anemometer	Gill WindSonic two-axis ultrasonic anemometer measuring wind speed at a height of 50 cm
GPS	To monitor the current at sea surface

Table B28. SVP-BRST drifters.

Instrument	Brief description
HRSST thermistor	Digital high-resolution thermistor measuring seawater temperature at a depth of 15 cm
Pressure sensor	Vaisala PTB110 barometer measuring atmospheric pressure at a height of 50 cm
GPS	To monitor the current at sea surface

Table B29. SVP-BSC drifters.

Instrument	Brief description
CT sensors	Sea-Bird SBE-37-SI measuring seawater temperature and conductivity (salinity) at a depth of 15 cm
Pressure sensor	Vaisala PTB110 barometer measuring atmospheric pressure at a height of 50 cm
GPS	To monitor the current at sea surface

Table B30. SURPACT drifters.

Instrument	Brief description
CT sensors	Valeport CTD probe measuring seawater temperature and conductivity (salinity) at depth of 4 cm
Pressure sensor	Honeywell integrated pressure transducer (IPT) measuring atmospheric pressure
Audio analyzer	MSGEQ7 graphic equalizer rain sensor to infer rain intensity from sound spectra

Table B31. Pacific Gyre barometer–temperature drifters.

Instrument	Brief description
Thermistor	30 K thermistor measuring seawater temperature at a depth of 20 cm
Pressure sensor	Honeywell integrated pressure transducer (IPT) measuring atmospheric pressure at a height of 50 cm
GPS	monitors the current at sea surface

Table B32. OCARINA.

Instrument	Brief description
Anemometer	Gill R3-50 three-axis sonic anemometer measuring wind speed and horizontal and vertical velocities at 50 Hz at a height of 1.6 m
Weather sensors	Vaisala WXT-520 measuring air temperature, barometric pressure, and relative humidity at 1 Hz at a height of 1 m
Pyranometer	Campbell CNR4 Kipp and Zonen radiometer measuring broadband downward solar irradiance at a height of 1 m
Pyrgeometer	Campbell CNR4 Kipp and Zonen radiometer measuring upward and downward broadband infrared irradiance at a height of 1 m
Inertial platform	Xsens MTi-G IMU measuring time and accelerations at 50 Hz through gyroscopes, accelerometers, magnetometers, a GPS, and a barometer at a height of 0.1 m
CT sensor	Sea-Bird SBE-37 SI measuring sea surface temperature and conductivity/salinity at 1 Hz at a height of -0.2 m
Acoustic Doppler current profiler	Nortek Signature 1.2 GHz ADCP measuring vertical profiles of ocean current and horizontal and vertical velocities at 25 Hz from -0.3 to -17.3 m every 0.5 m of water

Table B33. PICCOLO.

Instrument	Brief description
Anemometers	Five homemade cup anemometers measuring the horizontal wind speed close to the surface (at 0.40, 0.60, 0.85, 1.15, and 1.6 m) to infer the friction velocity u_*, the wave peak period, and the roughness aerodynamic length z_0
Inertial platform	Xsens MTi-G IMU measuring time and accelerations at 50 Hz through gyroscopes, accelerometers, magnetometers, a GPS, and a barometer at a height of 0.1 m

Earth Syst. Sci. Data, 13, 4067–4119, 2021

https://doi.org/10.5194/essd-13-4067-2021

Author contributions. Author contributions are grouped (alphabetically) in different categories of contribution. BS and SB conceived of and led EUREC^{4}A and the preparation and writing of this paper. DF co-led the coordination as the local lead principal investigator (PI). FA, AB, CF, JK, PKQ, and SaS conceived of and led a major component of EUREC^{4}A. AB, DF, and SaS additionally contributed substantially to the preparation of the paper. The next grouping of authors, beginning with CA, made major contributions to the broader coordination and execution of scientific and/or dissemination activities. The final group of authors, beginning with NA, served as instrument PIs and/or made substantial contributions to the scientific preparation, execution, and/or dissemination activities. The groupings are subjective and imperfect but were motivated in part by the desire to better highlight the initiative of early career scientists in taking on responsibility and contributing to both the intellectual and organizational foundations of EUREC^{4}A. Specific contributions, as self statements, are recorded as part of the scientific documentation.

Competing interests. The authors declare that they have no conflict of interest.

Disclaimer. Publisher's note: Copernicus Publications remains neutral with regard to jurisdictional claims in published maps and institutional affiliations.

Special issue statement. This article is part of the special issue "Elucidating the role of clouds–circulation coupling in climate: datasets from the 2020 (EUREC^{4}A) field campaign". It is not associated with a conference.

References

Ackerman, A. S., vanZanten, M. C., Stevens, B., Savic-Jovcic, V., Bretherton, C. S., Chlond, A., Golaz, J.-C., Jiang, H., Khairoutdinov, M., Krueger, S. K., Lewellen, D. C., Lock, A., Moeng, C.-H., Nakamura, K., Petters, M. D., Snider, J. R., Weinbrecht, S., and Zulauf, M.: Large-Eddy Simulations of a Drizzling, Stratocumulus-Topped Marine Boundary Layer, Mon. Weather Rev., 137, 1083–1110, 2009.

Aemisegger, F., Vogel, R., Graf, P., Dahinden, F., Villiger, L., Jansen, F., Bony, S., Stevens, B., and Wernli, H.: How Rossby wave breaking modulates the water cycle in the North Atlantic trade wind region, Weather Clim. Dynam., 2, 281–309, https://doi.org/10.5194/wcd-2-281-2021, 2021.

Albrecht, B., Bretherton, C. S., Johnson, D., Schubert, W. S., and Frisch, A. S.: The Atlantic stratocumulus transition experiment – ASTEX, B. Am. Meteorol. Soc., 76, 889–904, 1995.

Albrecht, B., Ghate, V., Mohrmann, J., Wood, R., Zuidema, P., Bretherton, C., Schwartz, C., Eloranta, E., Glienke, S., Donaher, S., Sarkar, M., McGibbon, J., Nugent, A. D., Shaw, R. A., Fugal, J., Minnis, P., Paliknoda, R., Lussier, L., Jensen, J., Vivekanandan, J., Ellis, S., Tsai, P., Rilling, R., Haggerty, J., Campos, T., Stell, M., Reeves, M., Beaton, S., Allison, J., Stossmeister, G., Hall, S., and Schmidt, S.: Cloud System Evolution in the Trades (CSET): Following the Evolution of Boundary Layer Cloud Systems with the NSF–NCAR GV, B. Am. Meteorol. Soc., 100, 93–121, 2019.

Augstein, E., Schmidt, H., and Ostapoff, F.: The vertical structure of the atmospheric planetary boundary layer in undisturbed trade winds over the Atlantic Ocean, Bound.-Lay. Meteor., 6, 129–150, 1974.

Bailey, A., Toohey, D., and Noone, D.: Characterizing moisture exchange between the Hawaiian convective boundary layer and free troposphere using stable isotopes in water, J. Geophys. Res.-Atmos., 118, 8208–8221, 2013.

Bannon, J. K.: Large-scale vertical motion in the atmosphere, Nature, 163, 495–496, 1949.

Behrendt, A., Wulfmeyer, V., Senff, C., Muppa, S. K., Späth, F., Lange, D., Kalthoff, N., and Wieser, A.: Observation of sensible and latent heat flux profiles with lidar, Atmos. Meas. Tech., 13, 3221–3233, https://doi.org/10.5194/amt-13-3221-2020, 2020.

Bigorre, S. and Plueddemann, A. J.: The Annual Cycle of Air-Sea fluxes in the Northwest Tropical Atlantic, Front. Mar. Sci., 7, 612842, https://doi.org/10.3389/fmars.2020.612842, 2020.

Bodenschatz, E., Malinowski, S. P., Shaw, R. A., and Stratmann, F.: Can we understand clouds without turbulence?, Science, 327, 970–971, 2010.

Bony, S. and Stevens, B.: Measuring Area-Averaged Vertical Motions with Dropsondes, J. Atmos. Sci, 76, 767–783, 2019.

Bony, S., Stevens, B., Frierson, D. M. W., Jakob, C., Kageyama, M., Pincus, R., Shepherd, T. G., Sherwood, S. C., Siebesma, A. P., Sobel, A. H., Watanabe, M., and Webb, M. J.: Clouds, circulation and climate sensitivity, Nat. Geosci., 8, 261–268, 2015.

Bony, S., Stevens, B., Ament, F., Bigorre, S., Chazette, P., Crewell, S., Delanoë, J., Emanuel, K., Farrell, D., Flamant, C., Gross, S., Hirsch, L., Karstensen, J., Mayer, B., Nuijens, L., Ruppert, J. H., Sandu, I., Siebesma, P., Speich, S., Szczap, F., Totems, J., Vogel, R., Wendisch, M., and Wirth, M.: EUREC4A: A field campaign to Elucidate the Couplings between Clouds, Convection and Circulation, Surv. Geophys., 36, 1529–1568, 2017.

Bony, S., Schulz, H., Vial, J., and Stevens, B.: Sugar, Gravel, Fish and Flowers: Dependence of Mesoscale Patterns of Trade-wind Clouds on Environmental Conditions, Geophys. Res. Lett., 47, e2019GL085988, https://doi.org/10.1029/2019GL085988, 2020.

Bretherton, C. S., Krueger, S. K., Wyant, M. C., Bechtold, P., van Meijgaard, E., Stevens, B., and Teixeira, J.: A GCSS Boundary-Layer Cloud Model Intercomparison Study Of The First Astex Lagrangian Experiment, Bound.-Lay. Meteorol., 93, 341–380, 1999.

Brient, F., Schneider, T., Tan, Z., Bony, S., Qu, X., and Hall, A.: Shallowness of tropical low clouds as a predictor of climate models' response to warming, Clim. Dynam., 47, 433–449, 2016.

Broadwell, J. E. and Breidenthal, R. E.: A simple model of mixing and chemical reaction in a turbulent shear layer, J. Fluid Mech., 125, 397–410, 1982.

Brummer, B., Augstein, E., and Riehl, H.: On the low-level wind structure in the Atlantic trade, Q. J. Roy. Meteor. Soc., 100, 109–121, 1974.

Buckingham, C. E., Garabato, A. C. N., Thompson, A. F., Brannigan, L., Lazar, A., Marshall, D. P., Nurser, A. J. G., Damerell, G., Heywood, K. J., and Belcher, S. E.: Seasonality of submesoscale flows in the ocean surface boundary layer, Geophys. Res. Lett., 43, 2118–2126, 2016.

Callies, J. and Ferrari, R.: Interpreting Energy and Tracer Spectra of Upper-Ocean Turbulence in the Submesoscale Range (1–200 km), J. Phys. Oceanogr., 43, 2456–2474, 2013.

Carton, X.: Oceanic Vortices, in: Fronts, Waves and Vortices in Geophysical Flows, pp. 61–108, Springer Berlin Heidelberg, Berlin, Heidelberg, 2010.

Chazette, P., Totems, J., Baron, A., Flamant, C., and Bony, S.: Trade-wind clouds and aerosols characterized by airborne horizontal lidar measurements during the EUREC4A field campaign, Earth Syst. Sci. Data, 12, 2919–2936, https://doi.org/10.5194/essd-12-2919-2020, 2020.

Chelton, D. B. and Xie, S.-P.: Coupled Ocean-Atmosphere Interaction at Oceanic Mesoscales, Oceanography, 23, 52–69, 2010.

Chelton, D. B., Esbensen, S. K., Schlax, M. G., Thum, N., Freilich, M. H., Wentz, F. J., Gentemann, C. L., McPhaden, M. J., and Schopf, P. S.: Observations of Coupling between Surface Wind Stress and Sea Surface Temperature in the Eastern Tropical Pacific, J. Climate, 14, 1479–1498, https://doi.org/10.1175/1520-0442(2001)014<1479:OOCBSW>2.0.CO;2, 2001.

Cooper, W. A., Lasher-Trapp, S. G., and Blyth, A. M.: The influence of entrainment and mixing on the initial formation of rain in a warm cumulus cloud, J. Atmos. Sci., 70, 1727–1743, 2013.

D'Asaro, E. A., Shcherbina, A. Y., Klymak, J. M., Molemaker, J., Novelli, G., Guigand, C. M., Haza, A. C., Haus, B. K., Ryan, E. H., Jacobs, G. A., Huntley, H. S., Laxague, N. J. M., Chen, S., Judt, F., McWilliams, J. C., Barkan, R., Kirwan, A. D., Poje, A. C., and Özgökmen, T. M.: Ocean convergence and the dispersion of flotsam, P. Natl. Acad. Sci. USA, 115, 1162–1167, 2018.

de Boer, G., Borenstein, S., Calmer, R., Cox, C., Rhodes, M., Choate, C., Hamilton, J., Osborn, J., Lawrence, D., Argrow, B., and Intrieri, J.: Measurements from the University of Colorado RAAVEN Uncrewed Aircraft System during ATOMIC, Earth Syst. Sci. Data Discuss. [preprint], https://doi.org/10.5194/essd-2021-175, in review, 2021.

Delanoë, J., Protat, A., Vinson, J.-P., Brett, W., Caudoux, C., Bertrand, F., Parent du Chatelet, J., Hallali, R., Barthes, L., Haeffelin, M., and Dupont, J.-C.: BASTA: A 95-GHz FMCW Doppler Radar for Cloud and Fog Studies, J. Atmos. Ocean. Tech., 33, 1023–1038, 2016.

Denby, L.: Discovering the Importance of Mesoscale Cloud Organization Through Unsupervised Classification, Geophys. Res. Lett., 47, 1097–10, 2020.

Dixit, V. V., Nuijens, L., and Helfer, K. C.: Counter-gradient momentum transport through subtropical shallow convection in ICON-LEM simulations, Earth and Space Science Open Archive, p. 23, 2020.

Ewald, F., Kölling, T., Baumgartner, A., Zinner, T., and Mayer, B.: Design and characterization of specMACS, a multipurpose hy-

perspectral cloud and sky imager, Atmos. Meas. Tech., 9, 2015–2042, https://doi.org/10.5194/amt-9-2015-2016, 2016.

Fairall, C. W., Bradley, E. F., Godfrey, J. S., Wick, G. A., Edson, J. B., and Young, G. S.: Cool-skin and warm-layer effects on sea surface temperature, J. Geophys. Res.-Oceans, 101, 1295–1308, 1996.

Foussard, A., Lapeyre, G., and Plougonven, R.: Response of Surface Wind Divergence to Mesoscale SST Anomalies under Different Wind Conditions, J. Atmos. Sci., 76, 2065–2082, 2019.

Garstang, M. and Betts, A. K.: A Review of the Tropical Boundary Layer and Cumulus Convection: Structure, Parameterization, and Modeling, B. Am. Meteorol. Soc., 55, 1195–1205, 1974.

Gibson, E. R., Gierlus, K. M., Hudson, P. K., and Grassian, V. H.: Generation of Internally Mixed Insoluble and Soluble Aerosol Particles to Investigate the Impact of Atmospheric Aging and Heterogeneous Processing on the CCN Activity of Mineral Dust Aerosol, Aerosol Sci. Tech., 41, 914–924, 2007.

Holland, J. Z. and Rasmusson, E. M.: Measurements of the atmospheric mass, energy, and momentum budgets over a 500-kilometer square of tropical ocean, Mon. Weather Rev., 101, 44–55, 1973.

Illingworth, A. J., Barker, H. W., Beljaars, A., Ceccaldi, M., Chepfer, H., Clerbaux, N., Cole, J., Delanoë, J., Domenech, C., Donovan, D. P., Fukuda, S., Hirakata, M., Hogan, R. J., Huenerbein, A., Kollias, P., Kubota, T., Nakajima, T., Nakajima, T. Y., Nishizawa, T., Ohno, Y., Okamoto, H., Oki, R., Sato, K., Satoh, M., Shephard, M. W., Velázquez-Blázquez, A., Wandinger, U., Wehr, T., and van Zadelhoff, G. J.: The EarthCARE Satellite: The next step forward in global measurements of clouds, aerosols, precipitation, and radiation, B. Am. Meteorol. Soc., 96, 1311–1332, 2015.

Jensen, J. B. and Nugent, A. D.: Condensational growth of drops formed on giant sea-salt aerosol particles, J. Atmos. Sci., 74, 679–697, 2017.

Karstensen, J., Lavik, G., Kopp, A., Mehlmann, M., Boeck, T., Ribbe, J., Guettler, J., Nordsiek, F., Philippi, M., Bodenschatz, E., Tschitschko, B., Lange, D., Reus, K., Ritschel, M., Acquistapace, C., Wiskandt, J., Bendinger, A., Bagheri, G., Hall, K., Begler, C., Piosek, S., and Koerner, M.: EUREC⁴A Campaign, Cruise No. MSM89, 17 January–20 February 2020, Bridgetown Barbados – Bridgetown Barbados, The ocean mesoscale component in the EUREC4A++ field study, MARIA S. MERIAN-Berichte, https://doi.org/10.2312/cr_msm89, 2020.

Lambaerts, J., Lapeyre, G., Plougonven, R., and Klein, P.: Atmospheric response to sea surface temperature mesoscale structures, J. Geophys. Res.-Atmos., 118, 9611–9621, 2013.

Lange, D., Behrendt, A., and Wulfmeyer, V.: Compact Operational Tropospheric Water Vapor and Temperature Raman Lidar with Turbulence Resolution, Geophys. Res. Lett., 46, 14844–14853, 2019.

Lapeyre, G.: Surface Quasi-Geostrophy, Fluids, 2, 7–28, 2017.

Laxenaire, R., Speich, S., Blanke, B., Chaigneau, A., Pegliasco, C., and Stegner, A.: Anticyclonic Eddies Connecting the Western Boundaries of Indian and Atlantic Oceans, J. Geophys. Res.-Oceans, 123, 7651–7677, 2018.

Lena, M., Furtuna, I., and Fortuna, C.: EUREC4A film, Aeris, https://doi.org/10.25326/224, 2021.

Leon, D. C., French, J. R., Lasher-Trapp, S., Blyth, A. M., Abel, S. J., Ballard, S., Barrett, A., Bennett, L. J., Bower, K., Brooks, B., Brown, P., Charlton-Perez, C., Choularton, T., Clark, P., Collier, C., Crosier, J., Cui, Z., Dey, S., Dufton, D., Eagle, C., Flynn, M. J., Gallagher, M., Halliwell, C., Hanley, K., Hawkness-Smith, L., Huang, Y., Kelly, G., Kitchen, M., Korolev, A., Lean, H., Liu, Z., Marsham, J., Moser, D., Nicol, J., Norton, E. G., Plummer, D., Price, J., Ricketts, H., Roberts, N., Rosenberg, P. D., Simonin, D., Taylor, J. W., Warren, R., Williams, P. I., and Young, G.: The Convective Precipitation Experiment (COPE): Investigating the Origins of Heavy Precipitation in the Southwestern United Kingdom, B. Am. Meteorol. Soc., 97, 1003–1020, 2016.

Levin, Z., Ganor, E., and Gladstein, V.: The effects of desert particles coated with sulfate on rain formation in the eastern Mediterranean, J. Appl. Meteorol., 35, 1511–1523, 1996.

Li, X.-Y., Brandenburg, A., Svensson, G., Haugen, N. E. L., Mehlig, B., and Rogachevskii, I.: Effect of turbulence on collisional growth of cloud droplets, J. Atmos. Sci., 75, 3469–3487, 2018.

Mahadevan, A.: The Impact of Submesoscale Physics on Primary Productivity of Plankton, Annu. Rev. Marine. Sci., 8, 161–184, 2016.

Malkus, J. S.: On the structure of the trade wind moist layer, Massachusetts Institute of Technology and Woods Hole Oceanographic Institution, Cambridge, MA, 1958.

McWilliams, J. C.: Submesoscale currents in the ocean, Proc. R. Soc. A, 472, 27279778, https://doi.org/10.1098/rspa.2016.0117, 2016.

Mech, M., Orlandi, E., Crewell, S., Ament, F., Hirsch, L., Hagen, M., Peters, G., and Stevens, B.: HAMP – the microwave package on the High Altitude and LOng range research aircraft (HALO), Atmos. Meas. Tech., 7, 4539–4553, https://doi.org/10.5194/amt-7-4539-2014, 2014.

Mieslinger, T., Horváth, Á., Buehler, S. A., and Sakradzija, M.: The Dependence of Shallow Cumulus Macrophysical Properties on Large-Scale Meteorology as Observed in ASTER Imagery, J. Geophys. Res.-Atmos., 124, 11477–11505, 2019.

Naumann, A. K., Stevens, B., and Hohenegger, C.: A Moist Conceptual Model for the Boundary Layer Structure and Radiatively Driven Shallow Circulations in the Trades, J. Atmos. Sci, 76, 1289–1306, 2019.

Nencioli, F., Dong, C., Dickey, T., Washburn, L., and McWilliams, J. C.: A Vector Geometry–Based Eddy Detection Algorithm and Its Application to a High-Resolution Numerical Model Product and High-Frequency Radar Surface Velocities in the Southern California Bight, J. Atmos. Ocean. Tech., 27, 564–579, 2010.

Nuijens, L., Serikov, I., Hirsch, L., Lonitz, K., and Stevens, B.: The distribution and variability of low-level cloud in the North Atlantic trades, Q. J. Roy. Meteor. Soc., 140, 2364–2374, 2014.

O'Neill, L. W., Chelton, D. B., and Esbensen, S. K.: Covariability of Surface Wind and Stress Responses to Sea Surface Temperature Fronts, J. Climate, 25, 5916–5942, 2012.

Pöhlker, M. L., Ditas, F., Saturno, J., Klimach, T., Hrabě de Angelis, I., Araùjo, A. C., Brito, J., Carbone, S., Cheng, Y., Chi, X., Ditz, R., Gunthe, S. S., Holanda, B. A., Kandler, K., Kesselmeier, J., Könemann, T., Krüger, O. O., Lavrič, J. V., Martin, S. T., Mikhailov, E., Moran-Zuloaga, D., Rizzo, L. V., Rose, D., Su, H., Thalman, R., Walter, D., Wang, J., Wolff, S., Barbosa, H. M. J., Artaxo, P., Andreae, M. O., Pöschl, U., and Pöhlker, C.: Long-term observations of cloud condensation nuclei over the Amazon rain forest – Part 2: Variability and characteristics of biomass burning, long-range transport, and pristine

rain forest aerosols, Atmos. Chem. Phys., 18, 10289–10331, https://doi.org/10.5194/acp-18-10289-2018, 2018.

Prospero, J. M., Delany, A. C., Delany, A. C., and Carlson, T. N.: The Discovery of African Dust Transport to the Western Hemisphere and the Saharan Air Layer: A History, B. Am. Meteorol. Soc., 102, E1239–E1260, 2020.

Pujol, M.-I., Faugère, Y., Taburet, G., Dupuy, S., Pelloquin, C., Ablain, M., and Picot, N.: DUACS DT2014: the new multimission altimeter data set reprocessed over 20 years, Ocean Sci., 12, 1067–1090, https://doi.org/10.5194/os-12-1067-2016, 2016.

Ramanathan, V., Crutzen, P. J., Lelieveld, J., Mitra, A. P., Althausen, D., Anderson, J., Andreae, M. O., Cantrell, W., Cass, G. R., Chung, C. E., Clarke, A. D., Coakley, J. A., Collins, W. D., Conant, W. C., Dulac, F., Heintzenberg, J., Heymsfield, A. J., Holben, B., Howell, S., Hudson, J., Jayaraman, A., Kiehl, J. T., Krishnamurti, T. N., Lubin, D., McFarquhar, G., Novakov, T., Ogren, J. A., Podgorny, I. A., Prather, K., Priestley, K., Prospero, J. M., Quinn, P. K., Rajeev, K., Rasch, P., Rupert, S., Sadourny, R., Satheesh, S. K., Shaw, G. E., Sheridan, P., and Valero, F. P. J.: Indian Ocean Experiment: An integrated analysis of the climate forcing and effects of the great Indo-Asian haze, J. Geophys. Res.-Atmos., 106, 28371–28398, 2001.

Rasp, S., Schulz, H., Bony, S., and Stevens, B.: Combining crowdsourcing and deep learning to understand meso-scale organization of shallow convection, B. Am. Meteorol. Soc., 101, E1980–E1995, 2021.

Rauber, R. M., Stevens, B., Ochs III, H. T., and Knight, C.: Rain in shallow cumulus over the ocean–The RICO campaign, B. Am. Meteorol. Soc., 88, 1912–1928, 2007.

Renault, L., Molemaker, M. J., McWilliams, J. C., Shchepetkin, A. F., Lemarie, F., Chelton, D., Illig, S., and Hall, A.: Modulation of Wind Work by Oceanic Current Interaction with the Atmosphere, J. Phys. Oceanogr., 46, 1685–1704, 2016.

Renault, L., McWilliams, J. C., and Gula, J.: Dampening of Submesoscale Currents by Air-Sea Stress Coupling in the Californian Upwelling System, Sci. Rep., 8, 1–8, 2018.

Rieck, M., Nuijens, L., and Stevens, B.: Marine boundary layer cloud feedbacks in a constant relative humidity atmosphere, J. Atmos. Sci., 69, 2538–2550, 2012.

Riehl, H., Yeh, T. C., Malkus, J. S., and Laseur, N. E.: The North-East Trade of the Pacific Ocean, Q. J. Roy. Meteor. Soc., 77, 598–626, 1951.

Rocha, C. B., Chereskin, T. K., Gille, S. T., and Menemenlis, D.: Mesoscale to Submesoscale Wavenumber Spectra in Drake Passage, J. Phys. Oceanogr., 46, 601–620, 2016.

Rollo, C., Kinne, S., Kidane, A., Schlenczek, O., Schröder, M., Grosz, R., Sandiford, S., Raeke, A., Makuch, P., Gollop, J., Neuberger, A., de Groot, G., Meyer, M., Los, S., Chilinski, M., Ubele, A. A., Baranowski, D., Morfa-Avalos, Y., von Arx, J., Worbes, L., Nowak, J., Helfer, K., Kalesse, H., Ibáñez-Landeta, A., Siddle, E., Baier, K., Szkolka, W., Mohr, W., Schirmacher, I., and Röttenbacher, J.: EUREC4A Campaign, Cruise No. M161, 17 Jan 2020–3 Mar 2020, Bridgetown Barbados – Ponta Delgada Portugal, https://doi.org/10.2312/cr_m161, 2020.

Satoh, M., Stevens, B., Judt, F., Khairoutdinov, M., Lin, S.-J., Putman, W. M., and Düben, P.: Global Cloud-Resolving Models, Curr. Clim. Change Rep., 5, 172–184, 2019.

Schnitt, S., Orlandi, E., Mech, M., Ehrlich, A., and Crewell, S.: Characterization of Water Vapor and Clouds During the Next-Generation Aircraft Remote Sensing for Validation (NARVAL) South Studies, IEEE J. Sel. Top. Appl., 10, 3114–3124, https://doi.org/10.1109/JSTARS.2017.2687943, 2017.

Schroth, A. C., Chandra, M. S., and Meischner, P. F.: A C-Band Coherent Polarimetric Radar for Propagation and Cloud Physics Research, J. Atmos. Ocean. Tech., 5, 803–822, 1988.

Seifert, A. and Heus, T.: Large-eddy simulation of organized precipitating trade wind cumulus clouds, Atmos. Chem. Phys., 13, 5631–5645, https://doi.org/10.5194/acp-13-5631-2013, 2013.

Shcherbina, A. Y., D'Asaro, E. A., Lee, C. M., Klymak, J. M., Molemaker, M. J., and McWilliams, J. C.: Statistics of vertical vorticity, divergence, and strain in a developed submesoscale turbulence field, Geophys. Res. Lett., 40, 4706–4711, 2013.

Sherwood, S. C., Bony, S., and Dufresne, J.-L.: Spread in model climate sensitivity traced to atmospheric convective mixing, Nature, 505, 37–42, 2014.

Siebesma, A. P., Bretherton, C. S., Brown, A., Chlond, A., Cuxart, J., Duynkerke, P. G., Jiang, H., Khairoutdinov, M., Lewellen, D., Moeng, C.-H., Sánchez, E., Stevens, B., and Stevens, D. E.: A Large Eddy Simulation Intercomparison Study of Shallow Cumulus Convection., J. Atmos. Sci, 60, 1201–1219, 2003.

Siebesma, A. P., Bony, S., Jakob, C., and Stevens, B.: Clouds and Climate: Climate Science's Greatest Challenge, Cambridge University Press, Cambridge, UK, 2020.

Snodgrass, E. R., Di Girolamo, L., and Rauber, R. M.: Precipitation Characteristics of Trade Wind Clouds during RICO Derived from Radar, Satellite, and Aircraft Measurements, J. Appl. Meteorol., 48, 464–483, 2009.

Stephan, C. C., Schnitt, S., Schulz, H., Bellenger, H., de Szoeke, S. P., Acquistapace, C., Baier, K., Dauhut, T., Laxenaire, R., Morfa-Avalos, Y., Person, R., Quiñones Meléndez, E., Bagheri, G., Böck, T., Daley, A., Güttler, J., Helfer, K. C., Los, S. A., Neuberger, A., Röttenbacher, J., Raeke, A., Ringel, M., Ritschel, M., Sadoulet, P., Schirmacher, I., Stolla, M. K., Wright, E., Charpentier, B., Doerenbecher, A., Wilson, R., Jansen, F., Kinne, S., Reverdin, G., Speich, S., Bony, S., and Stevens, B.: Ship- and island-based atmospheric soundings from the 2020 EUREC[4]A field campaign, Earth Syst. Sci. Data, 13, 491–514, https://doi.org/10.5194/essd-13-491-2021, 2021.

Stevens, B.: EUREC4A Tracks, AERIS, https://doi.org/10.25326/165 [data set], 2021.

Stevens, B. and Schwartz, S. E.: Observing and Modeling Earth's Energy Flows, Surv. Geophys., 33, 779–816, 2012.

Stevens, B., Ackerman, A. S., and Albrecht, B. A.: Simulations of Trade Wind Cumuli under a Strong Inversion , J. Atmos. Sci., 58, 1870–1891, 2001.

Stevens, B., Lenschow, D. H., and Faloona, I.: On entrainment rates in nocturnal marine stratocumulus, Q. J. Roy. Meteorol. Soc., 129, 3469–3493, 2003.

Stevens, B., Moeng, C.-H., Ackerman, A. S., Bretherton, C. S., Chlond, A., de Roode, S., Edwards, J., Golaz, J.-C., Jiang, H., Khairoutdinov, M., Kirkpatrick, M. P., Lewellen, D. C., Lock, A., Müller, F., Stevens, D. E., Whelan, E., and Zhu, P.: Evaluation of Large-Eddy Simulations via Observations of Nocturnal Marine Stratocumulus, Mon. Weather Rev., 133, 1443–1462, 2005.

Stevens, B., Farrell, D., Hirsch, L., Jansen, F., Nuijens, L., Serikov, I., Brügmann, B., Forde, M., Linné, H., Lonitz, K., and Prospero, J. M.: The Barbados Cloud Observatory: anchoring inves-

tigations of clouds and circulation on the edge of the ITCZ, B. Am. Meteorol. Soc., 97, 787–801, 2016.

Stevens, B., Ament, F., Bony, S., Crewell, S., Ewald, F., Gross, S., Hansen, A., Hirsch, L., Jacob, M., Kölling, T., Konow, H., Mayer, B., Wendisch, M., Wirth, M., Wolf, K., Bakan, S., Bauer-Pfundstein, M., Brueck, M., Delanoë, J., Ehrlich, A., Farrell, D., Forde, M., Gödde, F., Grob, H., Hagen, M., Jäkel, E., Jansen, F., Klepp, C., Klingebiel, M., Mech, M., Peters, G., Rapp, M., Wing, A. A., and Zinner, T.: A High-Altitude Long-Range Aircraft Configured as a Cloud Observatory: The NARVAL Expeditions, B. Am. Meteorol. Soc., 100, 1061–1077, 2019a.

Stevens, B., Bony, S., Brogniez, H., Hentgen, L., Hohenegger, C., Kiemle, C., L'Ecuyer, T. S., Naumann, A. K., Schulz, H., Siebesma, P. A., Vial, J., Winker, D. M., and Zuidema, P.: Sugar, gravel, fish and flowers: Mesoscale cloud patterns in the trade winds, Q. J. Roy. Meteor. Soc., 146, 141–152, 2019b.

Stevens, B., Satoh, M., Auger, L., Biercamp, J., Bretherton, C. S., Chen, X., Düben, P., Judt, F., Khairoutdinov, M., Klocke, D., Kodama, C., Kornblueh, L., Lin, S.-J., Neumann, P., Putman, W. M., Röber, N., Shibuya, R., Vanniere, B., Vidale, P. L., Wedi, N., and Zhou, L.: DYAMOND: the DYnamics of the Atmospheric general circulation Modeled On Non-hydrostatic Domains, Prog. Earth Planet. Sci., 6, 1–17, 2019c.

Sullivan, P. P., McWilliams, J. C., Weil, J. C., Patton, E. G., and Fernando, H. J. S.: Marine boundary layers above heterogeneous SST: Across-front winds, J. Atmos. Sci., 77, 4251–4275, 2020.

Thomson, J.: Wave Breaking Dissipation Observed with SWIFT Drifters, J. Atmos. Ocean. Tech., 29, 1866–1882, https://doi.org/10.1175/JTECH-D-12-00018.1, 2012.

Thomson, J. and Girton, J.: Sustained Measurements of Southern Ocean Air-Sea Coupling from a Wave Glider Autonomous Surface Vehicle, Oceanography Magazine, 30, 104–109, https://doi.org/10.5670/oceanog.2017.228, 2017.

Thomson, J., Girton, J. B., Jha, R., and Trapani, A.: Measurements of Directional Wave Spectra and Wind Stress from a Wave Glider Autonomous Surface Vehicle, J. Atmos. Ocean. Tech., 35, 347–363, https://doi.org/10.1175/JTECH-D-17-0091.1, 2018.

Thomson, J., Moulton, M., de Klerk, A., Talbert, J., Guerra, M., Kastner, S., Smith, M., Schwendeman, M., Zippel, S., and Nylund, S.: A new version of the SWIFT platform for waves, currents, and turbulence in the ocean surface layer, in: IEEE/OES Workshop on Currents, Waves, and Turbulence Measurements, 2019.

Tomita, H., Miura, H., Iga, S., Nasuno, T., and Satoh, M.: A global cloud-resolving simulation: Preliminary results from an aqua planet experiment, Geophys. Res. Lett., 32, L08805, https://doi.org/10.1029/2005GL022459, 2005.

vanZanten, M. C., Stevens, B., Nuijens, L., Siebesma, A. P., Ackerman, A. S., Burnet, F., Cheng, A., Couvreux, F., Jiang, H., Khairoutdinov, M., Kogan, Y., Lewellen, D. C., Mechem, D., Nakamura, K., Noda, A., Shipway, B. J., Slawinska, J., Wang, S., and Wyszogrodzki, A.: Controls on precipitation and cloudiness in simulations of trade-wind cumulus as observed during RICO, J. Adv. Model. Earth Sy., 3, 1–20, 2011.

Vial, J., Bony, S., Dufresne, J.-L., and Roehrig, R.: Coupling between lower-tropospheric convective mixing and low-level clouds: Physical mechanisms and dependence on convection scheme, J. Adv. Model. Earth Sy., 8, 1892–1911, 2016.

Vial, J., Vogel, R., Bony, S., Stevens, B., Winker, D. M., Cai, X., Hohenegger, C., Naumann, A. K., and Brogniez, H.: A New Look at the Daily Cycle of Trade Wind Cumuli, J. Adv. Model. Earth Sy., 11, 3148–3166, 2019.

Vogel, R., Bony, S., and Stevens, B.: Estimating the Shallow Convective Mass Flux from the Subcloud-Layer Mass Budget, J. Atmos. Sci, 77, 1559–1574, 2020.

Weller, R. A.: Observing Surface Meteorology and Air-Sea Fluxes, Springer International Publishing, Cham, 17–35, https://doi.org/10.1007/978-3-319-66493-4_2, 2018.

Wendisch, M., Müller, D., Schell, D., and Heintzenberg, J.: An airborne spectral albedometer with active horizontal stabilization, J. Atmos. Ocean. Technol., 18, 1856–1866, 2001.

Wex, H., Dieckmann, K., Roberts, G. C., Conrath, T., Izaguirre, M. A., Hartmann, S., Herenz, P., Schäfer, M., Ditas, F., Schmeissner, T., Henning, S., Wehner, B., Siebert, H., and Stratmann, F.: Aerosol arriving on the Caribbean island of Barbados: physical properties and origin, Atmos. Chem. Phys., 16, 14107–14130, https://doi.org/10.5194/acp-16-14107-2016, 2016.

Wirth, M., Fix, A., Mahnke, P., Schwarzer, H., Schrandt, F., and Ehret, G.: The airborne multi-wavelength water vapor differential absorption lidar WALES: system design and performance, Appl. Phys. B, 96, 201–213, 2009.

Wulfmeyer, V., Turner, D. D., Baker, B., Banta, R., Behrendt, A., Bonin, T., Brewer, W. A., Buban, M., Choukulkar, A., Dumas, E., Hardesty, R. M., Heus, T., Ingwersen, J., Lange, D., Lee, T. R., Metzendorf, S., Muppa, S. K., Meyers, T., Newsom, R., Osman, M., Raasch, S., Santanello, J., Senff, C., Späth, F., Wagner, T., and Weckwerth, T.: A New Research Approach for Observing and Characterizing Land–Atmosphere Feedback, B. Am. Meteorol. Soc., 99, 1639–1667, 2018.

Wyszogrodzki, A. A., Grabowski, W. W., Wang, L.-P., and Ayala, O.: Turbulent collision-coalescence in maritime shallow convection, Atmos. Chem. Phys., 13, 8471–8487, https://doi.org/10.5194/acp-13-8471-2013, 2013.

Zhang, D., Cronin, M. F., Meinig, C., Farrar, J. T., Jenkins, R., Peacock, D., Keene, J., Sutton, A., and Yang, Q.: Comparing Air-Sea Flux Measurements from a New Unmanned Surface Vehicle and Proven Platforms During the SPURS-2 Field Campaign, Oceanography, 32, 122–133, 2019.

Zuidema, P., Li, Z., Hill, R. J., Bariteau, L., Rilling, B., Fairall, C., Brewer, W. A., Albrecht, B., and Hare, J.: On Trade Wind Cumulus Cold Pools, J. Atmos. Sci., 69, 258–280, 2012.